



Master's thesis

Comparison of Different Model Depths of a Direct Drive Wind Turbine Regarding the Generator Air Gap Sensitivity

This work was presented at the Chair for Wind Power Drives in Aachen on November 2019 and at the Politecnico di Torino in Turin on April 2020, by:

Paolo Andreani
Matriculation number: 250456

Faculty Internal Supervisor: Prof. Dr.-Ing. Ralf Schelenz

External Supervisor: Prof. Paolo Maggiore

External Supervisor: Dr. Matteo Davide Lorenzo Dalla Vedova

Supervising Scientific Assistant: Abdul Baseer, M.Eng.

Declaration of Authorship

I declare that this thesis and the work presented in it are my own and has been generated by me as the result of my own original research without use of any other than the cited sources and aids. Sentences or parts of sentences quoted literally are marked as such; other references with regard to the statement and scope are indicated by full details of the publications concerned. The thesis in the same or similar form has not been submitted to any examination body and has not been published. This thesis was not yet, even in part, used in another examination or as a course performance.

Aachen, 15.11.2019

Signature

Topic

Content

Nomenclature	IV
Abbreviations	VII
List of figures	VIII
List of tables	XI
1. Introduction	1
2. State of the Art and Background	3
2.1 Economic and Political Background	3
2.2 How Wind Turbines Generate Electricity	5
2.3 Differences between Direct Drive and Gear Box Generators	9
2.4 Main Cause of Air Gap Displacement	10
2.4.1 Wind load	10
2.4.2 Static and Dynamic eccentricity	12
2.4.3 Magnetic Force	13
2.4.4 Increase of temperature	14
2.4.5 Centrifugal force	15
2.4.6 Gravity	16
2.4.7 Manufacturing/ Installation defect.....	17
3. Mathematical theory	18
3.1 Finite elements method	18
3.1.1 Type of elements	20
3.2 Multi Body simulation	22
3.2.2 Model elements	22
3.2.3 Lagrange equation 1 st kind	24
3.2.4 Eigen behaviour.....	26
3.2.5 SIMPACK flexible body	27
3.3 Modal assurance criterion	27
4. Structure of the models for the simulations	29
4.1 Geometrical and mechanical characteristics	29
4.2 Bearings	31
4.3 Convergence analysis	34
4.4 MAC matrix	42
4.5 Tower	47
4.6 Blades	47
4.7 Entire model	48

4.7.1	Finite element model	48
4.7.2	Multi body model assembled.....	54
5.	Simulation results	57
5.1	Air gap displacement	57
5.1.1	Static finite element simulation.....	60
5.1.2	Comparison results FEM to MB	71
5.2	Campbell diagram.....	75
5.3	Optimization	77
6.	Outlook and further studies	80
7.	Summary	81
	Appendix	84

Nomenclature

Symbol	Unit	Description
E_k	J	Kinetic energy
m	kg	Mass
\bar{u}	m/s	Average speed
P_W	W	Wind power
\dot{m}	kg/s	Mass flow
A	m^2	Section area
ρ	kg/m^3	Density
r	m	Wind turbine radius
π		Pi
ρ_0	kg/m^3	Density of the air in state 0
c	J/K	Heat capacity
z	m	Altitude
T_0	K	Temperature of the air in state 0
g	m/s^2	Gravitational acceleration
R	$m^3 atm / mol K$	Gas constant
C_P		Power coefficient
$P_{me,out}$	W	Actual electrical power produced
a		Axial induction factor
η_t		Total efficiency factor
η_{gear}		Losses due to gearbox
η_{gen}		Losses due to generator
η_{ele}		Losses due to electric system
TSR or λ		Tip Speed Ratio
v_m	m/s	Wind shear variation
α		Empirical wind shear exponent
h	m	Height of tower
ψ	rad	Blade azimuthal angle
v_t	m/s	Tower shadow disturbance
x	m	Distance from blade to tower
σ_F	N/m^2	Stress due to the magnetic field
σ_{Fn}	N/m^2	Normal component of σ_F

Symbol	Unit	Description
σ_{Ftan}	N/m^2	Tangential component of σ_F
μ_0	N/A^{-2}	Permeability of free space
H	m/A	Magnetic field strength
H_n	m/A	Normal component of H
H_{tan}	m/A	Tangential component of H
F_{UMP}	N	Unbalance magnetic pull
D	m	Air gap diameter
L	m	Air gap length
B_m	$kg\ s^{-2}A^{-1}$	Magnetic field
ϑ	rad	Angular position on the air gap
e	m	Form rotor centre to stator centre
g	m	Air gap size
Φ_{conv}	W/m^2	Heat flux
k	$W/(m^2K)$	Heat transfer coefficient
ΔT	K	Difference in temperature
ΔL	m	Air gap displacement
L_0	m	Initial air gap size
F_c	N	Centrifugal force
a_c	m/s^2	Centrifugal acceleration
ω	rad/s^2	Rotor angular velocity
\vec{F}_g	N	Gravity force
$F_{g,x}$	N	x component of \vec{F}_g
$F_{g,y}$	N	y component of \vec{F}_g
Φ	J	potential elastic energy
U	J	Potential energy
dV	m^3	Infinitesimal volume of integration
dS	m^2	Infinitesimal surface of integration
$\{\bar{\sigma}\}$	N/m^2	Stress strain vector
$\{\bar{\varepsilon}\}$		Strain components vector
$\{\bar{u}\}$	m	Displacement in the space
$\{\dot{\bar{u}}\}$	m/s	Velocity vector
$\{\hat{X}_v\}$	N/m^3	Volumetric constant elastic

Symbol	Unit	Description
$\{\widehat{X}_s\}$	N/m^2	Surface constant elastic
$[K^{(e)}]$		Stiffness matrix
$[M^{(e)}]$ or \vec{M}		Mass matrix
$\{F^{(e)}\}$		Force vector
$\{\bar{q}^{(e)}\}$		Generalized coordinates vector
$[C^{(e)}]$		Elastic stiffness coefficient matrix
$[B^{(e)}]$		Linear part of the strain array
$[N^{(e)}]$		Interpolation matrix
$\{A_q\}$		Mode shape vector
$\vec{g}(\vec{r}, \vec{r}, t)$		Geometrical kinematic constraints
\vec{r}_i	m	Position vector
\vec{L}_i	$kg\ m^2/s$	Vector of angular momentum
\vec{m}_i	$kg\ m^2/s$	Rate of change angular momentum
\vec{I}_i		Inertial tensor
$\vec{\omega}_i$	rad/s^2	Vector of the angular acceleration
\vec{E}		Identity matrix
$\vec{G}_{(\vec{r},t)}$		Jacobian matrix of the constraint
$\vec{Y}_{(\vec{r},t)}$		Constraint vector partial derivate of t
λ		Lagrange multiplier
\vec{P}		Velocity dependent forces matrix
\vec{Q}		Position dependent forces matrix
\vec{x}		Position vector
$p(\lambda)$		Characteristic polynomial
$MAC(i, k)$		MAC matrix's cell i, j value

Abbreviations

Abbreviation	Description
UNFCCC	United Nations Framework Convention on Climate Change
LCOE	Levelized cost of electricity
USD	United State Dollars
FEM	Finite Elements Method
MBS	Multi Bodies Simulation
DD	Direct Drive
GB	Gearbox
MAC	Modal Assurance Criterion
<i>dof</i>	Degree of freedom
ALLSD	Static dissipation energy
ALLSE	Strain energy
IRM	Inertial Relief Modes
C3D10	Tetrahedron quadratic element with 10 nodes
C3D20R	Quadratic brick with 20 nodes, reduced integration

List of figures

Figure 2.1: Global new investment in clean energy by sector [10].....	3
Figure 2.2: Figure 2.2 LCEO - Historic development [10]	4
Figure 2.3: Pressure and speed variation in an ideal model of wind turbine [13, 14]	7
Figure 2.4: Power coefficient as a function of axial induction factor [13]	8
Figure 2.5: Power coefficient as a function of TSR [15]	9
Figure: 2.6 Cost of 3 MW DFIG 3G and PMSG DD [36]	9
Figure 2.7: Gearbox and Direct Drive wind turbines [37, 38]	10
Figure 2.8: CFD model of wind turbine rotor	11
Figure 2.9: Wind speed and torque on the tower as function of the blade azimuthal angle under the effect of tower shadow and wind shear [21].....	12
Figure 2.10: Static and dynamic eccentricity	12
Figure 2.11: Generic section with normal stress, across the airgap [24]	13
Figure 2.12: UMP in: symmetrical machine (a); with rotor displaced vertically downwards [25].....	14
Figure 2.13: Expansion due to temperature rises in the stator (ΔT_s) and rotor (ΔT_r) in a radial flux machine	14
Figure 2.14: Stator temperature distribution in an outer rotor direct drive 2,5 kW [23]	15
Figure 2.15: Effect of centripetal force in a radial-flux machine [24]	15
Figure 2.16: Centrifugal force on the rotor surface and rotor deflection	16
Figure 2.17: The major and the minor component of gravity [24]	17
Figure 2.18: Failure Causes & Failure consequences [41]	17
Figure 3.1: Steps to create a FEM system: CAD, partition CAD, meshing	18
Figure 3.2: Shear locking: 1st order element $\gamma_{xy}=0$ $\sigma_{xy}=0$; 2nd order element $\gamma_{xy}\neq 0$ $\sigma_{xy}\neq 0$	21
Figure 3.3: Convergence analysis for the finite elements mesh [26]	22
Figure 3.4: Example of Multi Body System [28]	23
Figure 3.5: Bad example of MAC matrix (left), good example of MAC matrix (right) [32]	28
Figure 4.1: Wind turbine: model in SIMPACK	29
Figure 4.2: Cross section of Generator	30
Figure 4.3: Radial stiffness of Fixed and Loosed bearings	32
Figure 4.4: Axial stiffness of Fixed bearing.....	32
Figure 4.5 Fixed bearing different configurations	32
Figure 4.6: Loosed bearing different configurations	33
Figure 4.7: Fixed bearing F.E.M modelling in ABAQUS: first concept with artificial damping	33
Figure 4.8: Sketch of rigid bearing.....	34
Figure 4.9: Machine frame: CAD model a) and FEM model b)	34
Figure 4.10: Machine frame: hexagonal and tetragonal mesh	35
Figure 4.11: Frame: static convergence analysis	35
Figure 4.12: Frame: modal convergence analysis	36
Figure 4.13 Shaft: static convergence analysis	36
Figure 4.14: Shaft: modal convergence analysis	37
Figure 4.15: Connector: static convergence analysis.....	37
Figure: 4.16 Connector: modal convergence analysis	38
Figure 4.17: Rotor: static convergence analysis	38
Figure 4.18: Rotor: modal convergence analysis	39
Figure 4.19: Stator: static convergence analysis.....	39
Figure 4.20: Stator: modal convergence analysis	40
Figure 4.21: Hub: static convergence analysis.....	40
Figure 4.22: Hub: modal convergence analysis	41
Figure 4.23: MAC matrix iterations	42
Figure 4.24: Hub: MAC matrix	43
Figure 4.25: Shaft: MAC matrix	43
Figure 4.26: Frame: MAC matrix	44

Figure 4.27: Stator: MAC matrix	44
Figure 4.28: Connector: MAC matrix	45
Figure 4.29: Rotor: MAC matrix	45
Figure 4.30: Auto MAC matrix FEM.....	46
Figure 4.31: Auto MAC matrix MBS	46
Figure 4.32: MAC matrix FEM - MBS	46
Figure 4.33: Tower SIMPACK model	47
Figure 4.34: Blades SIMPACK model	47
Figure 4.35: Generator F.E.M.....	48
Figure 4.36: ABAQUS: constraint to apply the weight of the blades	49
Figure 4.37: Magnetic pull for different model deep	49
Figure 4.38: ABAQUS: Connector- constraint-wire to apply the magnetic pull with one slice.....	50
Figure 4.39: ABAQUS: tie constraint between frame and shaft.....	50
Figure 4.40: Sketch of: Node to Surface & Surface to Surface	51
Figure 4.41: COPEN output static simulation of two plate. a) Surface to surface & b) Node to surface.....	51
Figure 4.42: Missing Master surface problem [27]	52
Figure 4.43: ABAQUS: air gap modelling.....	52
Figure 4.44: Comparison between COPEN and minimal distance	53
Figure 4.45: Magnitude displacement of whole system & Air gap clearance – Simulation WITHOUT LOADS.....	53
Figure 4.46: Rotor MBS part.....	54
Figure 4.47: Stator MBS part.....	54
Figure 4.48: Force element type and 2D Generator model.....	55
Figure 4.49: SIMPACK sensor to study the air gap displacement	55
Figure 4.50: 2D model of the wind turbine.....	56
Figure 5.1: a) Side view of generator & b) Front view of rotor.....	57
Figure 5.2: Air gap 2D plot example	58
Figure 5.3: Air gap average displacement calculation.....	58
Figure 5.4: Air gap displacement distribution	59
Figure 5.5: ABAQUS COPEN: slave surface rotor & slave surface stator.....	59
Figure 5.6 Air gap displacement distribution	59
Figure 5.7: ABAQUS: stabilization of the system by the specific damping factor	60
Figure 5.8: ABAQUS plot of ALLSD and ALLSE.....	60
Figure 5.9: Air gap displacement: no loads applied	61
Figure 5.10: Air gap displacement: Gravity	61
Figure 5.11: Air gap displacement: Gravity Blades weight	62
Figure 5.12: Air gap displacement: Gravity Blades weight Magnetic pull 1 slice	62
Figure 5.13: Air gap displacement: Gravity Blades weight Magnetic pull 3 slices	63
Figure 5.14: Air gap displacement: Gravity Blades weight Magnetic pull 5 slice	63
Figure 5.15: Air gap displacement: Gravity Blades weight Magnetic pull 10 slices	64
Figure 5.16: Air gap displacement: Gravity Blades weight Magnetic pull 20 slices	64
Figure 5.17: Airgap displacement: Comparison between the impact of the number of the slices	65
Figure 5.18: Maximum and Average displacement for magnetic pull split up in different number of slices.....	65
Figure 5.19: Boundary conditions for the simulation with torque around x	66
Figure 5.20: Air gap displacement: Gravity Blades weight Generator torque	66
Figure 5.21: Air gap displacement: Gravity Blades weight Magnetic pull Generator torque Wind.....	67
Figure 5.22: Second bearings configurations: Gravity Magnetic pull Generator torque Wind	67
Figure 5.23: Third bearings configurations: Gravity Magnetic pull Generator torque Wind	68
Figure 5.24: Airgap displacement: Comparison between impact of different load set	68
Figure 5.25: Rigid bearings air gap displacement: Gravity Blades weight Magnetic pull Generator torque Wind ...	69
Figure 5.26: Average displacement: real bearing VS rigid bearing	69
Figure 5.27: Average displacement: real bearing VS rigid bearing	70
Figure 5.28: MBS air gap displacement sketch of the top generator's top part	71

Figure 5.29: 20 eigen mode active	72
Figure 5.30: 40 eigen mode active	72
Figure 5.31: 50 eigen mode active	73
Figure 5.32: 80 eigen mode active	73
Figure 5.33: 80 eigen mode active	74
Figure 5.34: Convergence analysis for the cut IRM frequency and for the number of eigen mode	74
Figure 5.35: Air gap displacement from MBS simulation	75
Figure 5.36: Campbell diagram for the eigenfrequency until 39	76
Figure 5.37Campbel diagram for natural frequency lower to 3 Hz	76
Figure 5.38: Lateral section of the optimization model	77
Figure 5.39: Optimization model analysis without loads	78
Figure 5.40: Optimization model air gap displacement: Gravity weight Generator torque Magnetic pull Wind	78
Figure 5.41: Average displacement comparison	79
Figure 5.42 Maximum displacement comparison	79
Figure 6.1: Different bearing position	80

List of tables

Table 2.1: Capacity (MW) in relation to estimated jobs and economic impact, 2017 [7]	5
Table 3.1: F.E.M. elements in ABAQUS	21
Table 4.1: Steel mechanical properties	30
Table 4.2: Geometrical characteristic of Fixed bearing [33]	31
Table 4.3: Geometrical characteristic of Loosed bearing [34]	31
Table 4.4: Frame: properties of the mesh	36
Table 4.5: Shaft: properties of the mesh	37
Table 4.6: Connector: properties of the mesh	38
Table 4.7: Stator: properties of the mesh	39
Table 4.8: Rotor: properties of the mesh	40
Table 4.9: Hub: properties of the mesh	41
Table 4.10: Summary of the properties of the mesh	41
Table 4.11: Forces and Moment.....	48
Table 5.1: Maximum and minimum displacement: slave surface rotor & slave surface stator	59
Table 5.2: Description of eigenmode	77

1. Introduction

Since the industrial revolution the need for energy has always increased and as a consequence Green House Gas (GHG) have reached dangerous levels for the World ecosystem. From 1971 to 2017 CO_2 emission has grown from 14 Gt/year to 32 Gt/year [1] [2]. The almost totality of researchers say that Anthropocene is the cause for the increased temperature (around $1^\circ C$ $2^\circ C$ between 1850 and 2019) [3] [4].

Since 1992, when United Nations Framework Convention on Climate Change (UNFCCC) was founded in Rio de Janeiro, more and more people in the World have understood that climate change is a real problem and they have begun to find ways to reduce GHG emissions. After this summit, other summits have followed, the most important were held in Kyoto 1997 and in Paris in 2015. During the Paris summit world countries agreed to keep the global temperature rise well below $2^\circ C$ above pre-industrial levels and to pursue efforts to limit the temperature increase to $1,5^\circ C$ [5] [6].

More and more countries, especially in Europe, started to invest money in order to find better ways to produce green energy in order to replace fossil energy sources. Wind turbines have an important role in the decarbonization context because they are the most suitable green energy resource and their environmental impact and operational life have a small effect on the ecosystem. However, the state of art of the wind turbine is not enough to satisfy the global demand of energy. The wind energy market value now (2019) is around 45.000 million dollars for the capacity value of 440,475 MW [7]. The cheaper technology is still the gearbox configuration, its cost is around 300 thousand euro per Megawatt [8] against the 450 thousand euro per Megawatt of the direct drive (DD) generator. Nevertheless, during the last period the cost of the energy from these two configurations is always getting closer to each other. For high reliability the direct drive concept is better than the gearbox concept and is more and more used for offshore wind turbine. The actual gap in cost between the offshore wind energy and the onshore wind energy is around 100 dollars/MWh whereas in 2012 when the gap was around 200 dollars/MWh [8].

The main difference between the gearbox configuration and the direct drive configuration is that in the first case the generator is fair to the main stress load, as the wind load and the bladed weight and the main problem in this configuration is the gearbox's vibrations, while in the second case there aren't vibrations from the gear box but the generator is directly in touch with the external loads. The main problem in the direct drive configuration is that the optimal distance between stator and rotor is 1/1000 times of the air gap diameter (for instance if the air gap diameter is 5 m the clearance between stator and rotor should be 5 mm). Every change out of this clearance will cause a decrease in the efficiency of all machine. If the stator and rotor get in touch the generator will rapidly get damaged. Due to that, the DD generator must have a very stiff structure and bearing arrangement in order to stabilise the air gap. Therefore, the bearings in DD concept have a fundamental role.

The aim of this thesis is to analyse how the air gap changes in a 3.6 MW inner rotor wind turbine.

Chapter 2 describes how wind turbines work and what their physical limits are. It goes on to describe the wind turbine market as a good investment and the two most important technologies for wind turbines with horizontal axis as well as their advantages and disadvantages. The chapter closes with an introduction to the topics of this thesis, the main loads that affect a direct drive wind turbine during its operation and their negative effect on the efficiency of the system as well as the safety. The three kinds of loads that will be analysed are the aerodynamic wind load, the magnetic pull and the gravity.

Chapter 3 explains the mathematical theory used to conduct these tests. First of all, it explains the finite elements method (FEM) which is used to analyse the generator in ABAQUS and a static analysis of it, then it describes the different properties of each finite element and an ABAQUS implementation of it. Then it focuses on the multibody simulation (MBS) and SIMPACK software. At the end the modal assurance criterion (MAC) and how ABAQUS and SIMPACK models have been compared in order to make sure that the static and dynamic

analysis are substantial is showed

Chapter 4 presents the model construction beginning with a global overview of the geometrical and mechanical characteristics of the wind turbine under exam. Then a mesh convergence study is introduced together with an explanation on which kind of mesh have been chosen for each component. Finally, the Auto MAC matrix is introduced so that each FEM model is consistent with itself and the MAC matrix to make sure that each MBS model is consistent with its own FEM model. At the end the whole FEM and MBS model are showed.

Chapter 5 shows the results of the analysis: first of all, the results of the static analysis for three different load configurations (the first one considers the gravity, the second one adds the wind load and the last one adds the magnetic pull between generator-stator and generator-rotor). Then the results of the MBS simulations are shown. At the end of the chapter the results of MBS are commented and compared.

The last section is dedicated to the comparison between the different outputs of each analysis and to extra results like the Bode diagram.

2. State of the Art and Background

This chapter explains first of all why wind turbine technology had a rapid market growth in the last few years, why the economic market has invested more and more in this sector and why countries have decided to push forward these investments. Then it explains the physical process by which the wind turbine generates power, different kinds of wind turbines, advantages and disadvantages of direct drive generators and different kinds of concepts. The end of the chapter focuses on the causes of air gap displacement in a direct drive generator and describes the main factors, which have an impact on the generator air gap deflection.

2.1 Economic and Political Background

Since 1992, when UNFCCC was founded, the global warming problem has attracted the interest of researchers from all over the world. The Kyoto protocol [5] in 1998 represents the first step countries have made to follow researchers' suggestions to reduce human impact on the ecosystem. Other political meetings followed but the most important is the Paris Agreement in 2015. Its main points are a long-term goal of keeping the increase in global average temperature to well below 2 °C above pre-industrial levels and to limit the increase to 1.5 °C (article 2.1.(a)) and of peaking global emissions as soon as possible (article 4) [6]. Companies are encouraged to invest in clean energy resources, for instance General Electric (GE) in 2018 made the most powerful offshore direct drive wind turbine in the world, Haliade-X 12MW. It is 200 m high, each blade is longer than 100 m and its rotor has a 220 m diameter, GE estimates that Haliade-X 12MW can produce energy for 16000 houses. GE is also going to invest 400 million USD to empower development and deployment of its turbine during the next 3-5 years [9].

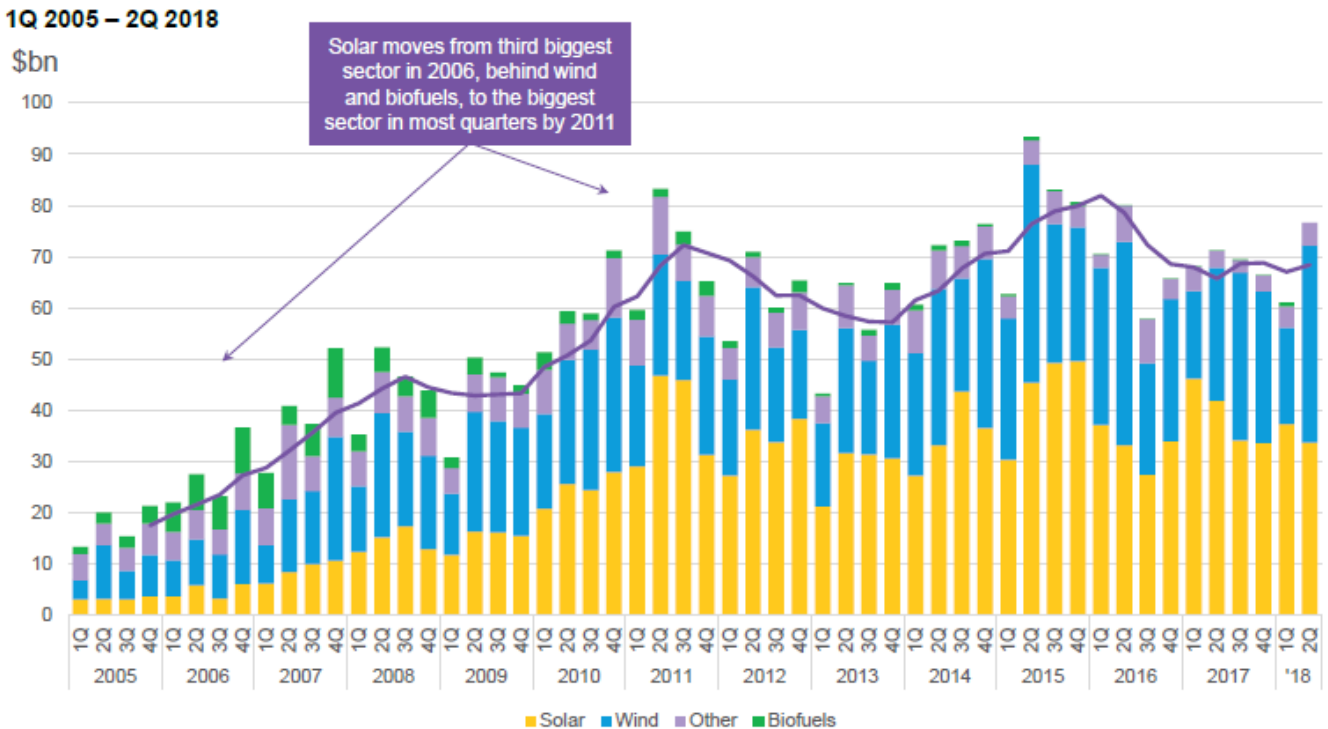


Figure 2.1: Global new investment in clean energy by sector [10]

Figure 2.1: Global new investment in clean energy by sector shows the investment for each quarter from 2005 until the second quarter of 2018. It is evident that the wind energy market is growing, the trend in the clean energy sector is positive, solar energy seems to have a very bright future. Nevertheless, each market operates to satisfy its own demand that's why the stream of money is very different for each market. In North, Central and South America investments in clean energy are worth around 20 billion USD and more than a half are

dedicated to wind energy. In Europe companies invest less than in America, the European market is worth around 15 billion USD. Wind is the favourite energy source in Europe. The best market for clean energy is the Asia Pacific, during the second quarter of 2018 more than 40 billion USD have been spent to improve its renewable source of energy. In Asia Pacific the most used form of energy is the solar one, but the wind energy market is worth around 20 billion USD, like the American market and more than the European one [10].

The rapid growth of the wind turbine sector is also witnessed by the fact that wind energy has become less expensive during the last years. Since 2015 the global capacity of wind turbine farms has grown to around 50 GW thus reducing the cost of wind energy [8]. Global installations at present have reached 592 GW (169 GW from Europe [8]) 23 of which are produced offshore. The following graph represents the historical development of levelized cost of energy LCOE. It is evident that the onshore solution produces less expensive energy than the offshore solution.

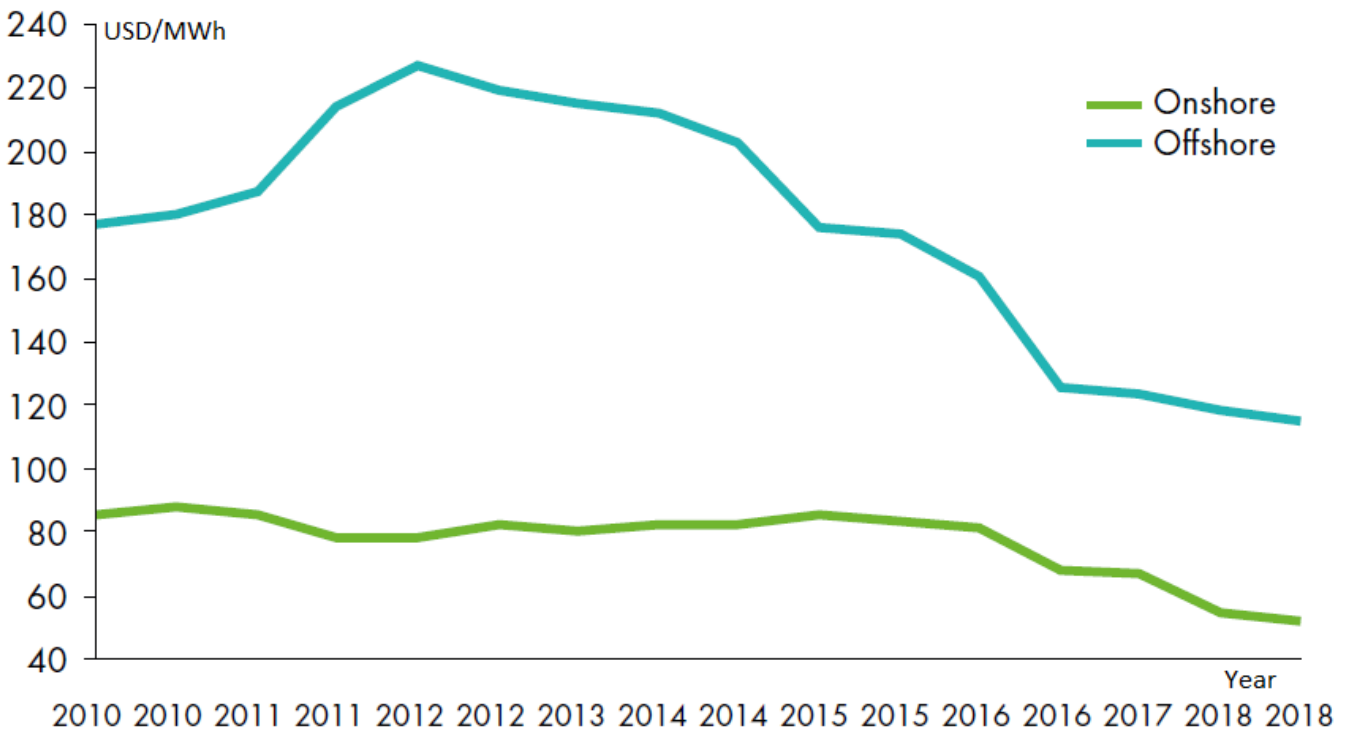


Figure 2.2: Figure 2.2 LCEO - Historic development [10]

This difference in cost is due to the different environment in which the turbines must work. The offshore solution operates in the sea, so this kind of turbine needs more manufacturing, its production process is more complex and as a consequence more expensive. Nevertheless, offshore wind turbines are a very good solution because they don't take up space on the ground and they operate in very windy environments, so they should produce more energy than their onshore counterparts. For this reason, technology needs to be improved in order to reduce their construction and maintenance costs as well as their efficiency and related energy losses. As it is possible to see in Figure 2.2 all efforts made until now produced a rapid decrease in the LCEO and the trend seems to be good. This could be possible thanks to the direct drive system whose production is very expensive but whose operational life is cheap, especially when it comes to the offshore solution. Every report made by official research centres has established that the wind market has also an important societal impact. During 2016 more than one million employees in the world have worked in the wind turbine field and the employment trend is increasing [11]. China expects that the number of jobs will increase up to 300,000 by 2020, for a total of 800,000 workers [7]. In America the wind turbine field is the second fastest-growing job with more than 100,000 workers [7]. In Europe the wind industry provides jobs for 260,000 people, 160,000 of them only in Germany [7]. The economic impact on society in 2017 has been more than 45 billion USD [7]. The following table shows the capacity of each country as regards estimated job and economic impact in 2017.

Country	Capacity (MW)	Estimated numbers of jobs	Economic impact (million dollars)
China	188'390	507'000	---
United States	88'973	105'500	11'000
Germany	55'876	160'200	15'245
Spain	23'092	22'468	2'710
United Kingdom	19'836	2'000	---
France	13'488	19'000	---
Canada	12'239	---	1'116
Italy	9'496	26'000	3'927
Sweden	6'691	---	---
Portugal	5'513	3'250	1'348
Denmark	5'503	>30'000	---
Mexico	3'942	1'300	---
Ireland	3'368	3'400	---
Austria	2'828	1'490	408
Korea	1'165	2'424	943
Switzerland	75	---	39
Total	440'475	>870'000	>45'000

Table 2.1: Capacity (MW) in relation to estimated jobs and economic impact, 2017 [7]

The data reported in Table 2.1 confirm the first place of Germany in the European wind sector. They also highlight the importance of this market for all other European countries. Spain, France Italy and Denmark have more than 20,000 workers and still have a lot of growth potential.

2.2 How Wind Turbines Generate Electricity

Man has always used the kinetic energy derived from wind to simplify his lifestyle. Ancient communities began to use wind energy to pump water, sail ships, grind grain or move presses. Modern wind turbines convert the wind's kinetic energy into electrical energy by means of a power converting machine [12, 13].

First of all, the wind turbine converts the wind's kinetic energy into mechanical energy. The kinetic energy (E_k) is defined as:

$$E_k = \frac{1}{2} m \bar{u}^2 \tag{Equation 2.1}$$

m is the mass of the air flow [kg]

\bar{u} is the wind average speed [m/s]

Using a derivative equation respect to time wind power (P_w) can be obtained as

$$P_w = \frac{dE_k}{dt} = \frac{1}{2} \dot{m} \bar{u}^2 \tag{Equation 2.2}$$

\dot{m} is the mass flow rate [kg/s]

The global mass involved in this process is equal to

$$\dot{m} = A \bar{u} \rho \tag{Equation 2.3}$$

A is the section area through which the mass flow rate passes [m^2]

ρ is the density of the air [kg/m^3]

\bar{u} is the wind average speed [m/s^2]

Hence, the ideal power (P_w) that could be produced by a generator is equal to

$$P_w = \frac{1}{2} A \rho \bar{u}^3 \quad \text{Equation 2.4}$$

Where A , the blades' swept area, can be calculated from the formula

$$A = \pi [(l+r)^2 - r^2] = \pi l (1+2r) \quad \text{Equation 2.5}$$

r is the radius of the wind turbine rotor [m]

And, according to the equation of state and the hydrostatic equation, the density (ρ) of the air can be written as

$$\rho = \rho_0 \left(1 + \frac{c z}{T_0}\right)^{-\frac{g}{cR} + 1} \quad \text{Equation 2.6}$$

ρ_0 is the density of the air in state 0 [kg/m^3]

c is the heat capacity [J/K]

z is the altitude of the body [m]

T_0 is the temperature of the air in state 0 [K]

g is the gravitational acceleration and it is equal to $9.81 [m/s^2]$

R is the gas constant and it is equal to $8.2057 [m^3 atm / mol K]$

Looking at the Equation 2.4 and Equation 2.5, it is clear that in order to obtain higher power we need to have higher wind speed, longer blades and higher air density.

However, due to the various aerodynamic losses in the system (blade-tip, blade root, profile, turbulence, ...) it isn't possible to extract all the wind power during this first stage. It is therefore necessary to introduce the power coefficient (C_p) which is defined as the ratio of the actual drawing power divided by the wind power into the turbine [13], as

$$C_p = \frac{P_{me,out}}{P_w} = \frac{P_{me,out}}{0,5 \rho A \bar{u}^3} \quad \text{Equation 2.7}$$

$P_{me,out}$ is the actual electrical power produced [W]

P_w is the wind power into turbine [W]

First Lanchester in 1915 and then Betz in 1920 [13] have proved that it is impossible for one ideal wind turbine (a turbine with no hub and no resistance on the blades) to convert more than 59,26% of wind's kinetic energy into mechanical energy. This limited efficiency is due to the braking effect of the wind from its upstream speed V_1 to its downstream speed V_2 , while allowing a continuation of the flow regime [14].

By referring to Figure 2.3, considering the case without change in the air speed right across the wind blades with the pressure far upstream and downstream from the wind equal to the static pressure of the undisturbed flow, it is possible to calculate the Lanchester-Betz limit.

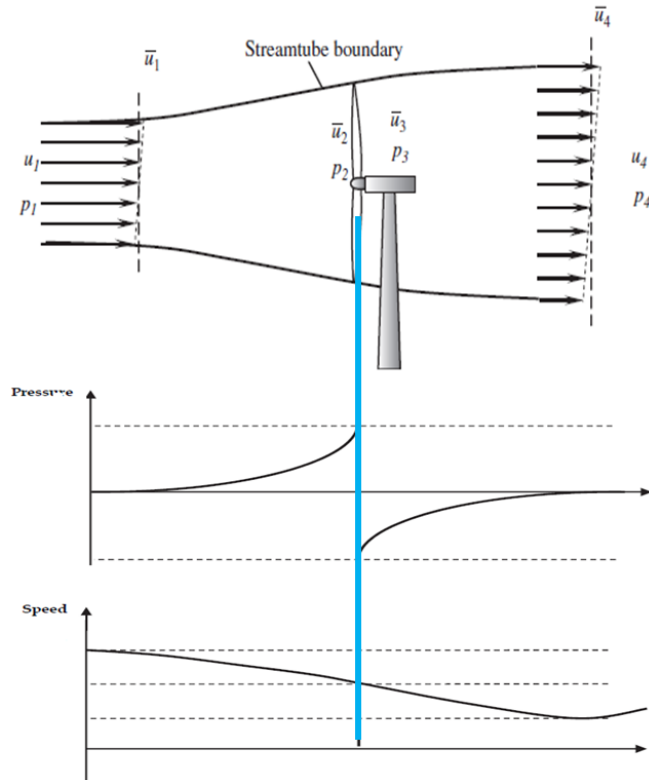


Figure 2.3: Pressure and speed variation in an ideal model of wind turbine [13, 14]

To recap:

- \bar{u}_1 and \bar{u}_4 are mean velocities upstream and downstream from the wind turbine
- \bar{u}_2 and \bar{u}_3 are mean velocities just in front and back of the blades. Hypothetically, $\bar{u}_2 = \bar{u}_3$
- Hypothetically $p_1 = p_4 = p$, the pressure upstream and downstream from the wind turbine are equal to the static pressure of the undisturbed airflow

Hence with this simplification it can be derived that

$$p_2 - p_3 = 0,5 \rho (\bar{u}_1^2 - \bar{u}_4^2) \quad \text{Equation 2.8}$$

$$\bar{u}_2 = \bar{u}_3 = 0,5 (\bar{u}_1 - \bar{u}_4) \quad \text{Equation 2.9}$$

Rewriting the Equation 2.4 in a better way, the mechanical power (P_w) that the blades could draw is equal to [13]

$$P_w = \frac{1}{2} A \rho \bar{u}_2 (\bar{u}_1^2 - \bar{u}_4^2) = \frac{1}{2} A \rho \bar{u}_1^3 4 a (1 - a)^2 \quad \text{Equation 2.10}$$

A is the area swept by the rotor blades [m^2]

ρ_0 is the density of the air in state 0 [kg/m^3]

Where a is the axial induction factor, it is defined as follows

$$a = \frac{\bar{u}_1 - \bar{u}_2}{\bar{u}_1} \quad \text{Equation 2.11}$$

Introduce the axial induction factor in the Equation 2.7,

$$C_p = 4 a (1 - a)^2 \quad \text{Equation 2.12}$$

$$\frac{d C_p}{d a} = 12 a^2 - 8 a + 4$$

Equation 2.13

So, it is possible to deduce that when the axial factor is equal to 1/3 the power coefficient reaches its maximum value of 16/27, 59.26% [13]. The behaviour of the power coefficient with respect to the axial induction factor is explained in Figure 2.4.

However, in wind turbines there are other losses of energy that must be considered. The other main losses are due to [13]:

- the gearbox, of course there aren't this kind of losses in a direct drive wind turbine, η_{gear} .
- the generator, all electrical and mechanical losses in a generator such as iron, friction, and other miscellaneous, η_{gen} .
- the electric system, it encompasses all combined electric power losses in the converter, switches, controls and cables, η_{ele} .

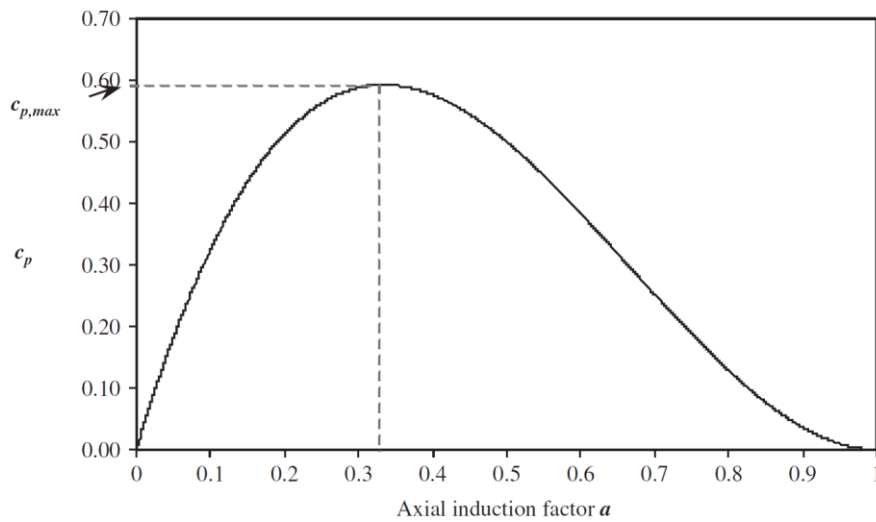


Figure 2.4: Power coefficient as a function of axial induction factor [13]

Hence, the total efficiency factor (η_t) of each wind turbine is equal to

$$\eta_t = C_p \eta_{gear} \eta_{gen} \eta_{ele}$$

Equation 2.14

C_p is the power coefficient

At the state of the art, the total efficiency factor is around 45% [15]. In a lot of studies, it can be possible to show the effect of the Tip Speed Ratio (TSR)

$$TSR = \lambda = \frac{\text{speed or rotor tip}}{\text{wind speed}}$$

Equation 2.15

on the wind turbine's efficiency [13, 15, 14, 16]. Figure 2.5 shows the relation between the power coefficient and the TSR in different kinds of wind turbines. The average 80 m wind speed in the world is around 5,9 m/s [17] so the most efficient rotor configuration is the three-bladed one. The most important wind farms (Roscoe Wind Farm USA, Gansu Wind Farm China, Stateline Wind Farm USA, ...) use this kind of configuration. However, in the windiest places on earth the most efficient designs are the two-blade and the one-blade rotor. They are both more efficient than the three-blades rotor when the wind speed is over 9 m/s. However, this kind of systems are very rare, and they don't have many applications. It is not possible to build three-blade turbines too close to city centres since they are too big, and the wind speed isn't high enough. Hence the need to adopt solutions like the Darrieus or Savonius turbine, even if their power coefficient is inferior to the three-blades ones. [15]

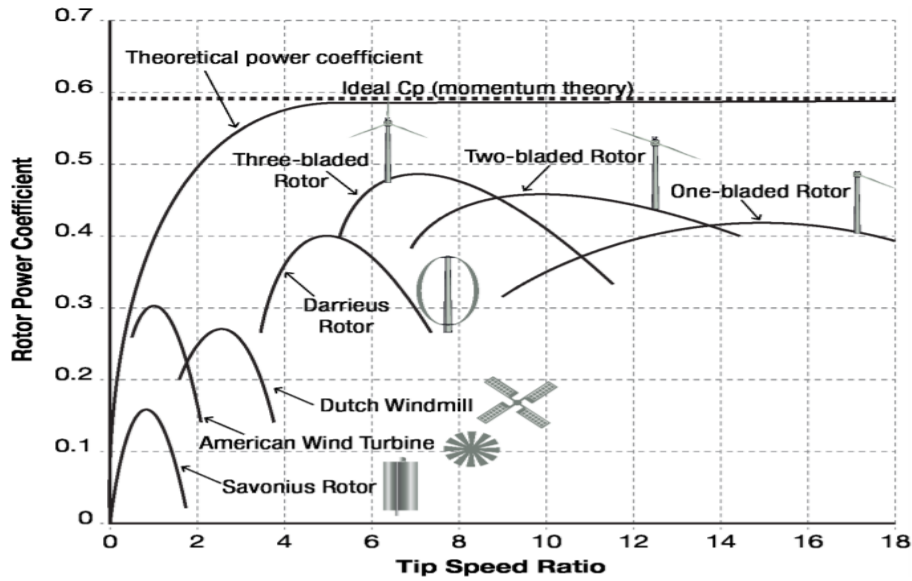


Figure 2.5: Power coefficient as a function of TSR [15]

2.3 Differences between Direct Drive and Gear Box Generators

The main difference between the direct drive generator and the gearbox one is that in the first case the hub is directly connected to the rotor, so that the rotor operates at the same speed as the turbine’s blades, while in the latter the hub is connected to a gearbox, in order to increase rotational speed from a low-speed rotor to a higher speed electrical generator. The necessity to remove the gearbox comes from the need to increase the turbine’s reliability (more than 50 % of the wind turbines’ failures are due to a combination failure of both the gearbox and the bearings [18]), especially in the case of offshore systems where the manufacturing is very frequent and expensive. But the downside to using direct drive instead of a gearbox system has been twofold: cost and weight. Figure: 2.6 shows the comparison in cost between two different kinds of 3MW turbine, DFIG 3G (Doubly-fed induction generator) with gearbox and PMSG DD (Permanent Magnet Synchronous Generator) without gearbox.

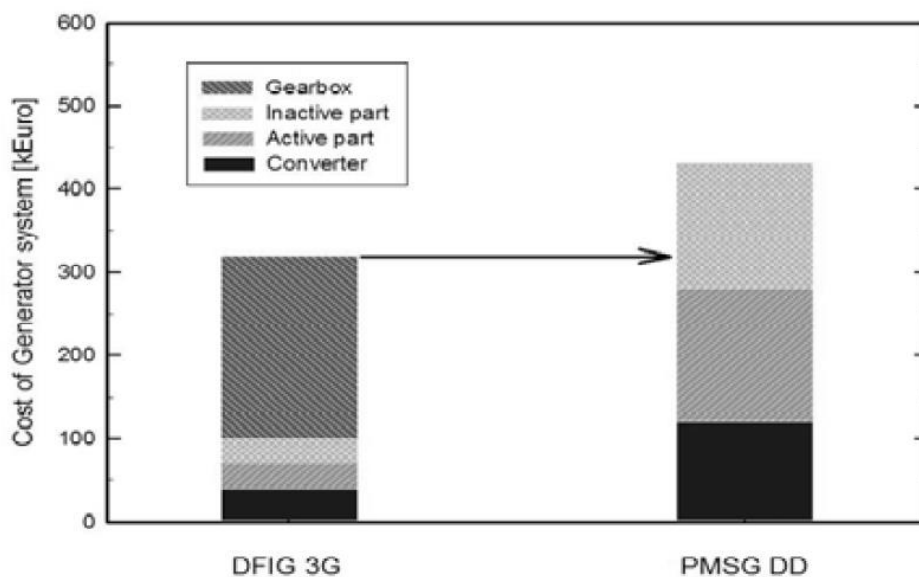


Figure: 2.6 Cost of 3 MW DFIG 3G and PMSG DD [36]

Figure 2.7 shows the different configurations of gearbox and direct drive systems.

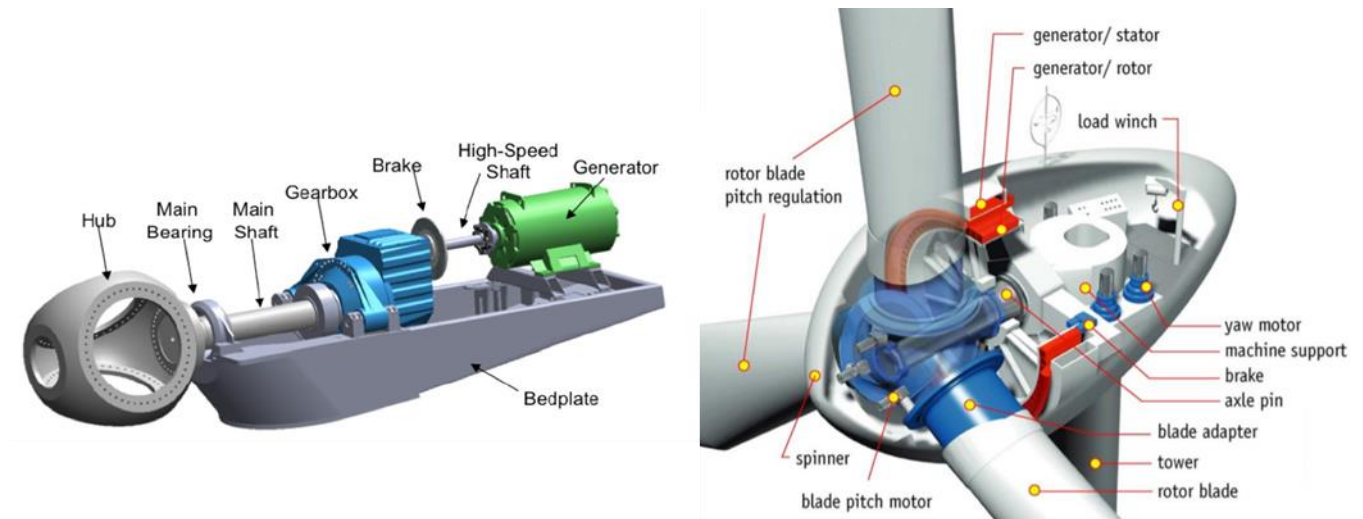


Figure 2.7: Gearbox and Direct Drive wind turbines [37, 38]

The generator is bigger in the second one and this can be one of the main problems in the direct drive wind turbine. In the gearbox wind turbine, the generator is isolated from external loads, wind loads, blades' weight and it is only subjected to centrifugal and magnetic loading and gearbox vibrations. For this reason, the structure of the stator and of the rotor aren't supposed to support big stress. In the direct drive wind turbine, the generator is subjected to extremely high dynamic loadings: wind loads, blades' weight, magnetic force, tower shadow effects, wind shear and turbine eccentricity, and their influence on the generator's structure is very high. For this reason, the direct drive generator must be built with materials which increase the generator's stiffness in controlling air gap displacements, but it means that the mass of the generator must be very high. The ideal distance between the rotor and stator is $1/1000$ of the air gap diameter, for instance with a 5m diameter air gap the distance between stator and rotor should be 5 mm. It is impossible to avoid an air gap displacement, but it is extremely important that the stator and the rotor are isolated from each other and that their relative distance doesn't become bigger than 20 % of this clearance. Otherwise the air gap flux density might vary significantly and thus affect electromagnetic forces and possibly add magnitude from other forces [19].

2.4 Main Cause of Air Gap Displacement

The main causes of air gap displacement are:

- Wind load
- Static and dynamic eccentricity
- Magnetic force
- Increase of temperature
- Centrifugal force
- Manufacturing /installation /material defect
- Gravity

2.4.1 Wind load

The wind load is the operative force in the wind turbine, so it is extremely important to evaluate it with precision. There are a lot of factors that make such evaluation extremely difficult (turbulence, air density, air temperature, environmental effects, geometry of the blades, ...)

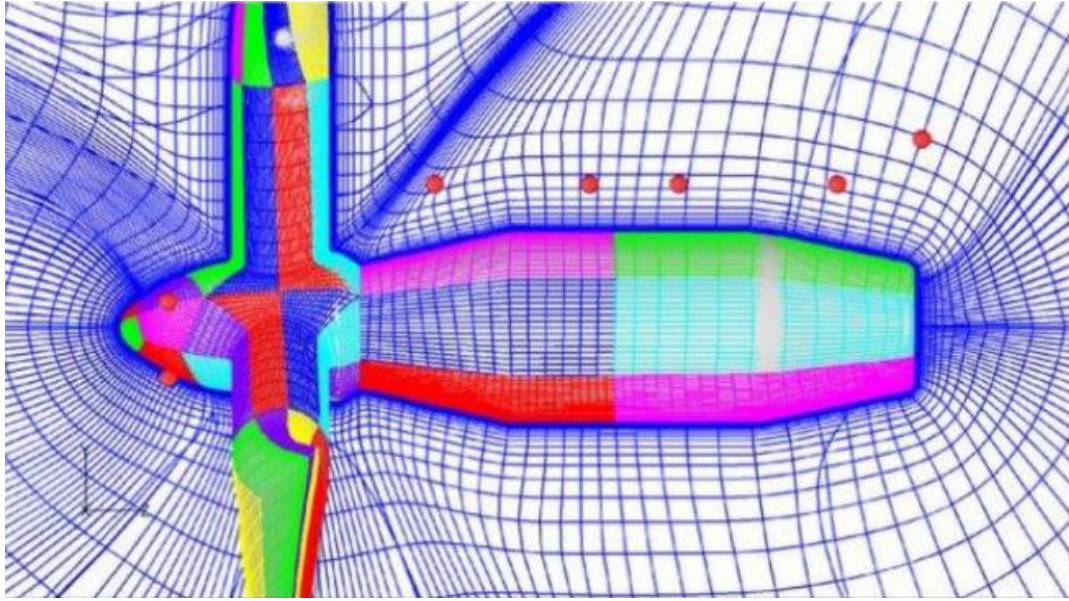


Figure 2.8: CFD model of wind turbine rotor

To study the loads from the wind the the most powerfull theory is the CFD (Computational fluid dynamics) theory. The idea of this theory is to subdivide the flow filed into small volume elements and solving the conservative equation for each element. It is clear that the output result in function of the input theory. For instance Euler equations has no boundary layers but has spatially transiently motion, Euler equation with boundary layers equation can analys the laminar and turbolent flow but it has not flow separation, Navier-Stocks equations can studie laminar and turbulence flow, and the result depend about the turbulence model (it is very accurated model but also very expansive). Wind shear and tower shadow are both external disturbances which come from wind power variations due to a periodic reduction of mechanical torque at the frequency called 3p frequency. The 3p frequency is a source of vibration due to rotational sampling as each blade passes the tower. It could be dangerous if it is too close to the frequency range associated with inter-area, it might be a source of forced oscillations than can exite system resonance [20]. They can be calculated as [21]

$$v_m(r, \psi) = \alpha \left(\frac{r}{h}\right) \cos(\psi) + \frac{\alpha(\alpha - 1)}{2} \left(\frac{r}{h}\right)^2 \cos^2(\psi) + \frac{\alpha(\alpha - 1)(\alpha - 2)}{6} \left(\frac{r}{h}\right)^3 \cos^3(\psi) \quad \text{Equation 2.16}$$

$$v_t(r, \psi, x) = \frac{a^2(r^2 \sin^2(\psi) - x^2)}{(r^2 \sin^2(\psi) + x^2)^2} \quad \text{Equation 2.17}$$

v_m is the wind shear vatiation [m/s]

α is the empirical wind shear exponent

r is the blade length [m]

h is the height of tower [m]

ψ is the blade azimuthal angle [rad]

v_t is the tower shadow disturbance [m/s]

x is the distance of blade origin from the tower midline [m]

a is the tower radius [m]

The first one is the wind shadow variation speed and the second one is the tower shadow disturbance speed.

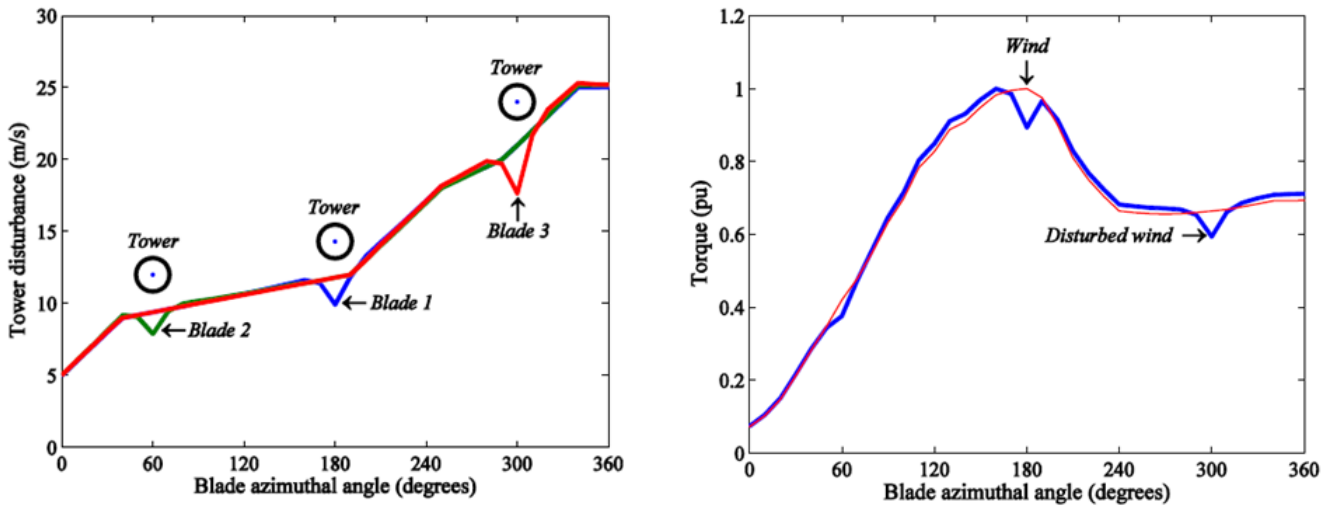


Figure 2.9: Wind speed and torque on the tower as function of the blade azimuthal angle under the effect of tower shadow and wind shear [21]

Is not difficult to understand that the wind shear effect decreases when the tower’s height increases and the tower shadow effect is present only in a range between $90^\circ < \psi < 270^\circ$.

In this thesis, I have compared the static effect of gravity, wind load and the magnetic force with and without the contribution of the bearings. The second step has been a multi body dynamic analysis with the wind shear and the tower shadow effect. The result is showed I n the following chapter.

2.4.2 Static and Dynamic eccentricity

The eccentricity is the misalignment between the rotor and stator axis, there are two kinds of eccentricity: static eccentricity and dynamic eccentricity, Figure 2.10. Static eccentricity happens when the rotor turns around its own rotation axis but it’s dislocated with respect to the stator axis. Dynamic eccentricity happens when the centre of the rotor’s axis is the same as the stator’s one, but it does not correspond to the rotation axis of the rotor. Of course these two phenomena can exist together [22].

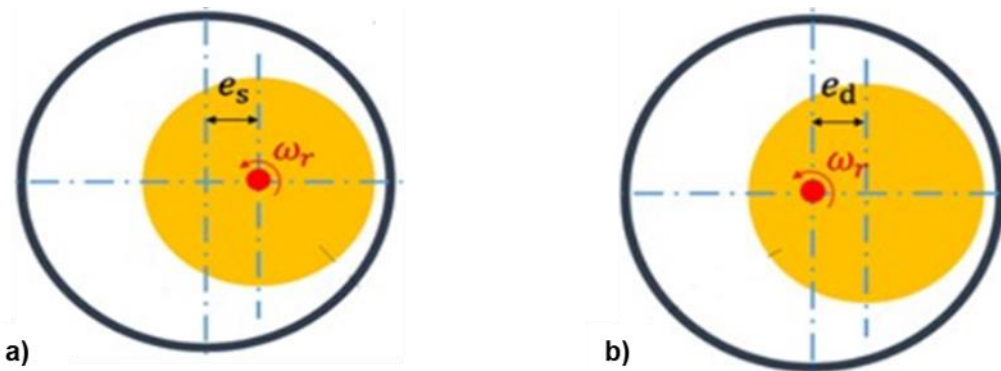


Figure 2.10: Static and dynamic eccentricity

Eccentricity in wind turbines could be dangerous for two reasons, first of all it increases vibration of the system which could cause a critical failure in the system. Then the air gap could be modified due to a change in the air flux density. An increase of 20% of the density brings an increase of 44% of unbalanced magnetic Pull (UMP) in the direction of the smallest air gap [22]. For this reason, eccentricity must remain under a certain limit. Other result of rotor eccentricity is bearing wear it means that the real operation life of the bearing could be less than the project operation life.

2.4.3 Magnetic Force

The interaction between the permanent magnets on the rotor's surface and the iron of the stator produces an attractive force between the rotating and static parts of the generator. This kind of force acts perpendicular and tangential to the air gap. The magnetic force can be calculated in its normal and tangential components by the Maxwell's stress tensor theory as a function of the magnetic field strength between stator and rotor as [23]

$$\sigma_F = 0,5 \mu_0 H^2 \quad \text{Equation 2.18}$$

$$\sigma_{Fn} = 0,5 \mu_0 (H_n^2 - H_{tan}^2) \quad \text{Equation 2.19}$$

$$\sigma_{Ftan} = \mu_0 H_n H_{tan} \quad \text{Equation 2.20}$$

σ_F is the stress due to the magnetic field [N/m^2]

σ_{Fn} is the normal component of the stress due to the magnetic field [N/m^2]

σ_{Ftan} is the tangential component of the stress due to the magnetic field [N/m^2]

μ_0 is the permeability of free space, it is equal to $4 \pi 10^{-7} [N/A^{-2}]$

H is magnetic field strength [m/A]

H_n is normal component of magnetic field strength [m/A]

H_{tan} is tangential component of magnetic field strength [m/A]

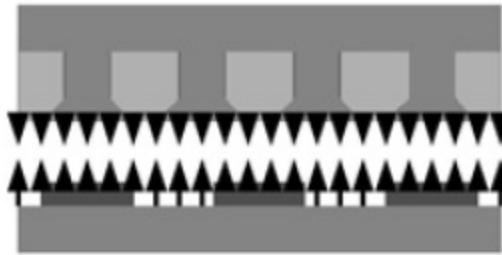


Figure 2.11: Generic section with normal stress, across the airgap [24]

When a large airgap flux density is used, like in a direct drive wind generator, the normal stress is about ten times than the tangential stress, it means that the tangential stress can be neglected [24].

To regard Figure 2.12 Figure 2.11 in the first case the UMP should be equal to zero because the air gap has symmetrical distribution around all generator, in the other case, Figure 2.12.b, in the yellow region the distance between statro and rotro is smaller than in the other region, due to it born a magnetic force from the center to the rotor to the air gap's smallest region in radial direction [25]. This force (F_{UMP}) can be calculated as [25]

$$F_{UMP} = \frac{DL}{4\mu_0} B_m^2 \delta(x) \int_0^\vartheta \sin(\vartheta)^2 d\vartheta \quad \text{Equation 2.21}$$

$$\delta(x) = e/g \quad \text{Equation 2.22}$$

D is the air gap diameter [m]

L is the air gap length [m]

B_m is the magnetic field [T] or [$kg s^{-2} A^{-1}$]

ϑ is the angular position on the air gap regard to Figure 2.12 [rad]

e is the distance of rotor centre from stator centre [m]

g is the air gap size in the symmetrical configuration [m]

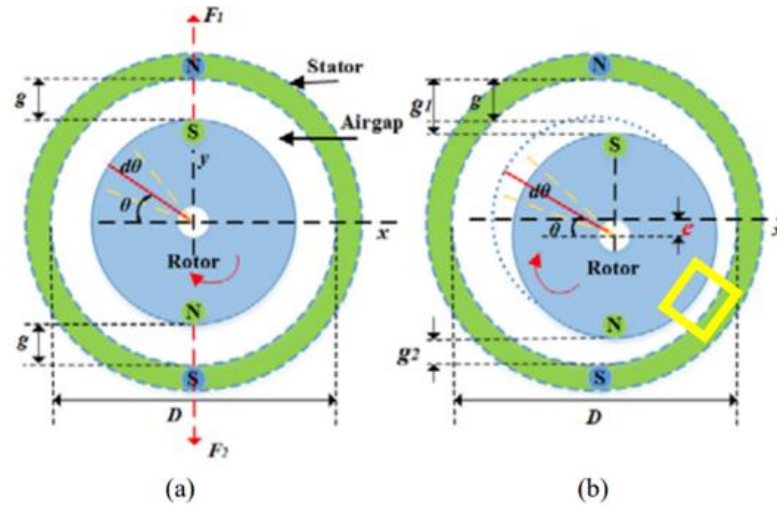


Figure 2.12: UMP in: symmetrical machine (a); with rotor displaced vertically downwards [25]

2.4.4 Increase of temperature

The generator is a machine that generates energy, so it also generates heat (first thermodynamically law). The heat leads to a temperature rise in different machine parts, all these temperature rises, falls and different rates of change can produce differential thermal expansion and contraction. Heat can be transferred from one place to another by three methods: conduction (it happens when two surfaces with different temperature are in touch, it is a physical process without movement of material), convection (it is the heat transfer due to the bulk movement of molecules within fluids such as gases and liquids, it is a physical process with movement of material) and radiation (it is the transfer of energy by means of photons in electromagnetic waves). Obviously, the convection is the main method of heat transfer in the air gap. In Figure 2.14 is shown the impact of the temperature rise in an inner-rotor generator. Newton's laws and the displacement of air gap can as [23] [24].

$$\Phi_{conv} = -k \Delta T \quad \text{Equation 2.23}$$

$$\Delta L = L_0 k \Delta T \quad \text{Equation 2.24}$$

Φ_{conv} is the heat flux [W/m^2]

k is the heat transfer coefficient [$W/(m^2K)$]

ΔT is the difference in temperature between the two surfaces [K]

ΔL is the air gap displacement due to the temperature [m]

L_0 is the initial length between stator and rotor [m]

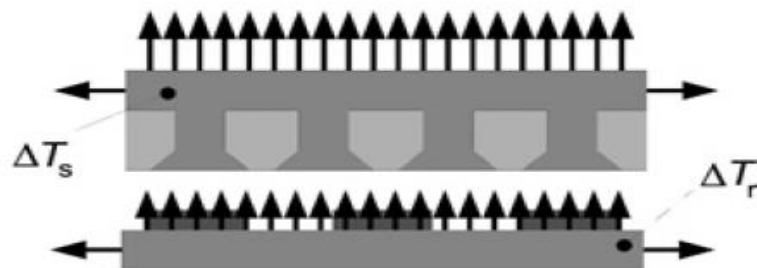


Figure 2.13: Expansion due to temperature rises in the stator (ΔT_s) and rotor (ΔT_r) in a radial flux machine
In the research [23] the authors have studied the temperature of a stator in a 2,5-kW outer rotor direct drive.

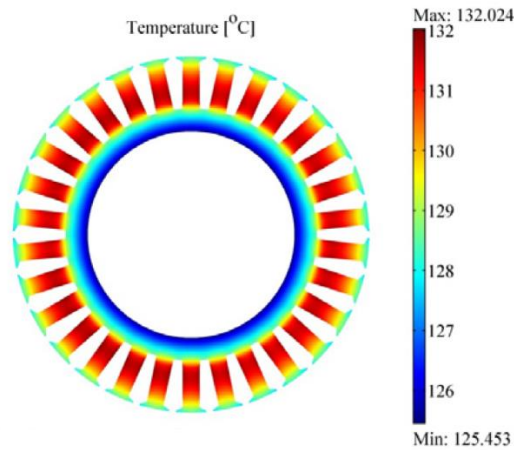


Figure 2.14: Stator temperature distribution in an outer rotor direct drive 2,5 kW [23]

They have found that the differential temperature of the component could be around 10 Celsius degree, with the maximum temperature in the bars of the stator, Figure 2.14 shows their results.

2.4.5 Centrifugal force

The magnitude of the centrifugal force (F_c) can be calculated by the second law of Newton and the definition of angular velocity (ω), as

$$F_c = m a_c \tag{Equation 2.25}$$

$$a_c = v \omega = \frac{v^2}{r} \tag{Equation 2.26}$$

m is the mass of the rotor [kg]

a_c is the centrifugal acceleration [m/s^2]

v is the rotor velocity in radial direction [m/s]

ω is the rotor angular velocity [rad/s^2]

r is the rotor radius [m]

Putting together the Equation 2.25 and the Equation 2.26, it is possible to write the centrifugal force as

$$F_c = m v \omega = \frac{m v^2}{r} \tag{Equation 2.27}$$

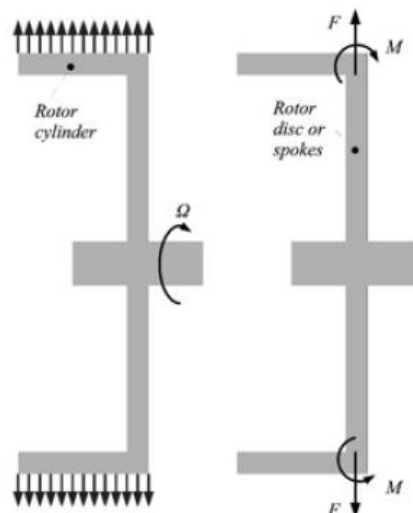


Figure 2.15: Effect of centripetal force in a radial-flux machine [24]

In the Figure 2.16 is shown the impact of the centrifugal force on the airgap.

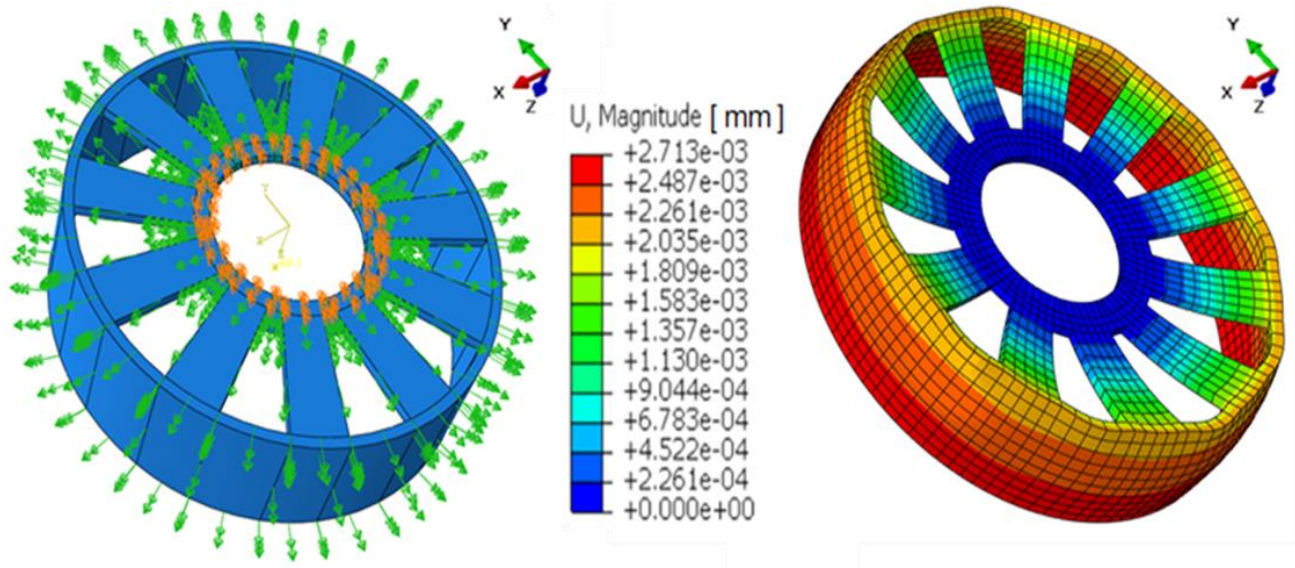


Figure 2.16: Centrifugal force on the rotor surface and rotor deflection

However, a normal direct drive wind turbine works with a speed around 12 rpm (1,5708 rad/s) [16], this rotational velocity leads to a centrifugal force that acts on the rotor surface and it is perpendicular to the air gap. However, the centrifugal force in a gear-less wind turbine has not a high impact on the behaviour of the air gap, in the following figure it is evident that the rotor's deflection is only $2,713 \cdot 10^3 \text{ mm}$.

2.4.6 Gravity

Gravity acts vertically during operation and its acceleration is equal to 9,81 m/s and of course, the stronger the gravity force the higher the mass. Gravity force (\vec{F}_g) can be determined by Newton's second law as

$$\vec{F}_g = m \vec{g} \tag{Equation 2.28}$$

m is the mass of the wind turbine [kg]

\vec{g} is the gravitational acceleration, it is equal to 9.81 [m/s²]

Nevertheless, the wind turbine generator's axis makes an angles to the horizontal (normally it is equal to 5 degree), it means that gravity acts on the generator in two ways: there is a major and a minor component as shown in Figure 2.17. The two different components of the gravity force can be calculated as

$$F_{g,x} = m g \sin(\Psi) \tag{Equation 2.29}$$

$$F_{g,y} = m g \cos(\Psi) \tag{Equation 2.30}$$

$F_{g,x}$ is the x component of gravity force [N]

$F_{g,y}$ is the y component of gravity force [N]

Ψ is the angle between x and y components [rad]

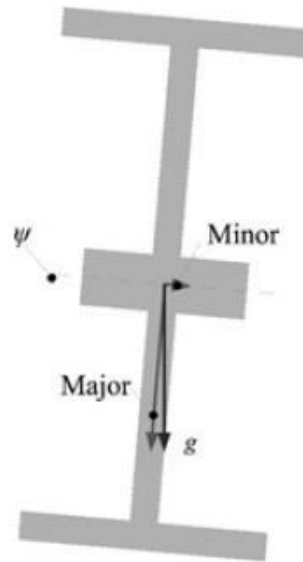


Figure 2.17: The major and the minor component of gravity [24]

2.4.7 Manufacturing/ Installation defect

The failures due to the manufacturing defect are very difficult to predict, it is impossible to make a mathematical model of the human error. In the Figure 2.18 is showed the percentaul of the possible failure and their own consequence.

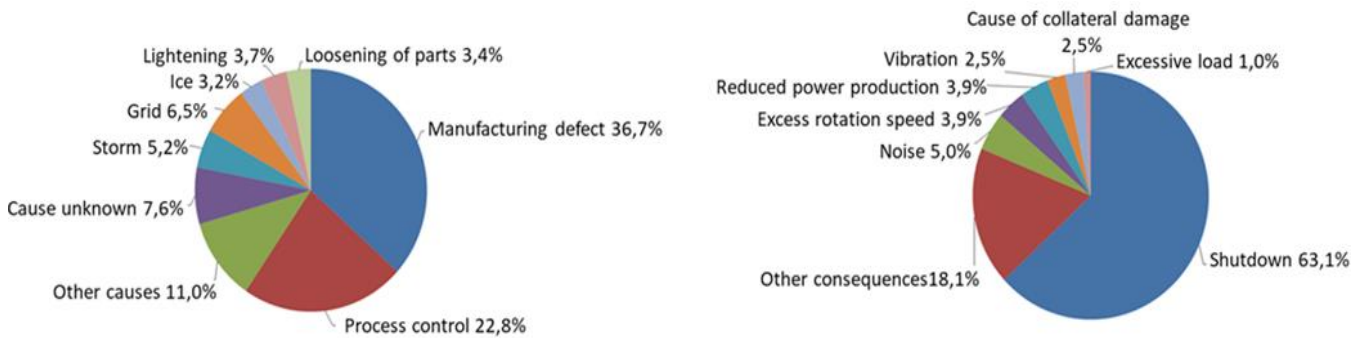


Figure 2.18: Failure Causes & Failure consequences [41]

It is clear that the manufacturing defect is the main cause of failure (36%) and its consequence is often the shutdown of the system (63.1%). Regard to the air gap the main problem of the manufacturing is the disalignment between the stator and rotor axis because a different distance between stator and rotor means a decrease in efficiency.

3. Mathematical theory

This chapter explains the mathematical theories that are been implemented by the calculator in order to resolve the static and dynamic problem. The first section is focused on the Finite Elements Method (FEM) which is been used to modulation the geometry of the generator in ABAQUS in order to make the static analysis and to prepare the model for the freedom reduction in SIMPACK. Then the Multi Body Simulations theory (MBS) is explained, this mathematical theory is been used to study the dynamic problem. At the end of this chapter, it is explained the Modal Assurance Criterion (MAC), it is showed how to import a FEM model from ABAQUS in a MBS model in SIMPACK.

3.1 Finite elements method

The finite elements method is a mathematical tool designed to simplify the geometry of the structure which has to be studied in order to find an approximate solution of problems of various physical nature, and that lends itself well to being automated. The basic concept is to cut the structure in a finite number of elements (pieces of the structure), whose geometry is simpler than the geometry of the beginning model, the properties of the different elements are explained at the end of this section. Then the equations that describe the behaviour of the body are solved for each element, the equations are solved for each node of the element. This process results in a set of simultaneous algebraic equations that describe the approximated behaviour of the real system. In this thesis the FEM. theory was used only for describe be displacement of the structure, so it follows only the mathematical theory for the displacement behaviour.

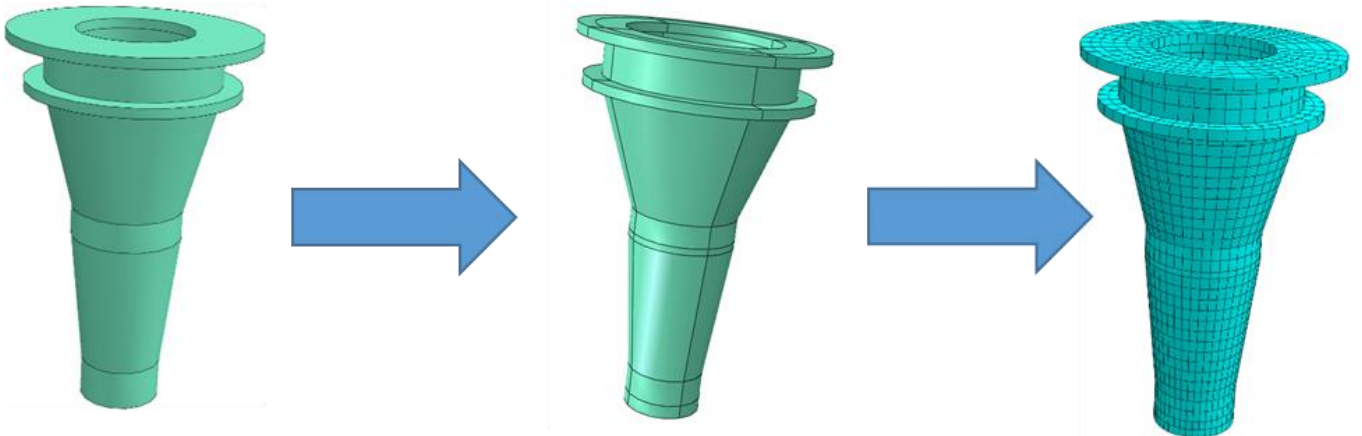


Figure 3.1: Steps to create a FEM system: CAD, partition CAD, meshing

The potential elastic energy (Φ , Equation 3.1) the kinetic energy (E_k , Equation 3.2) and the potential energy (U , Equation 3.3) can be expressed as [26]

$$\Phi = \frac{1}{2} \int_V \{\bar{\sigma}\}^T \{\bar{\varepsilon}\} dV \quad \text{Equation 3.1}$$

$$E_k = \frac{1}{2} \int_V \{\dot{\bar{u}}\}^T \rho \{\dot{\bar{u}}\} dV \quad \text{Equation 3.2}$$

$$U = - \left(\int_V \{\bar{u}\}^T \{\bar{X}_v\} dV + \int_S \{\bar{u}\}^T \{\bar{X}_s\} dS \right) \quad \text{Equation 3.3}$$

dV is an infinitesimal volume of integration [m^3]

dS is an infinitesimal surface of integration [m^2]

$\{\bar{\sigma}\}$ is the stress strain vector [N/m^2]

$\{\bar{\varepsilon}\}$ is the strain components vector

$\{\bar{u}\}$ is the displacement of the body in the space [m]

$\{\dot{\bar{u}}\}$ is the velocity of the body [m/s]

ρ is the density of the body [kg/m³]

$\{\hat{X}_v\}$ is the volumetric constant elastic [N/m³]

$\{\hat{X}_S\}$ is the surface constant elastic [N/m²]

The last equations can be discretized for each element as

$$\Phi^{(e)} = \frac{1}{2} \{\bar{q}^{(e)}\}^T [K^{(e)}] \{\bar{q}^{(e)}\} \quad \text{Equation 3.4}$$

$$E_k^{(e)} = \frac{1}{2} \{\dot{\bar{q}}^{(e)}\}^T [M^{(e)}] \{\dot{\bar{q}}^{(e)}\} \quad \text{Equation 3.5}$$

$$U^{(e)} = \{\bar{q}^{(e)}\}^T \{F^{(e)}\} \quad \text{Equation 3.6}$$

Where:

- the stiffness matrix, $[K^{(e)}]$ Equation 3.7, contains the geometric and material behaviour information that indicates the resistance of the element to deformation when subjected to loading [26].
- the mass matrix, $[M^{(e)}]$ Equation 3.8, contains the information about the mass whose is concentrated at the element nodes [26].
- the force vector, $\{F^{(e)}\}$ Equation 3.9, representing a distributed nodal load on the basis of work equivalence [26].
- the generalized coordinates vector, $\{\bar{q}^{(e)}\}$, representing the degrees of freedom of the system.

$$[K^{(e)}] = \int_{V^{(e)}} [B^{(e)}]^T [C^{(e)}] [B^{(e)}] dV \quad \text{Equation 3.7}$$

$$[M^{(e)}] = \int_{V^{(e)}} \rho [N^{(e)}]^T [N^{(e)}] dV \quad \text{Equation 3.8}$$

$$\{F^{(e)}\} = \int_{V^{(e)}} \rho [N^{(e)}]^T \{\hat{X}_v\} dV + \int_{S^{(e)}} [N^{(e)}]^T \{\hat{X}_S\} dV \quad \text{Equation 3.9}$$

$\{\hat{X}_v\}$ is the volumetric constant elastic [N/m³]

$\{\hat{X}_S\}$ is the surface constant elastic [N/m²]

$[C^{(e)}]$ is the matrix of the elastic stiffness coefficient for every elements

$[B^{(e)}]$ is the matrix that connects the linear part of the strain array to the displacement

$[N^{(e)}]$ is the interpolation matrix

$\{F^{(e)}\}$ is the force vector for every elements [N]

Using the Lagrange's equation, Equation 3.10, it can be possible obtained the equation of motion, Equation 3.11

$$\frac{\partial}{\partial t} \left(\frac{\partial E_k^{(e)}}{\partial \dot{\bar{q}}^{(e)}} \right) + \frac{\partial \Phi^{(e)}}{\partial \bar{q}^{(e)}} + \frac{\partial U^{(e)}}{\partial \bar{q}^{(e)}} = 0 \quad \text{Equation 3.10}$$

$$[M^{(e)}] \{\ddot{\bar{q}}^{(e)}\} + [K^{(e)}] \{\bar{q}^{(e)}\} + \{F^{(e)}\} = 0 \quad \text{Equation 3.11}$$

However, the degree of freedom of this kind of system are too many and the calculation time is too expansive. Through the rotation matrix $[\lambda]$ it can be possible reduce all equations in an only global reference system and then it can be made the assembly of all information from each element. Following the global matrix needed

for the assembly and the equation of motion in the global coordinates system.

$$[M] = [\lambda]^T [M^{(e)}] [\lambda] \quad \text{Equation 3.12}$$

$$[K] = [\lambda]^T [K^{(e)}] [\lambda] \quad \text{Equation 3.13}$$

$$\{F\} = [\lambda]^T \{F^{(e)}\} \quad \text{Equation 3.14}$$

$$[M] \{\ddot{\bar{q}}\} + [K] \{\bar{q}\} + \{F\} = 0 \quad \text{Equation 3.15}$$

$[\lambda]$ is rotational matrix

$[M]$ is the mass matrix of the whole system

$[K]$ is the stiffness matrix of the whole system

$\{F\}$ is the forces and torques vector of the whole system

For the static general problem ABAQUS use the concept of the “minimum total potential energy” [27]. It states that “Of all displacement states of a body or structure, subjected to external loading, that satisfy the geometric boundary conditions (imposed displacements), the displacement state that also satisfies the equilibrium equations is such that the total potential energy is a minimum for stable equilibrium “ [26]. Hence,

$$\frac{\partial \Pi}{\partial \bar{q}} = \frac{\partial(\Phi+U)}{\partial \bar{q}} = [K]\{\bar{q}\} + \{F\} = 0 \quad \{\bar{q}\} = -[K]^{-1}\{F\} \quad \text{Equation 3.16}$$

$\frac{\partial \Pi}{\partial \bar{q}}$ is the partial derivate of potential energy

Φ is the potential elastic energy [J]

U is the poten

For the modal analysis the external loads are neglected, $\{F\} = 0$, that means the Equation 3.15 becomes as

$$[M] \{\ddot{\bar{q}}\} + [K] \{\bar{q}\} = 0 \quad \text{Equation 3.17}$$

To determine the natural frequencies and mode shapes of the system’s vibration modes, the generalized coordinate vector ($\{\bar{q}\}$) is supposed to be an exponential function as

$$\{\bar{q}\} = \{A_q\} e^{i \omega t} \quad \text{Equation 3.18}$$

$\{A_q\}$ is the mode shape vector

ω is the natural frequency of the system

Replacing the Equation 3.18 in the Equation 3.17 it gets the formula for free non-damped oscillation

$$(-\omega_j^2 [M] + [K]) \{A_q\}_j e^{i \omega t} = \{0\} \quad \text{Equation 3.19}$$

Where ω_j is the j-th natural frequency of the system and $\{A_q\}_j$ is the mode shape vector for the j-th natural frequency.

3.1.1 Type of elements

The FEM elements can be divided in two categories: the quadratic elements (second order) and the linear elements (first order). This last two categories can be divided in three other categories: Tetrahedral elements, Wedge elements and Hexagonal elements. In the Table 3.1 are posted all the possible combination between these categories.

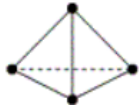
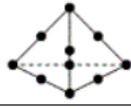
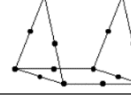
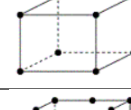
Element	Order	Number of nodes	Sigla	Geometry
Tetrahedral	1 st	4	C3D4	
	2 nd	10	C3D10	
Wedge	1 st	6	C3D6	
	2 nd	15	C3D15	
Hexagonal	1 st	8	C3D8	
	2 nd	20	C3D20	

Table 3.1: F.E.M. elements in ABAQUS

A removed mid-side node implies that the edge is and remains straight, resulting in a corresponding increase in the stiffness. It is recommended that elements with removed nodes be used only in transition regions and not where simpler linear elements with added shape functions will do.

With the same number of elements one mesh with Hexagonal elements given best result than one mesh with Tetrahedral elements but the Hexagonal elements can't be used when the geometry of the component is too complex, in that case the Hexagonal elements give a mesh distortion too high. The main problem in the 1st order elements is that due to the missed nodes during the deformation the energy going into the shearing the element rather than bending, this behaviour is called Shear locking. In the 2nd order elements there isn't the Shear locking because the element edges can assume a curved shape, that means the angle between the deformed isoperimetric lines remains 90°. For this regains the 1st order elements must not use in regions dominated by bending. In Figure 3.2 is showed the comparison between the Hexagonal elements 1st order and 2nd order loaded by a bending moment.

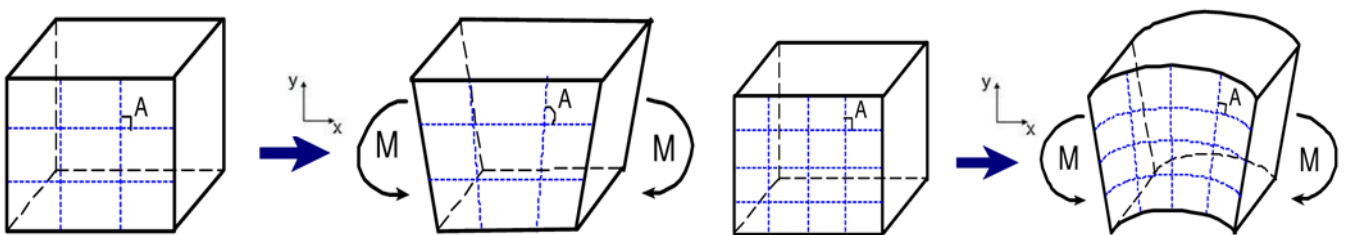


Figure 3.2: Shear locking: 1st order element $\gamma_{xy}=0$ $\sigma_{xy}=0$; 2nd order element $\gamma_{xy}\neq 0$ $\sigma_{xy}\neq 0$

The 2nd order normally has less problem than the 1st order: it goes quickly to convergence, it minimizes the shear and volumetric locking, it is robust during finite deformation and it uniforms contact pressure that means it allows to model contact accurately.

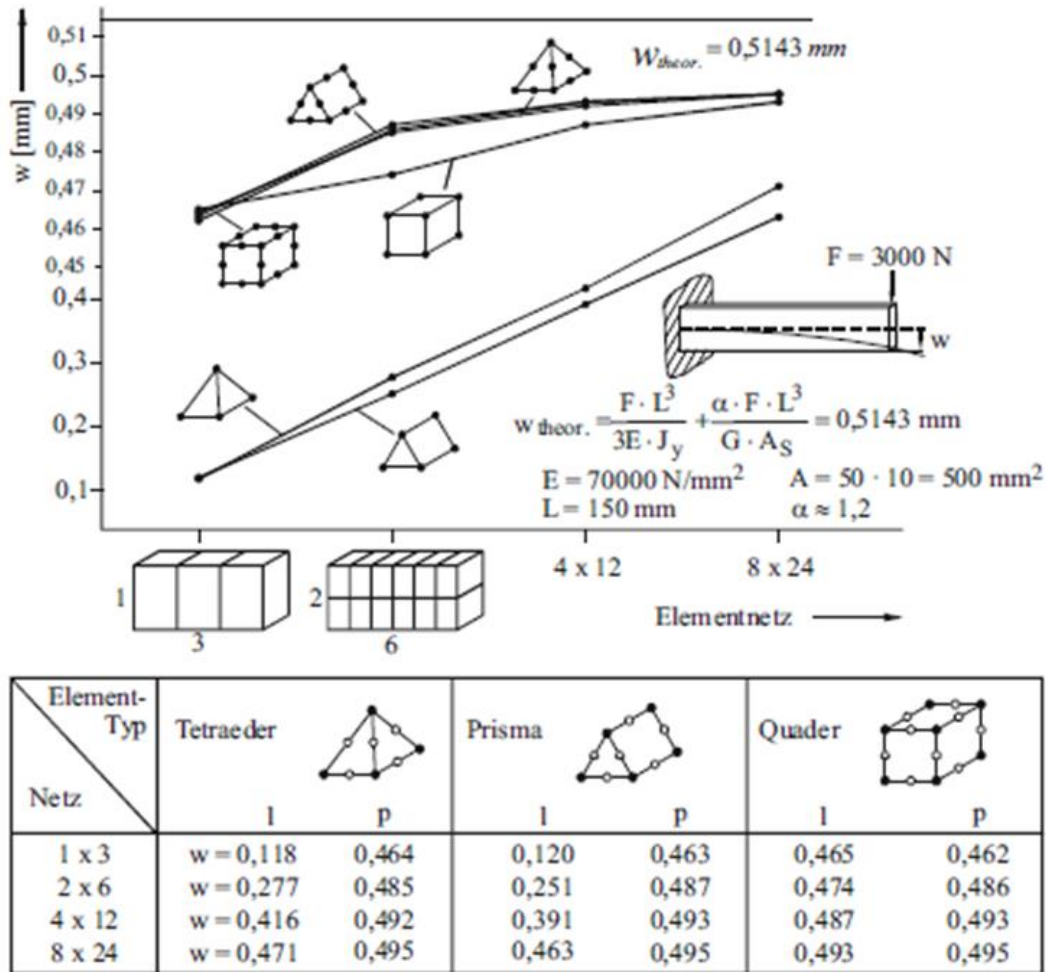


Figure 3.3: Convergence analysis for the finite elements mesh [26]

In Figure 3.3 it is showed a convergence analysis to a mesh of a beam stuck on one side and charge in the other side with a load equals to 3000 N. It is clear the high stiffness of the 1st order elements, the beam's displacement with a mesh of 1st order elements is very less than the beam's displacement with the same number of elements in the mesh but with 2nd order elements. It is also clear that the 2nd order elements go to convergence fast, whereas the 1st order elements go to convergence very slowly.

3.2 Multi Body simulation

A multi body system consist s of mass-inherent rigid bodies, which are connected by joints, springs, damper and positioning elements. The main propose of the multi body simulation is to find the minimal model deep that realise the physical processes in a system with the smallest number of degrees of freedom and parameters possible, in order to make the interpretation of the simulation results quite easy. In the first section of this chapter are describe the model elements, after the Lagrange equation of 1st kind and the eigen behaviour are described and the last part the different possibility to make a flexible body in SIMPACK are illustrated.

3.2.2 Model elements

In the Figure 3.4 is showed a general multi body system with all kind of model elements possible.

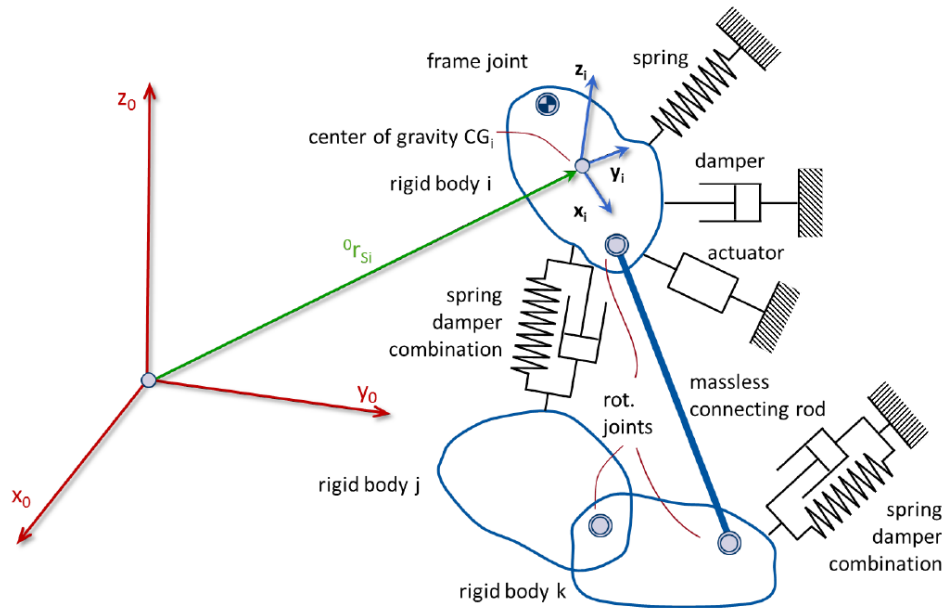


Figure 3.4: Example of Multi Body System [28]

The rigid body is the model elements responsible for the mass and the moment of inertia of the physical system. It can be punctiform or it can have a geometrical extension, but in both cases the all mass of the system is concentrated in the centre of mass and it is a scalar quantity. The moment of inertia can be represented by a scalar quantity only if the system is 2D in the other case it must be represented by a tensor. Every rigid body has each own reference system that displays the spatial position and orientation of the body (ex. Reference system 1 in Figure 3.4). The constraint elements enforce certain motion the body and they locked some degrees of freedom of the system and they cause force within the system indirectly in form of reactions. Some example of constraint elements are bearings, prismatic pairs, revolute pairs, frame joint rotational joint and massless connecting road. The constraint elements cab be described by the constraint function, which establish the correlation between the coordinates system of two bodies. By the constraint function it is possible describe the position and the orientation of the fully bodies in the multi bodies system. The constraint can the classified as [28]:

- geometrical and kinematic constraints. The geometrical constraint locks the position of the system, it can be display as Equation 3.20. The kinematic constraint act on the velocity of the system, if it is not zero and it can display as the Equation 3.21;

$$\vec{g}(\vec{r}, t) = 0 \tag{Equation 3.20}$$

$$\vec{g}(\dot{\vec{r}}, \vec{r}, t) = 0 \tag{Equation 3.21}$$

- single-sided and double-sided constraints. The Equation 3.20 and the Equation 3.21 are both double-sided constraints, a constraint is a single-sided if the system can quit the constraint in only one direction. It means:

$$\vec{g} < 0 \text{ or } \vec{g} > 0 \tag{Equation 3.22}$$

- scleronomic and arheonomic constraints. If the constraint function is time-variant the constraint is called arheonomic, if the constraint function is time-invariant the constraint is called
- holonomic and non-holonomic constraints. A constraint is called holonomic if its constraint function is depending on the position and on the velocity, but the velocity can be integrable. If the velocity is in non-integrable form the constraint is called non-holonomic. It means that a kinematic constraint is holonomic only it is possible to make the integer of its velocity.

The interlinking element, opposite to the behaviour of the constraint elements, cause active force of the system. The most commune interlinking elements are spring, damper and actuator. Active forces can depend on the mass, or on the inertia respectively, and on the position or orientation of a body in a multibody system. Additionally, they can depend on other physical quantities (for instance spring constant, damping constant, acceleration due to gravity, electric field strength, magnetic flux) [28].

3.2.3 Lagrange equation 1st kind

MBS software (as SIMPACK) studies the behaviour of the system by a set of different ordinary equation (ODE) that are resolved by numerical solution. The most common method uses by calculator to describe the motions of a mechanical system under the action of forces is the Lagrange equation of 1st kind [28].

Equation 3.23 define the position vector (\vec{r}_i) of a body in absolute coordinates and its derivates ($\dot{\vec{r}}, \ddot{\vec{r}}$)

$$\vec{r}_i = \begin{pmatrix} \vec{r}_{i,tra} \\ \vec{r}_{i,rot} \end{pmatrix} = \begin{pmatrix} x \\ y \\ z \\ \alpha \\ \beta \\ \gamma \end{pmatrix}_i \quad \dot{\vec{r}} = \begin{pmatrix} \dot{\vec{r}}_{i,tra} \\ \dot{\vec{r}}_{i,rot} \end{pmatrix} = \begin{pmatrix} \dot{x} \\ \dot{y} \\ \dot{z} \\ \dot{\alpha} \\ \dot{\beta} \\ \dot{\gamma} \end{pmatrix}_i \quad \ddot{\vec{r}} = \begin{pmatrix} \ddot{\vec{r}}_{i,tra} \\ \ddot{\vec{r}}_{i,rot} \end{pmatrix} = \begin{pmatrix} \ddot{x} \\ \ddot{y} \\ \ddot{z} \\ \ddot{\alpha} \\ \ddot{\beta} \\ \ddot{\gamma} \end{pmatrix}_i \quad \text{Equation 3.23}$$

Equation 3.24 and Equation 3.25 show the two equation at the base of each numerical method to study a mechanical system nature, receptivity the Newton equation and the Euler equation.

$$m_i \vec{v}_{si} = \vec{f}_i = \vec{f}_i^e + \vec{f}_i^z \quad \text{Equation 3.24}$$

$$\vec{L}_i = \vec{m}_i = \vec{m}_i^e + \vec{m}_i^z = \vec{I}_i \vec{\omega}_i + \vec{\omega}_i \vec{I}_i \vec{\omega}_i \quad \text{Equation 3.25}$$

m_i is the mass of the body [kg]

\vec{v}_{si} is the vector of the acceleration of the centre of gravity of the body [m/s^2]

\vec{f}_i is the vector of total forces acting on the centre of gravity [N]

\vec{L}_i is the vector of angular momentum of a rigid body relative to the centre of gravity [$kg \ m^2/s$]

\vec{m}_i is the rate of change of the angular momentum of a rigid body relative to the centre of gravity

\vec{I}_i is the inertial tensor

$\vec{\omega}_i$ is the vector of the angular acceleration [rad/s^2]

$\vec{\omega}_i$ is the vector of the angular velocity and $\vec{\omega}_i \vec{I}_i \vec{\omega}_i$ is the skew symmetric matrix of the angular velocity [m/s]

\vec{f}_i^e and \vec{m}_i^e are the vector of external forces and torques [N] [Nm]

\vec{f}_i^z and \vec{m}_i^z are the vector of the internal force and torque [N] [Nm]

\vec{E} is the identity matrix

Writing the Equation 3.24 and the Equation 3.25 in matrix form (Equation 3.26) is achieved the equation of motion for one body.

$$\begin{bmatrix} m\vec{E} & \vec{0} \\ \vec{0} & \vec{I}_i \end{bmatrix} \begin{Bmatrix} \vec{v} \\ \vec{m}^e \end{Bmatrix}_i = \begin{Bmatrix} \vec{f}^e \\ \vec{m}^e \end{Bmatrix}_i - \begin{Bmatrix} 0 \\ \vec{\omega} \vec{I} \vec{\omega} \end{Bmatrix}_i + \begin{Bmatrix} \vec{f}^z \\ \vec{m}^z \end{Bmatrix}_i \quad \text{Equation 3.26}$$

Where

$$\begin{bmatrix} m\vec{E} & \vec{0} \\ \vec{0} & \vec{I}_i \end{bmatrix} = \vec{T}_i \text{ Mass matrix} \quad \text{Equation 3.27}$$

$$\begin{Bmatrix} \vec{v} \\ \vec{m}^e \end{Bmatrix}_i = \vec{r}_i \text{ Acceleration vector} \quad \text{Equation 3.28}$$

$$\begin{Bmatrix} \vec{f}^e \\ \vec{m}^e \end{Bmatrix}_i - \begin{Bmatrix} 0 \\ \vec{\omega} \vec{I} \vec{\omega} \end{Bmatrix}_i = \vec{e}_i \text{ Vector of external forces} \quad \text{Equation 3.29}$$

$$\begin{Bmatrix} \vec{f}^z \\ \vec{m}^z \end{Bmatrix}_i = \vec{z}_i \text{ Vector of reaction forces} \quad \text{Equation 3.30}$$

So, in a shorter form

$$\vec{T}_i \vec{r}_i = \vec{e}_i + \vec{z}_i \quad \text{Equation 3.31}$$

Each body of the system is described by the Equation 3.31, in order to describe the behaviour of whole bodies together the follow mathematical system must solve

$$\begin{bmatrix} \vec{T}_1 & 0 & \dots & 0 \\ 0 & \vec{T}_2 & & \vdots \\ \vdots & & \ddots & 0 \\ 0 & \dots & 0 & \vec{T}_n \end{bmatrix} \begin{pmatrix} \vec{r}_1 \\ \vec{r}_2 \\ \vdots \\ \vec{r}_n \end{pmatrix} = \begin{pmatrix} \vec{e}_1 \\ \vec{e}_2 \\ \vdots \\ \vec{e}_n \end{pmatrix} + \begin{pmatrix} \vec{z}_1 \\ \vec{z}_2 \\ \vdots \\ \vec{z}_n \end{pmatrix} \quad \text{Equation 3.32}$$

Equation 3.32 is the equations of motion of the whole system. Each body has 6 equation that describe it, so the dimension of the ODE system is very big and makes very hard solve it on the paper but the implementation on the computer is not so hard.

By the definition of the constrain holonomic equation and its derivate (Equation 3.33, Equation 3.34, Equation 3.35) it is possible write the vector of the reaction forces (\vec{z}) as in Equation 3.36.

$$\vec{g}_{(\vec{r},t)} = 0 \quad \text{Equation 3.33}$$

$$\vec{g}_{(\vec{r},t)} = \vec{G}_{(\vec{r},t)} \vec{r} + \vec{\gamma}_{(\vec{r},t)} = 0 \quad \text{Equation 3.34}$$

$$\vec{g}_{(\vec{r},t)} = \vec{G}_{(\vec{r},t)} \vec{r} + \vec{\gamma}_{(\vec{r},t)} = 0 \quad \text{Equation 3.35}$$

$$\vec{z} = \vec{G}_{(\vec{r},t)}^T \lambda \quad \text{Equation 3.36}$$

$\vec{G}_{(\vec{r},t)}$ is the Jacobian matrix of the constraint

$\vec{\gamma}_{(\vec{r},t)}$ is the time partial derivate of the constraint's vector

λ is the Lagrange multiplier to scale the constraint forces

At the end the Lagrange of 1st kind could be writing as in Equation 3.37

$$\vec{T} \vec{r} = \vec{e} + \vec{G}^T \vec{\lambda} \quad \text{Equation 3.37}$$

Hence the equation of motion in the differential algebraic from (DAE) is

$$\begin{bmatrix} \vec{T} & -\vec{G}^T \\ -\vec{G} & \vec{0} \end{bmatrix} \begin{pmatrix} \vec{r} \\ \vec{\lambda} \end{pmatrix} = \begin{pmatrix} \vec{e} \\ \vec{\gamma} \end{pmatrix} \quad \text{Equation 3.38}$$

3.2.4 Eigen behaviour

In order to study the eigen behaviour of the system the external forces are neglected, it means that the equation of motion is

$$\vec{M} \ddot{\vec{x}} + \vec{P} \dot{\vec{x}} + \vec{Q} \vec{x} = 0 \quad \text{Equation 3.39}$$

\vec{M} is the mass matrix

\vec{P} is the matrix of the velocity dependent forces

\vec{Q} is the matrix of the position dependent forces

\vec{x} is the position vector and $\dot{\vec{x}}$ and $\ddot{\vec{x}}$ are its time derivatives

The general approach to solve Equation 3.39 is impose an exponential solution like

$$\vec{x}_{(t)} = \vec{\tilde{x}} e^{\lambda t} \quad \text{Equation 3.40}$$

$$\dot{\vec{x}}_{(t)} = \lambda \vec{\tilde{x}} e^{\lambda t} \quad \text{Equation 3.41}$$

$$\ddot{\vec{x}}_{(t)} = \lambda^2 \vec{\tilde{x}} e^{\lambda t} \quad \text{Equation 3.42}$$

Where λ are the eigen values of the system. And $\vec{\tilde{x}}$ is a constant value. By making the substitution in the Equation 3.39 the equation of motion became

$$\vec{M} \lambda^2 \vec{\tilde{x}} e^{\lambda t} + \vec{P} \lambda \vec{\tilde{x}} e^{\lambda t} + \vec{Q} \vec{\tilde{x}} e^{\lambda t} = 0 \quad \text{Equation 3.43}$$

By making the simplification the finale equation to study the eigen behaviour is

$$[\vec{M} \lambda^2 + \vec{P} \lambda + \vec{Q}] \vec{\tilde{x}} = 0 \quad \text{Equation 3.44}$$

To find the λ value associated at the system has to be solved the characteristic polynomial ($p_{(\lambda)}$) in Equation 3.45

$$p_{(\lambda)} = \frac{1}{\det(\vec{M})} \det(\vec{M} \lambda^2 + \vec{P} \lambda + \vec{Q}) = 0 \quad \text{Equation 3.45}$$

The solutions of Equation 3.45 are imaginary solution, it means that each solution has its conjugate, so the solutions are like

$$\lambda_k = Re + i Im = -\delta_k + i \omega_k \quad \text{Equation 3.46}$$

$$\bar{\lambda}_k = Re - i Im = -\delta_k - i \omega_k \quad \text{Equation 3.47}$$

The system behaviour can be studied by the damping of the eigen mode (δ_k), there are three possible cases:

1. $\delta_k < 0$ the system is INSTABLE
2. $\delta_k = 0$ the system is CRITICAL STABLE
3. $\delta_k > 0$ the system is STABLE (all $-\delta_k$ must be positive, for every eigenmode)

Once evaluated the behaviour of the system is possible to find the eigenvector that describes the motion of the system in case of no external excitation, as

$$[\vec{M} \lambda_k^2 + \vec{P} \lambda_k + \vec{Q}] \vec{\tilde{x}}_k = 0 \quad \text{Equation 3.48}$$

In Equation 3.48 the value of λ_k is known and the vector $\vec{\tilde{x}}_k$ has to be assessed.

3.2.5 SIMPACK flexible body

In SIMPACK there are three possible way to model flexible bodies [29]:

- SIMBEAM with Euler-Bernoulli theory:
- SIMBEAM with Timoshenko theory:
- FlexModal

Both SIMBEAM model use a flexible beam element between the two nodes and with six degrees of freedom per node. The difference between these two ways is that SIMBEAM with Euler-Bernoulli theory doesn't include shear effect shear effects and, therefore, under predicts deflections and over predicts eigenfrequencies. the 'Euler-Bernoulli' type is suggested in cases where $l / d > 10$, where l is the overall length of a beam and d is a typical cross section diameter, on the contrary, SIMBEAM with Timoshenko theory is an advance beam theory and includes the effects of transverse shear strain in the beam, as well as the effects of rotational inertia, The 'Timoshenko' type is suggested in cases where $10 > l / d > 5$, where l is the overall length of a beam and d is a typical cross section diameter [29]. The bodies that can be modelled by SIMBEAM elements normally have a simple geometry and they are define directly in SIMPACK. The FlexModal need to a *.fbi file that contains the finite element model (the finite element model is made with other software as AAQUS, IPERMESH, SOLIDWORKS, ...) with the geometry and the material property, so this kind of model is better when the flexible body that want to be analyse has a complex geometry and if it is an assembly of more components.

3.3 Modal assurance criterion

The modal assurance criterion is a statistical indicator to compare the mode shapes come from two different simulations, is often used to compare the results come from an experimental simulation and the results come from an analytical simulation but, it can be also used to compare the mode shape from two analytical simulations. In this work it is used to compare the mode shape come from ABAQUS and the mode shapes come from SIMPACK, in order to define the right number of nodes to export from ABAQUS to SIMPACK. The basic idea of this theory is to compare mode vectors of all eigenmodes in order to check their orthogonality and give this information as an output number in the range between 0 to 1. It means that if two mode shapes are similar, the *MAC* must be equal to 1 (the modal vectors are not orthogonal) and on the other hand if two mode shapes are different the *MAC* must be equal to 0 (the modal vectors are orthogonal). In order to have a good relationship between two models the *MAC* matrix should have along the main diagonal only value close to 1 and outside it there should be only values close to 0. By the definition of shape vectors ($\{\psi_A\}_i$) as

$$\{\psi_A\}_i = \begin{Bmatrix} x_1 \\ y_1 \\ z_1 \\ \vdots \\ x_n \\ y_n \\ z_n \end{Bmatrix}_i \quad \text{Equation 3.49}$$

the *MAC* matrix is defined as follow [30] [31].

$$MAC(i, k) = \frac{|\{\psi_A\}_i^T \{\psi_B\}_k|^2}{\{\psi_A\}_i^T \{\psi_A\}_i \{\psi_B\}_k^T \{\psi_B\}_k} \quad \text{Equation 3.50}$$

The implementation of the Equation 3.50 can be done with a MATLAB script and its visualization is usually like a bar diagram, as in Figure 3.5, or like a colour 2d graph.

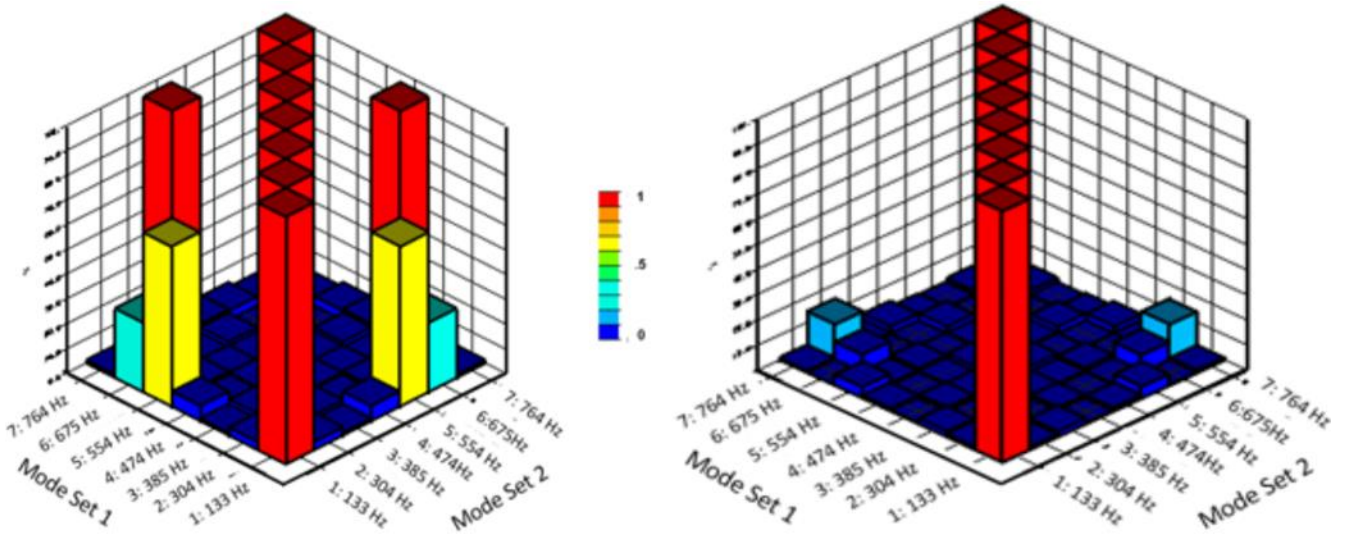


Figure 3.5: Bad example of *MAC* matrix (left), good example of *MAC* matrix (right) [32]

In Figure 3.5 it can be seen a bad output of *MAC* matrix, along the main diagonal there are only 1 but there are values equal to 1 also outside the main diagonal, it means that the mode shape 7th and 3rd have the seam behaviour and they can't be separated. On the other hand, the other *MAC* matrix is an example of good output, there are 1 only along the main diagonal, it means that the behaviour of all mode shapes can be distinguished.

4. Structure of the models for the simulations

The first section of this chapter describes the macro-geometry and the material property of the wind turbine used to make the simulations, it also defines how the components are in touch, the dimension of each component and the position of the bearings. The second section illustrates the bearing's mechanical properties and how they have been modelled in ABAQUS. In the third section is explained the convergence analysis, for the static and the modal simulations: the property of each FEM model is illustrated. In order to compare the SIMPACK and ABAQUS eigenmode, after the convergence analysis, the MAC matrix have been used. At the end of the chapter the whole FEM and MBS models of generator are described.

4.1 Geometrical and mechanical characteristics

Figure 4.1 shows the entire model of the wind turbine: the rotor diameter is equal to 130 m, the tower is 112 m high and its weight is 517.8 ton and between the ground and the generator's axis there is an angle (β) equal to 5° . This angle makes more distance between the tower and the blades, it is necessary because during the operation the blades deflect towards the tower and they could touch it. The whole system is fixed on the ground by the foundation, its mass is 420.8 ton.

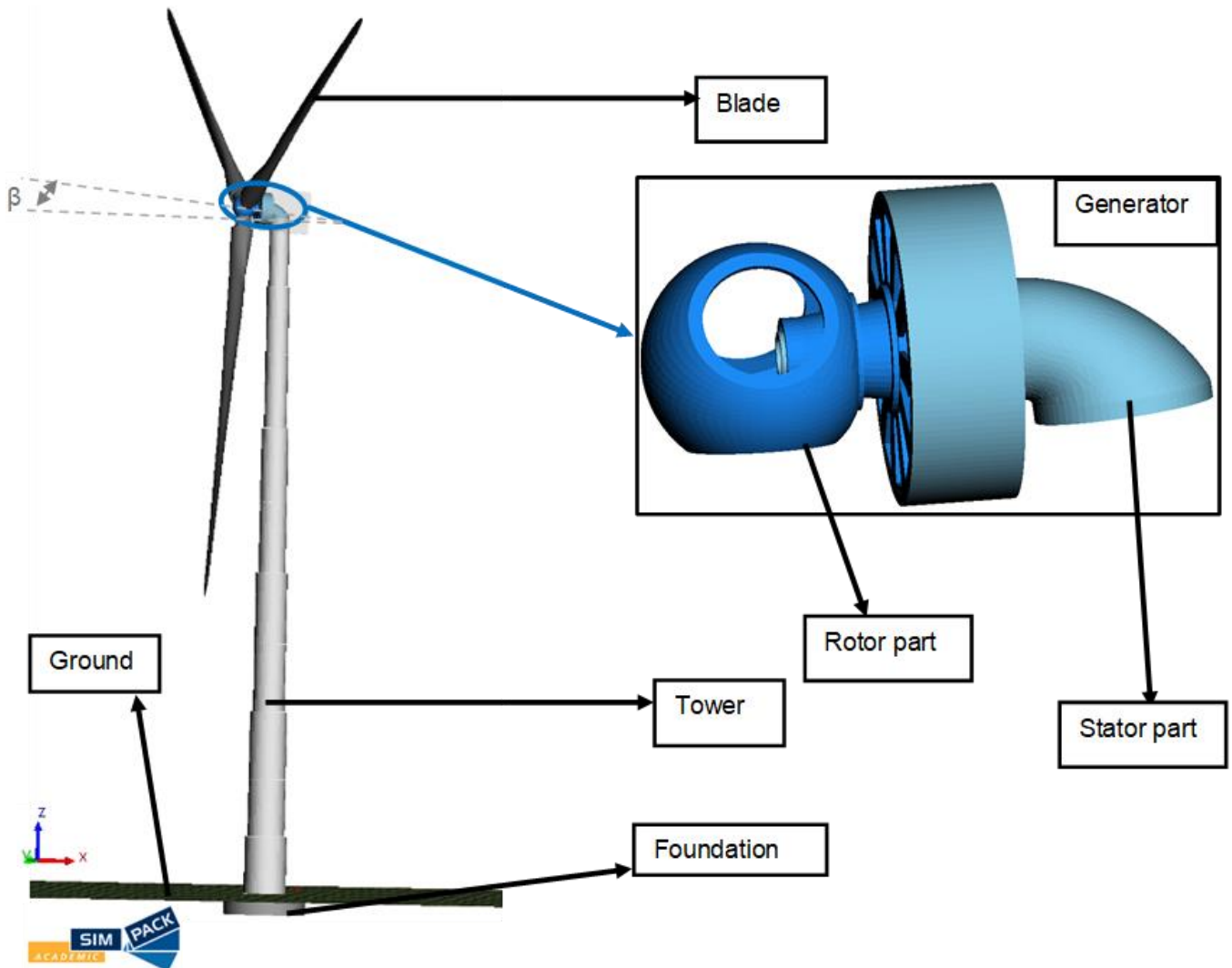


Figure 4.1: Wind turbine: model in SIMPACK

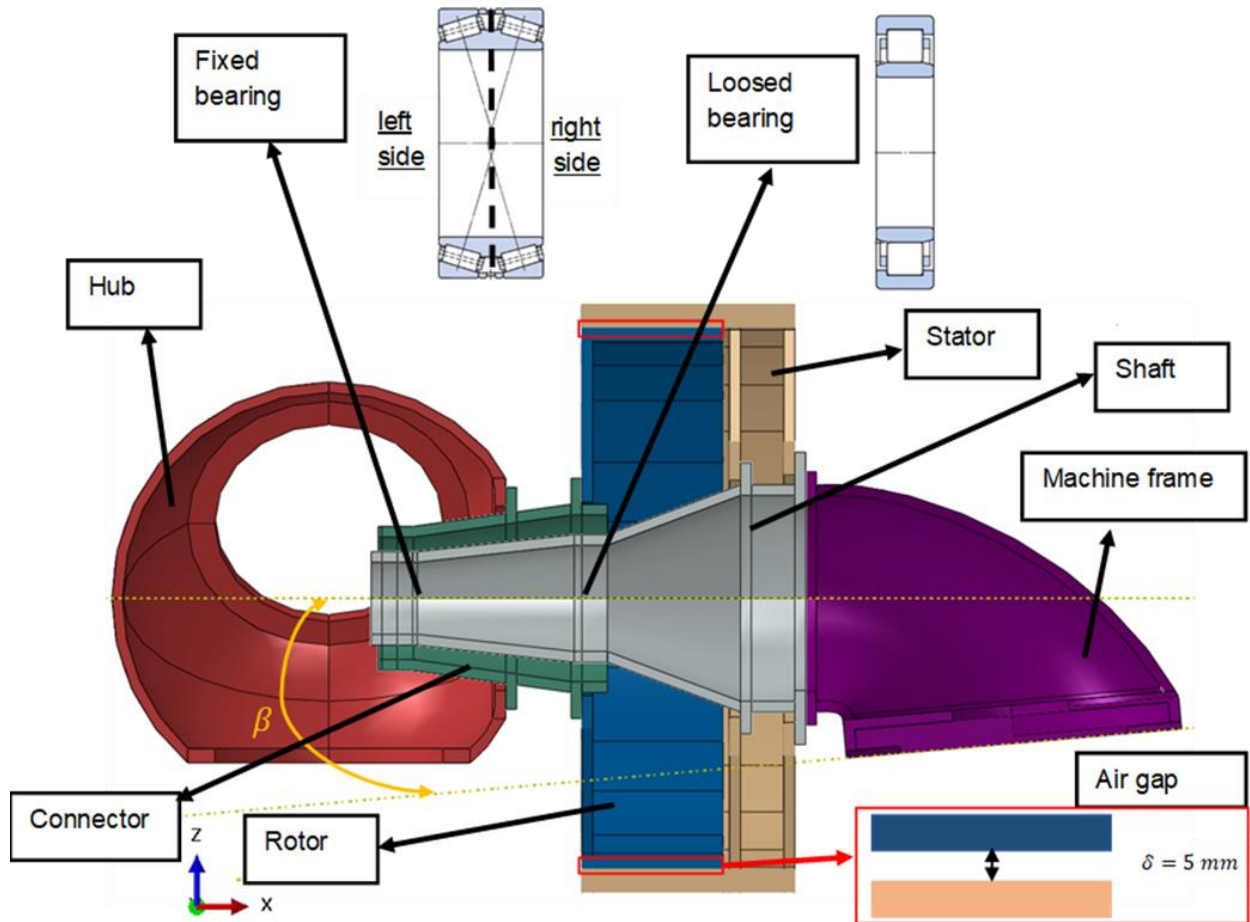


Figure 4.2: Cross section of Generator

Figure 4.2 shows the cross-section of the generator which is an inner rotor generator with 80 poles. The stator inner diameter is 5 m and the rotor out diameter is 4.995 m, hence the air gap clearance is equal to 5 mm. The rotor length is 1300 mm, so the airgap length is also 1300 mm. The machine frame is in touch with the tower and with one side of the shaft. There are 2 contact points between the stator and the shaft in order to make a very strong constraint and restrain its movement. The angular rotation of the rotor is allowed by the bearings that are attached to the shaft and to the connector. In this system there are two bearings, one Loosed bearing and one Fixed bearing, their position and their section it is showed in Figure 4.2. The bearing's characteristics are described in the next section. The rotor and the hub are connected to each other by the connector, both are only one surface in touch with the connector. The hub has three holes that are in connected with the adaptors of the blades, that means that the forces due to the weight of the blades act on the surface of these three holes. Another important thing is the distance between the bearings and the region where the active forces act, they don't act between the two bearings, so the moment due to the blades will have a very big impact on the structure. The material that was used for the whole system is the steel, its mechanical properties are showed in Table 4.1

E	210000 $\text{tonn}/(\text{mm s}^2)$
ρ	$7,85 \cdot 10^{-9} \text{ tonn}/\text{mm}^3$
ν	0,3

Table 4.1: Steel mechanical properties

4.2 Bearings

The geometrical characteristics of the Fixed bearing are showed in Table 4.2 and in Table 4.3 are showed the geometrical characteristics of the Loosed bearing.

d	863,6 mm
D	1130,3 mm
T	323,85 mm
B	323,85 mm
$r_{1,2min}$	4,8 mm
$r_{3,4min}$	12,7 mm
d_1	918 mm
D_1	1029 mm

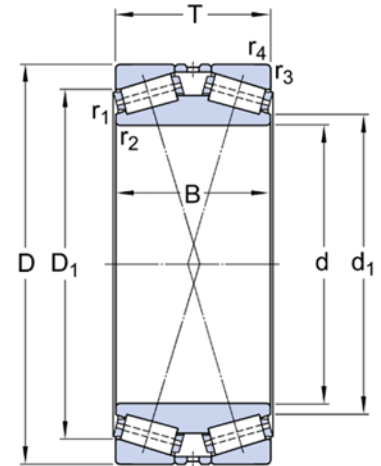


Table 4.2: Geometrical characteristic of Fixed bearing [33]

d	1180 mm
D	1540 mm
B	206 mm
D_1	1434 mm
F	1258 mm
$r_{1,2min}$	7,5 mm

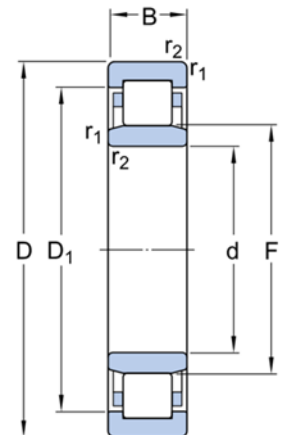


Table 4.3: Geometrical characteristic of Loosed bearing [34]

The stiffness of Fixed bearing and Loosed bearing come from another work made in the C.W.D. institute of R.W.T.H. Aachen. Table 4.2 shows that the Fixed bearing is made by two rollers hence, in order to make more realistic model, its radial stiffness has been split using the law of the parallel equivalent spring and its axial bearing is split between left side and right side: if a positive force act on the bearing then its right side will be charge and if a negative force act on the bearing then its left side will be charge (this is true for the reference system and the bearing in Figure 4.2). The Loosed bearing has only one roller, it means that the data could be used as they are. In Figure 4.3 is showed the radial stiffness of Fixed bearing, with only one roller works and with both two rollers work, and the radial stiffness of Loosed bearing. Figure 4.4 shows the axial stiffness of the Fixed bearing, the axial stiffness of the Loosed bearing is not mentioned because this bearing is not designed to withstand the axial loads.

The Loosed bearing radial stiffness is softer than the radial stiffness of the Fixed bearing and it is also not designed to withstand the axial loads, for these reasons the Fixed bearing is close to the hub, in order to withstand the external loads, and the Loosed bearing is close to the rotor, where the loads are lower

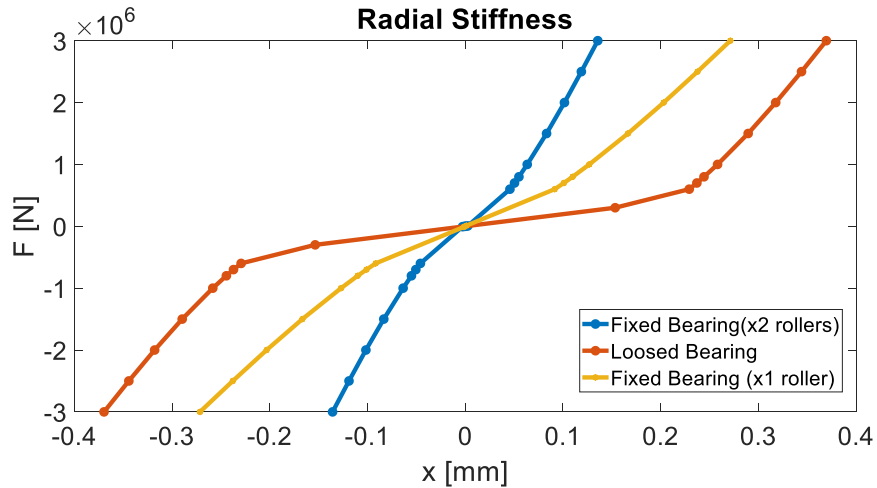


Figure 4.3: Radial stiffness of Fixed and Loosed bearings

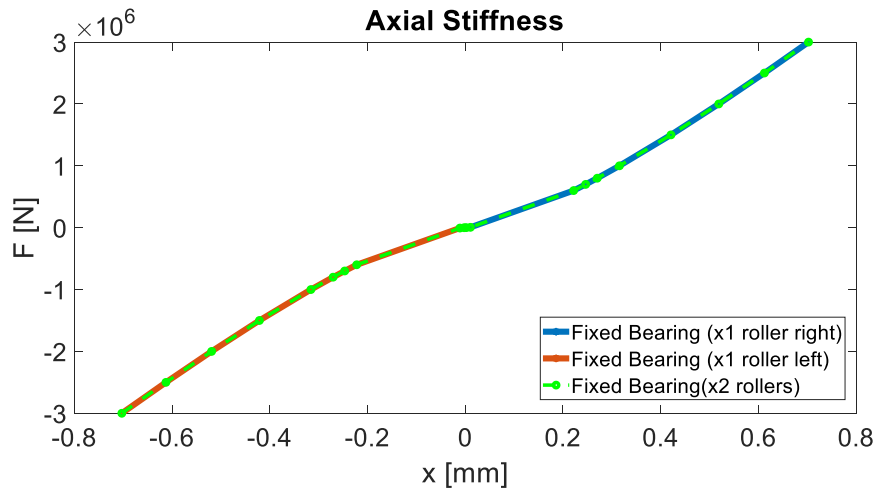


Figure 4.4: Axial stiffness of Fixed bearing

For the first step three different model of bearing has been implemented. The measures of Fixed bearing are shown in Table 4.2, the measure relative to the Loosed bearing are shown in Table 4.3. The first model was considering the all surface of rollers for both bearing, $B/2$ and B . In the second model, the reference length for the rollers is $B/6$ and $B/3$. In the third concept each roller has been modelled like only one line along the surface in the middle of each bearing's roller. Figure 4.5 and Figure 4.6 show the sketches of the three different model for the Fixed and Loosed bearing respectively.

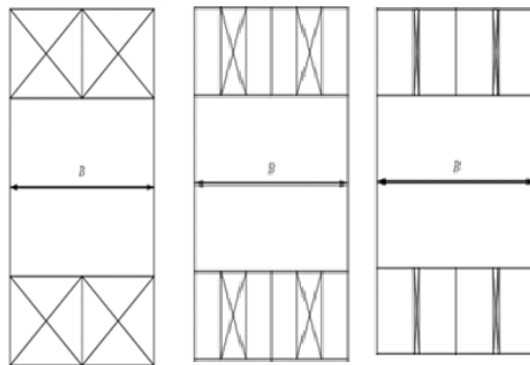


Figure 4.5 Fixed bearing different configurations

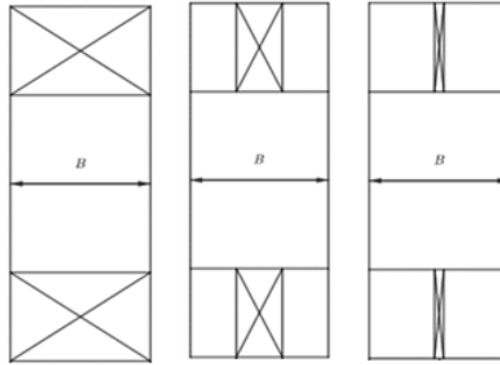


Figure 4.6: Loosed bearing different configurations

The FEM model of the first two concept of bearings in ABAQUS has been modelled with two reference points joint by a wire with specific reference length. The properties of the bearings are defined in a radial thrust connector element which is applied on the wire. This connector element has been chosen because it allows to define the properties along x and z axes. One reference point is attached with the external surface of the connector with a coupling constraint type continuum distribution, the other reference point is attached with the internal surface of the shaft by the same constraint. This kind of constraint has been chosen because they allow the movement of the surfaces. Due to the geometrical property of a line for to make the model of the third kind of bearing the kinematic coupling has been chosen. This kind of constraint doesn't allow the deformation of the surfaces. Only the first concept was been reduced in SIMPACK. Figure 4.7 presents the ABAQUS model for one roller of the Fixed bearing. More damping has been added on the bearings to stabilize the system, paragraph 5.1.1 explains the guidelines to follow in order to stabilize the system with artificial damping

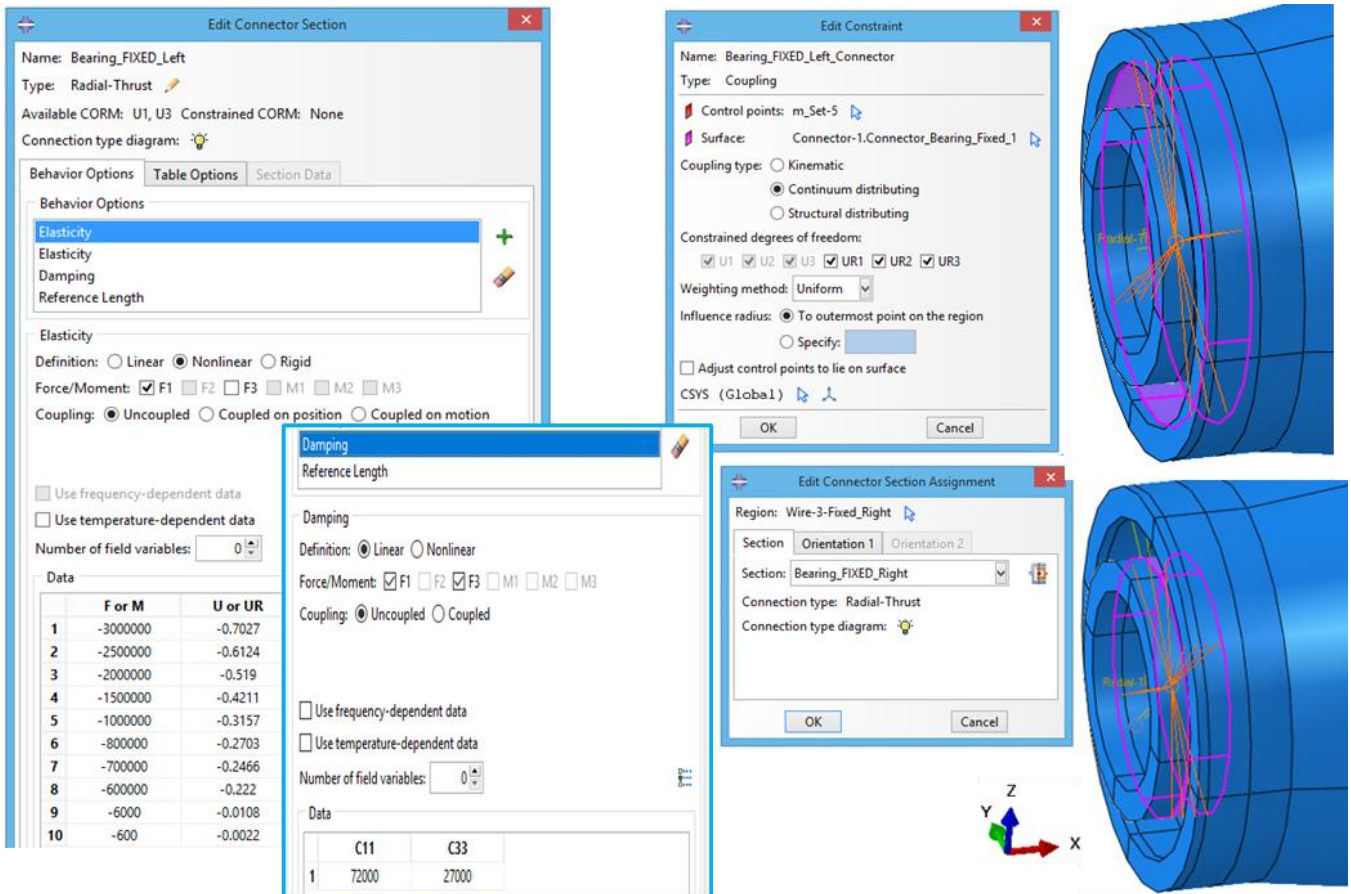


Figure 4.7: Fixed bearing F.E.M modelling in ABAQUS: first concept with artificial damping

To don't allow any change in the bearings clearance the bearings have been made with only one reference point for both surfaces, in this way it is possible analyses the impact of the rigid bearing. Figure 4.8 shows the sketch how to make a rigid bearing.

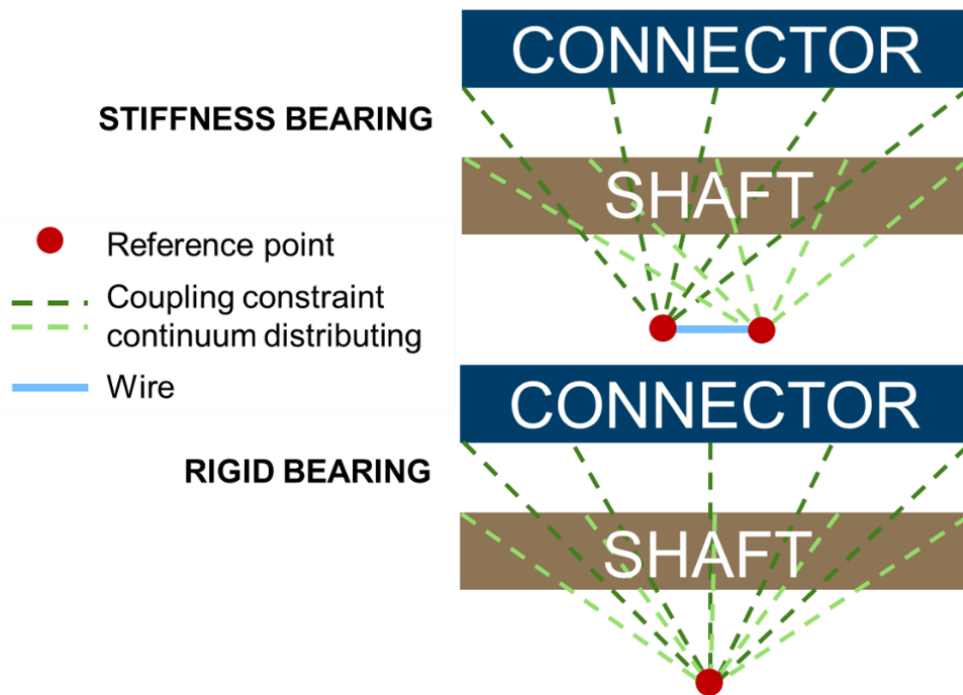


Figure 4.8: Sketch of rigid bearing

4.3 Convergence analysis

As the procedure to make the convergence analysis is the same for every component in this paragraph is describe only one case. The chosen case is the machine frame because its geometry is the most complex. The plots and the property of the mesh of the other components follow this first step.

The machine frame is constrained to the tower and with the shaft, it is the heaviest component of the generator and its geometry is very complex. In Figure 4.9 are showed the CAD model and the FEM model of the frame.

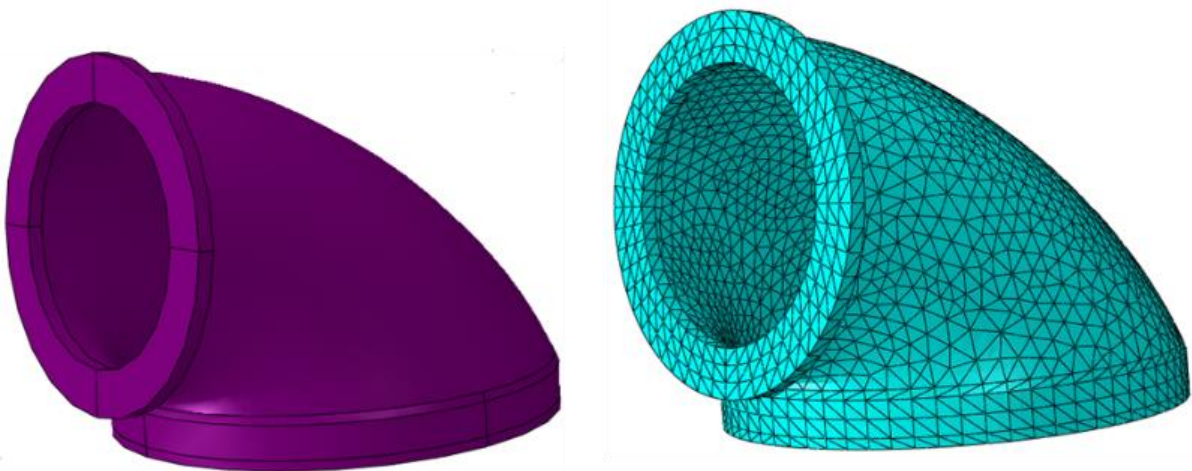


Figure 4.9: Machine frame: CAD model a) and FEM model b)

Due to the curvature of the machine frame between the constraints of the tower and the constraint of the shaft the mesh with the hexagonal elements is not allow. Figure 4.109 shows the model with hexagonal mesh and

with tetragonal mesh. The region between the curvature and the joint fails to mesh because the geometry of the component in that region distorts too much the elements.

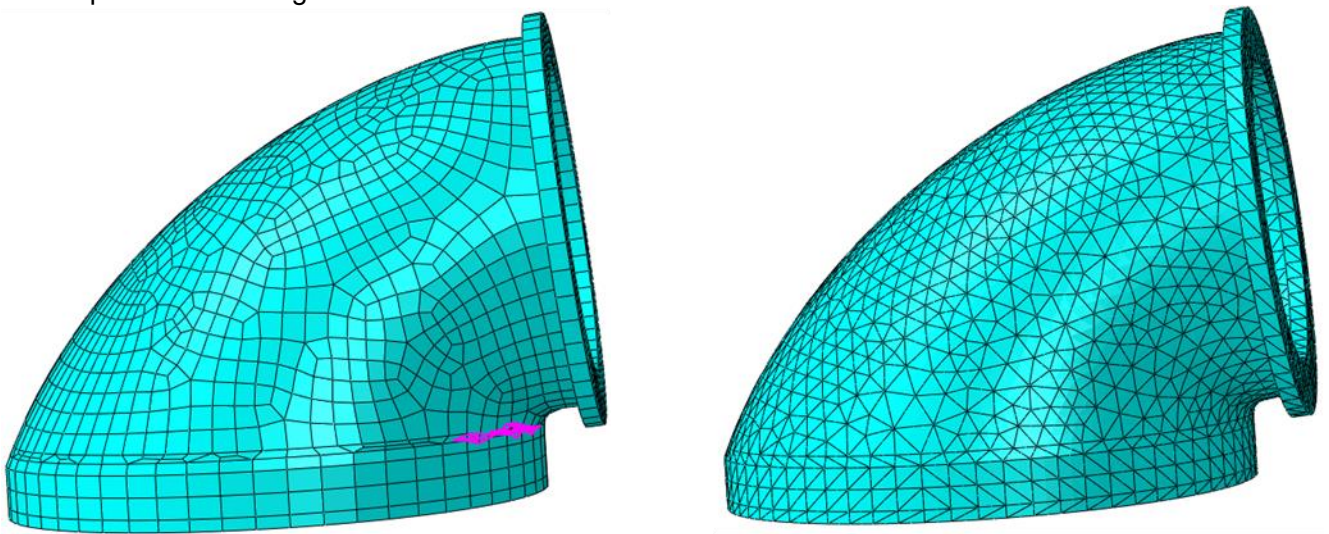


Figure 4.10: Machine frame: hexagonal and tetragonal mesh

Of course, the convergence analysis has been performed only for the tetragonal elements. For the convergence static analysis, a load equal to 1 ton in each direction has been used and applied on the surface where the frame is in touch with the shaft, and the boundary condition has been applied where the frame is attached to the tower and it is 0 dof constraint. Figure 4.11 shows the plot of the convergence analysis to the static case. As expected, the structure that has been meshed by tetragonal linear elements is stiffer than the structure that has been meshed by tetragonal quadratic elements, and the velocity of convergence is faster for the mesh made by quadratic elements.

In Figure 4.12 is showed the convergence modal analysis. Also, in this case, as expected, the tetragonal linear mesh is stiffer than the tetragonal quadratic mesh, this can be seen because the frequency of the linear mesh is always higher than the frequency of the quadratic mesh. This result confirms that the mesh convergence analysis is good. The modal convergence analysis is showed only for the first mode, but it has done for the first 30th mode. For the modal convergence analysis of every components 6 degree of freedom has been used and the rigid eigen mode has been ignored.

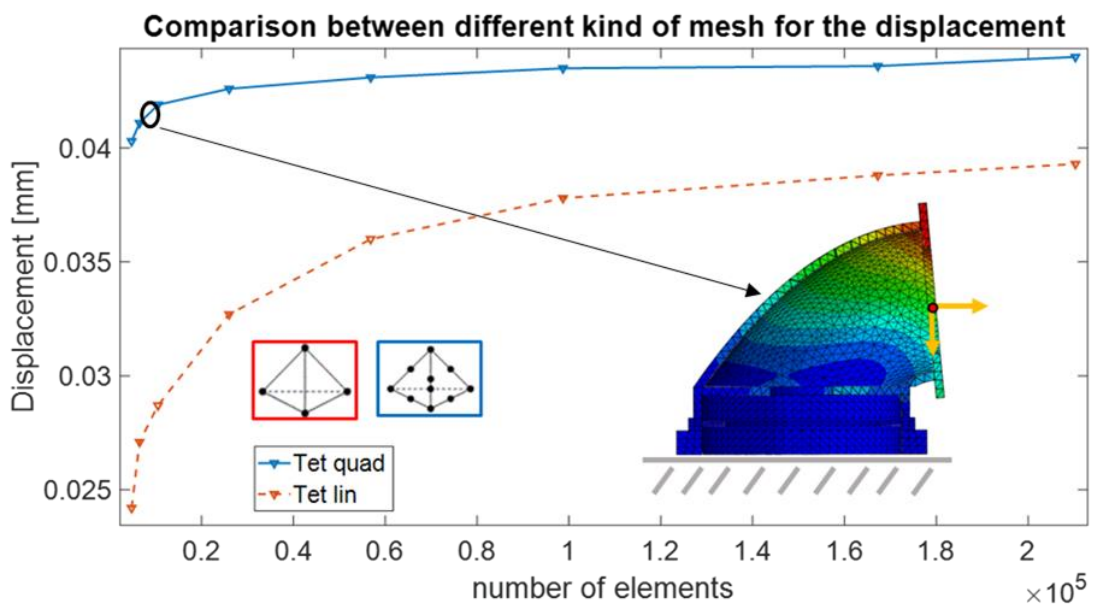


Figure 4.11: Frame: static convergence analysis

The results achieved in the convergence analysis led to make a hexagonal quadratic mesh with 16'584 elements. In Table 4.4 is showed a summary of all property of the machine frame, for the property of the material see Table 4.1.

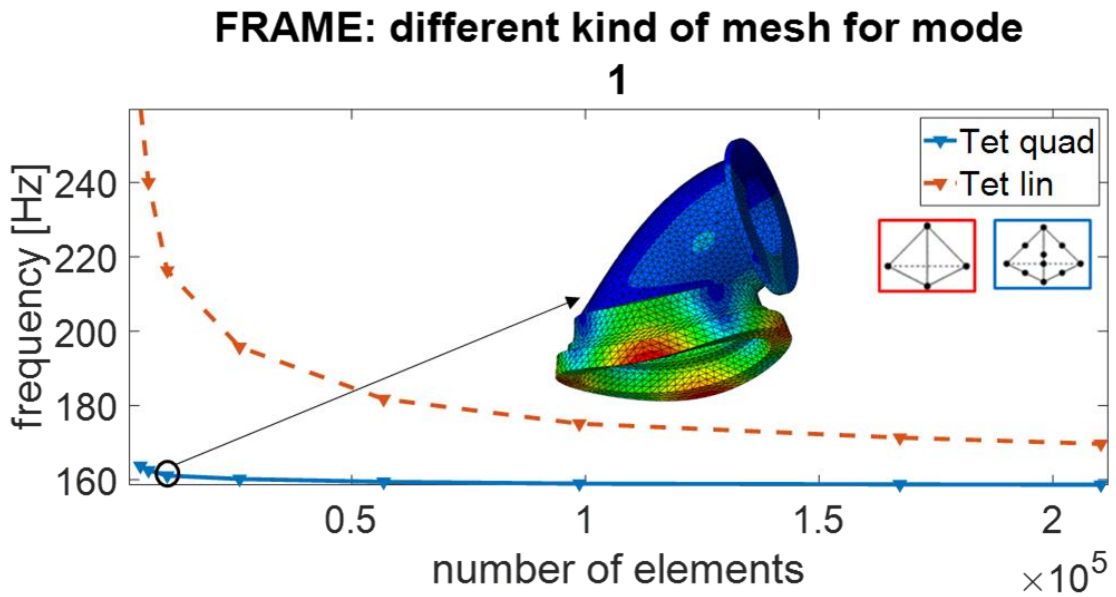


Figure 4.12: Frame: modal convergence analysis

Component	n. nodes	n. elements	Type of elements	Mass
Frame	32'346	16'834	C3D10	22.69 ton

Table 4.4: Frame: properties of the mesh

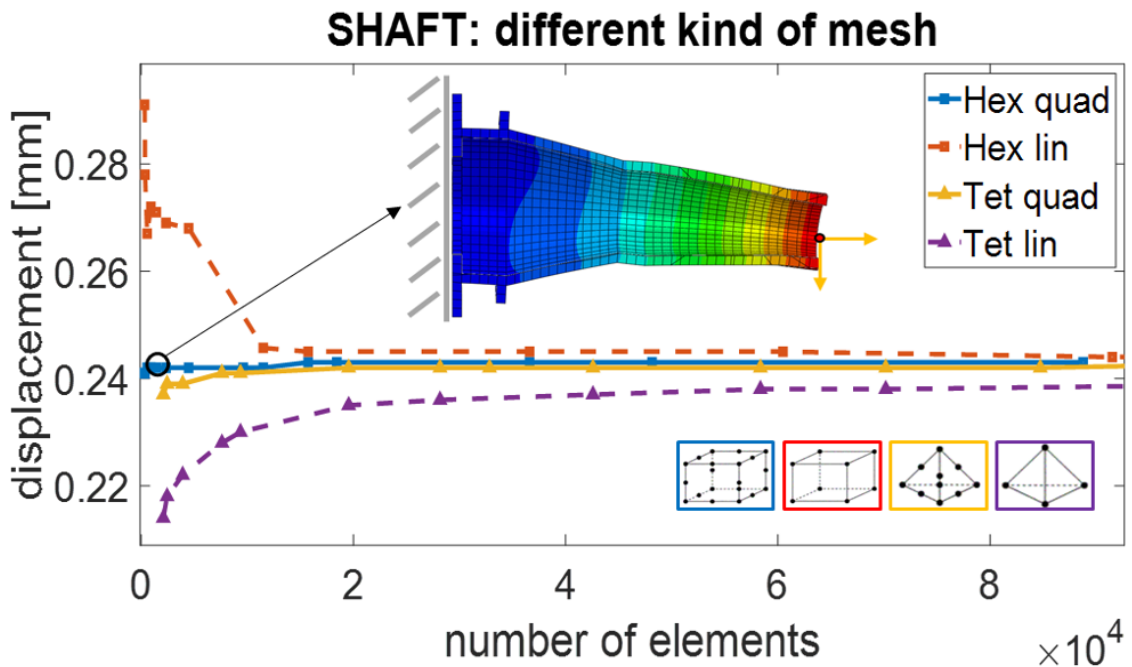


Figure 4.13 Shaft: static convergence analysis

SHAFT: different kind of mesh for mode 1

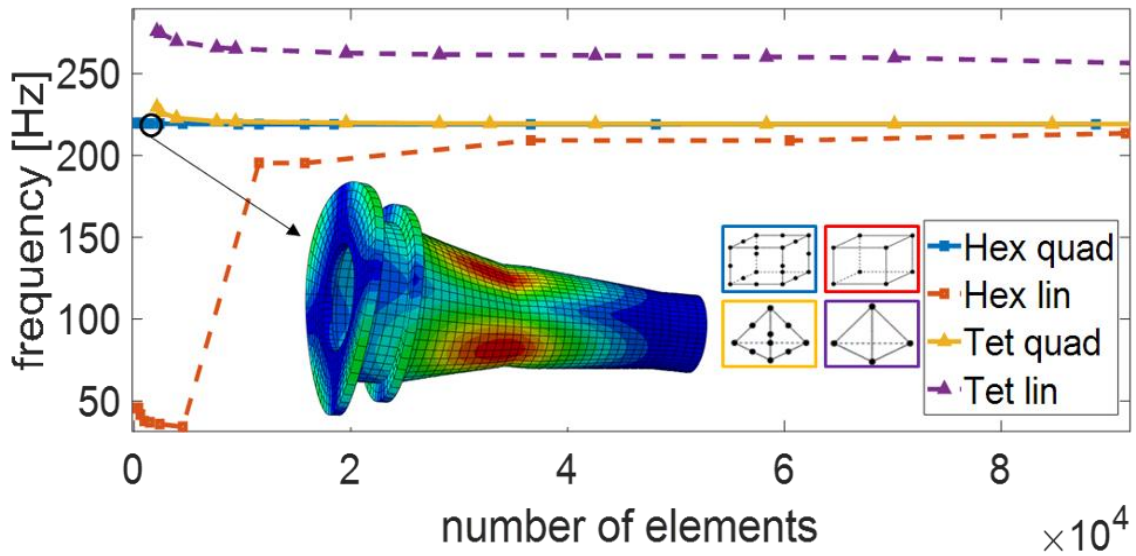


Figure 4.14: Shaft: modal convergence analysis

Component	n. nodes	n. elements	Type of elements	Mass
Shaft	11'680	1'640	C3D20R	15.86 ton

Table 4.5: Shaft: properties of the mesh

CONNECTOR: different kind of mesh

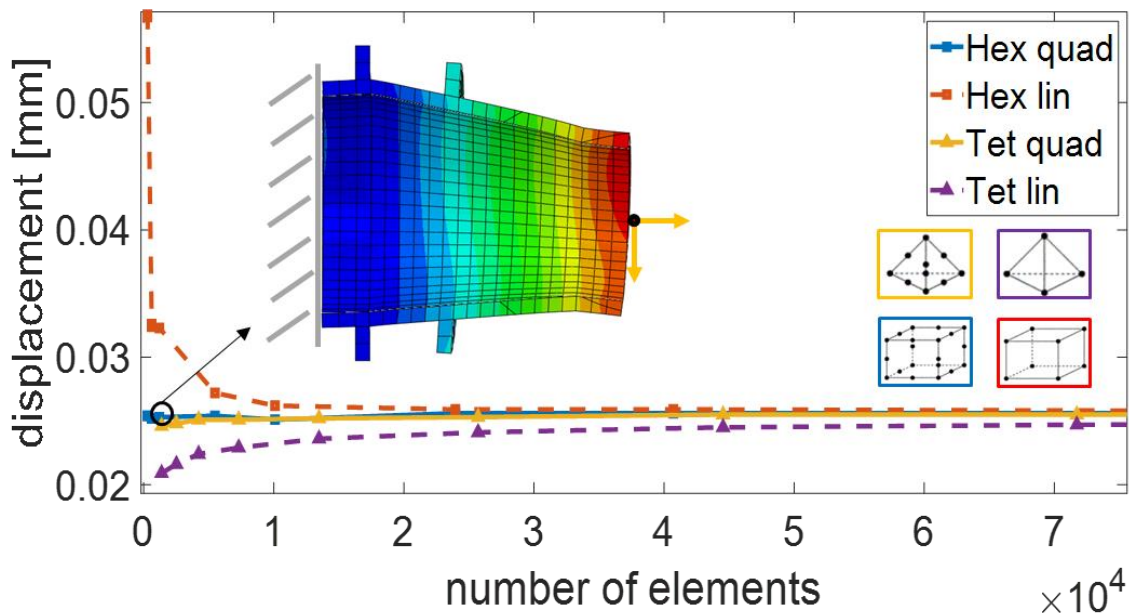


Figure 4.15: Connector: static convergence analysis

CONNECTOR: different kind of mesh for mode 1

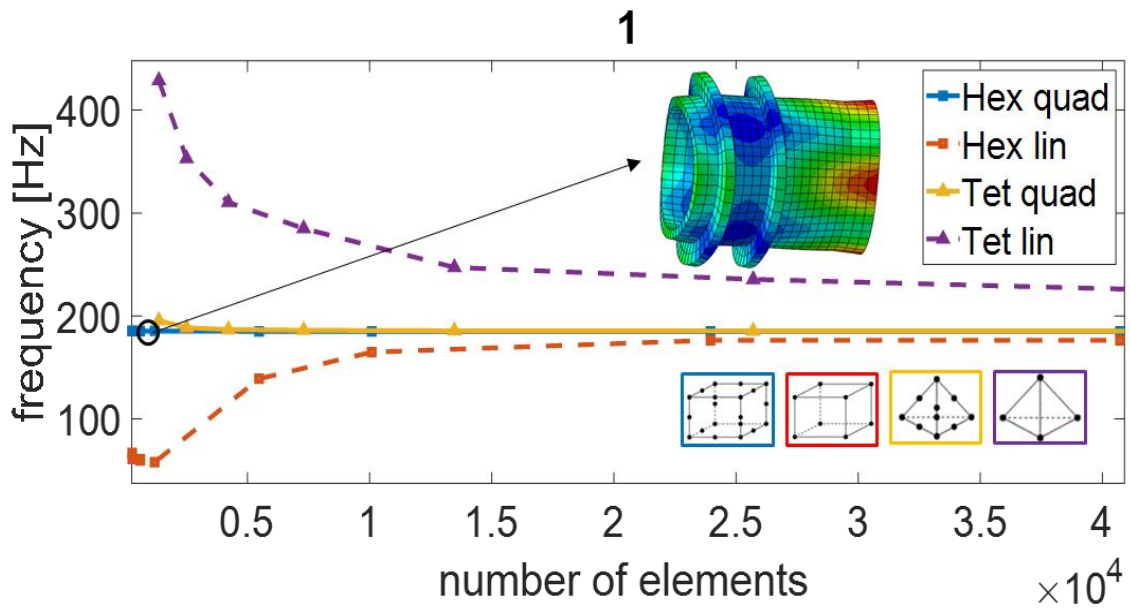


Figure: 4.16 Connector: modal convergence analysis

Component	n. nodes	n. elements	Type of elements	Mass
Connector	6'640	920	C3D20R	9.74 ton

Table 4.6: Connector: properties of the mesh

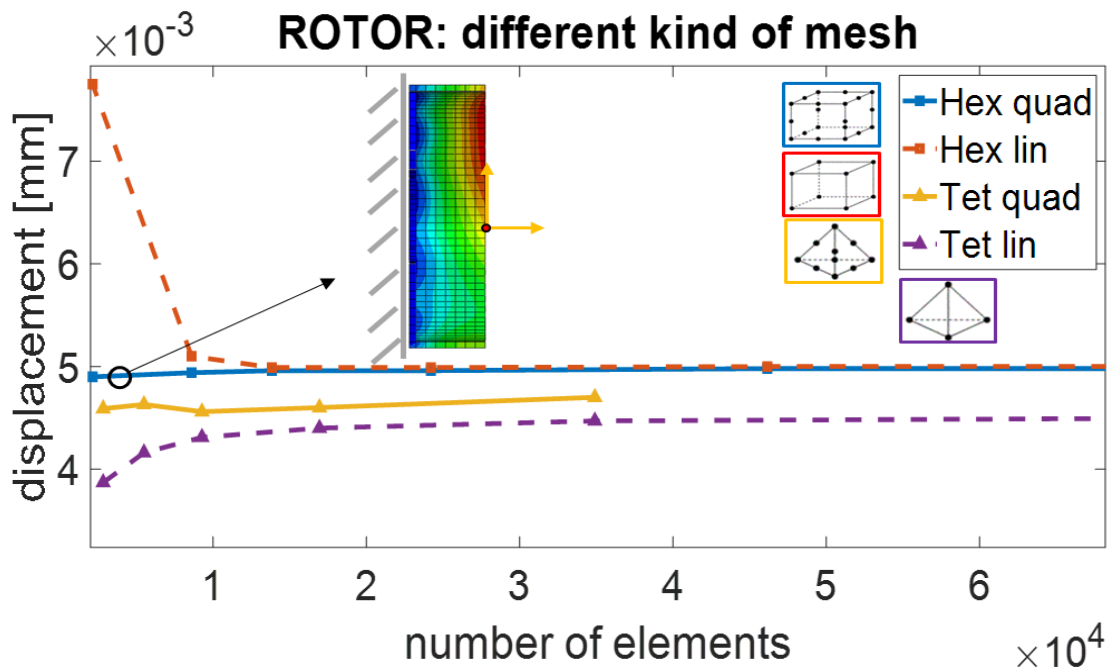


Figure 4.17: Rotor: static convergence analysis

ROTOR: different kind of mesh for mode 1

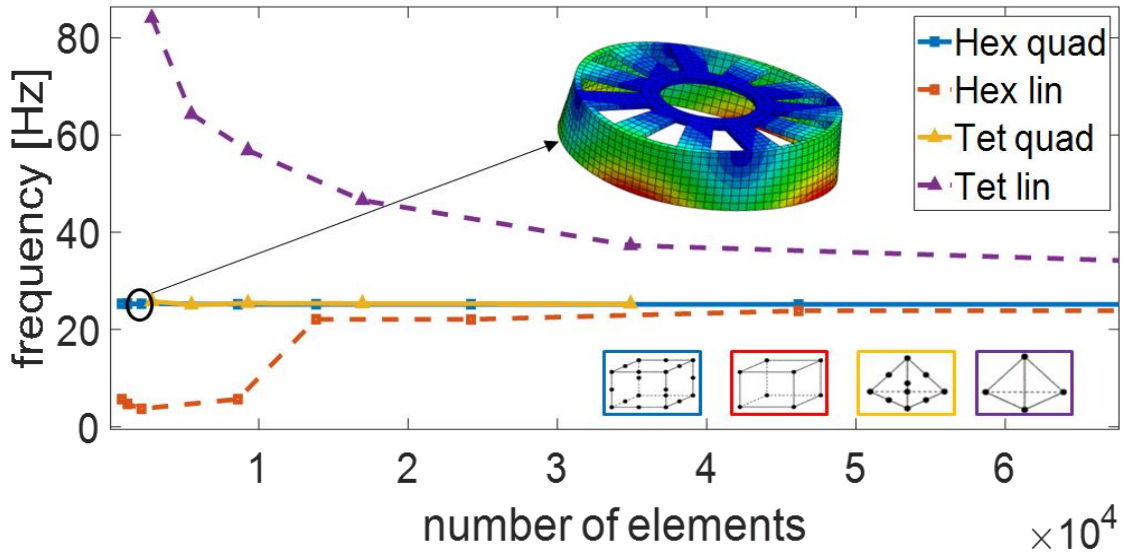


Figure 4.18: Rotor: modal convergence analysis

Component	n. nodes	n. elements	Type of elements	Mass
Rotor	16'836	2'222	C3D20R	24.90

Table 4.7: Stator: properties of the mesh

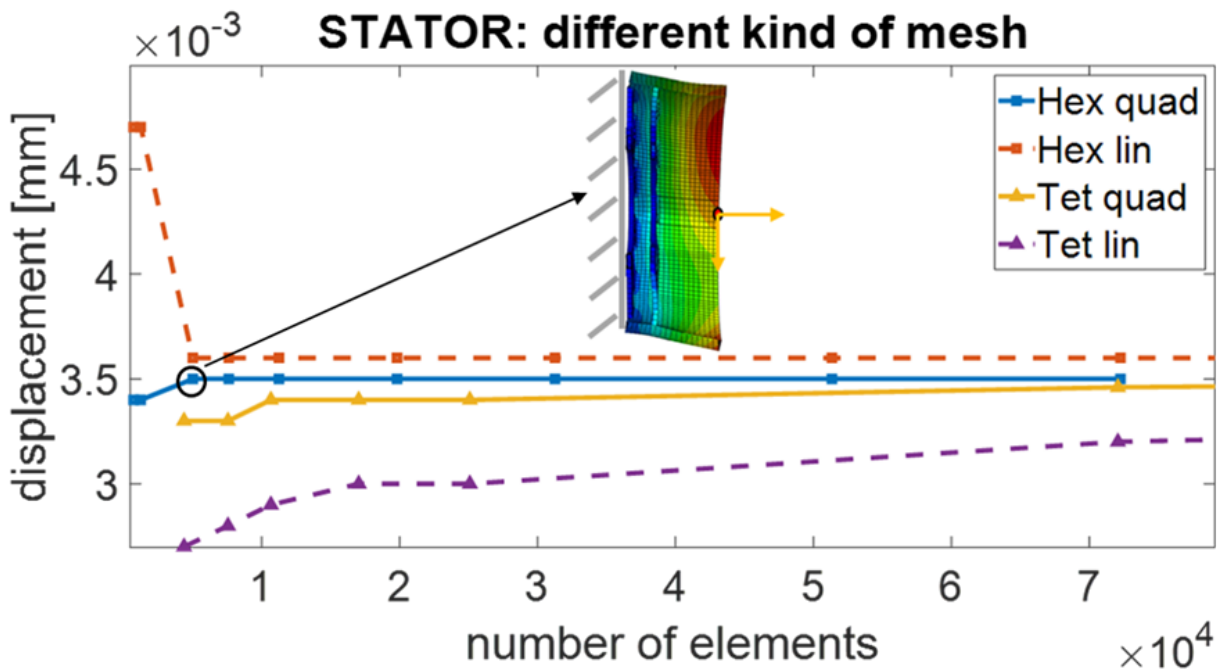


Figure 4.19: Stator: static convergence analysis

STATOR: different kind of mesh for mode 1

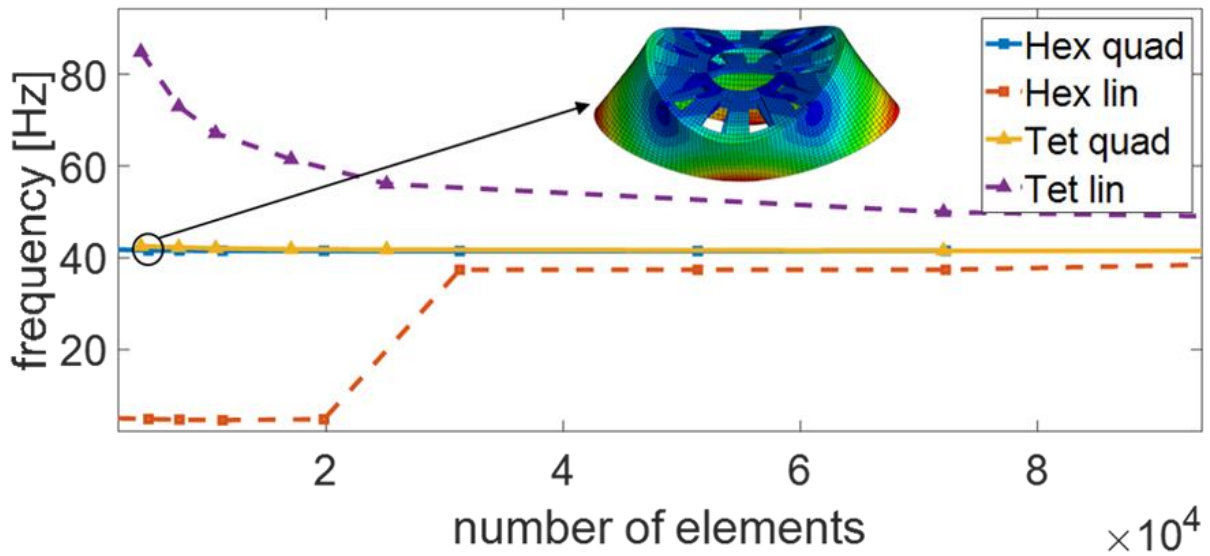


Figure 4.20: Stator: modal convergence analysis

Component	n. nodes	n. elements	Type of elements	Mass
Stator	36'912	5'864	C3D20R	70.06

Table 4.8: Rotor: properties of the mesh

Due to the high angle near to the hub's hole it is not possible to create a hexagonal mesh, for this reason the convergence analysis has done only for the tetragonal elements.

HUB: different kind of mesh

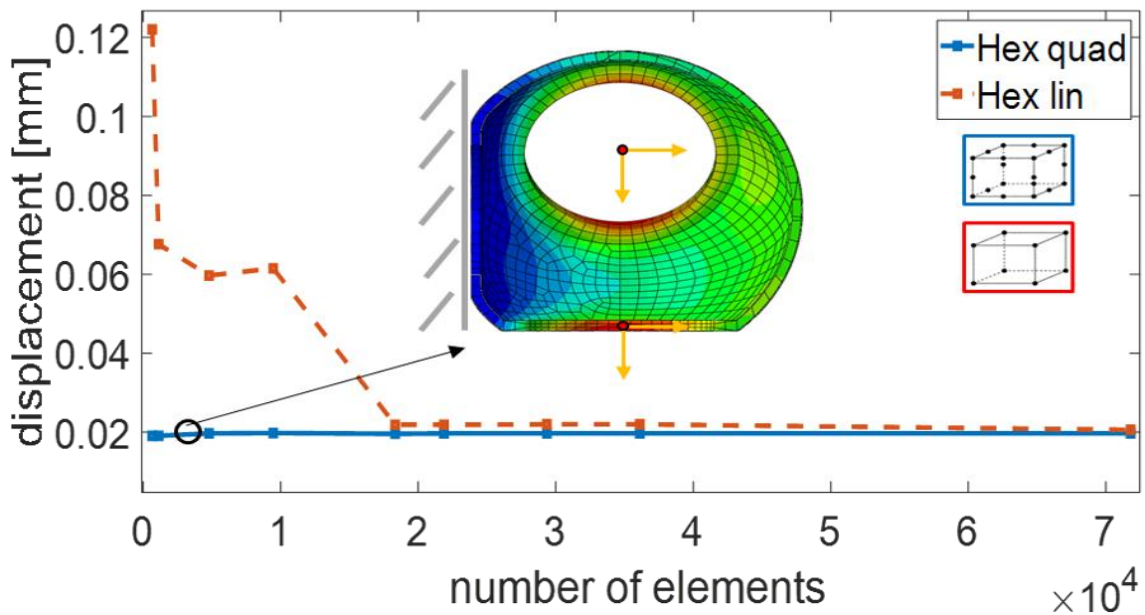


Figure 4.21: Hub: static convergence analysis

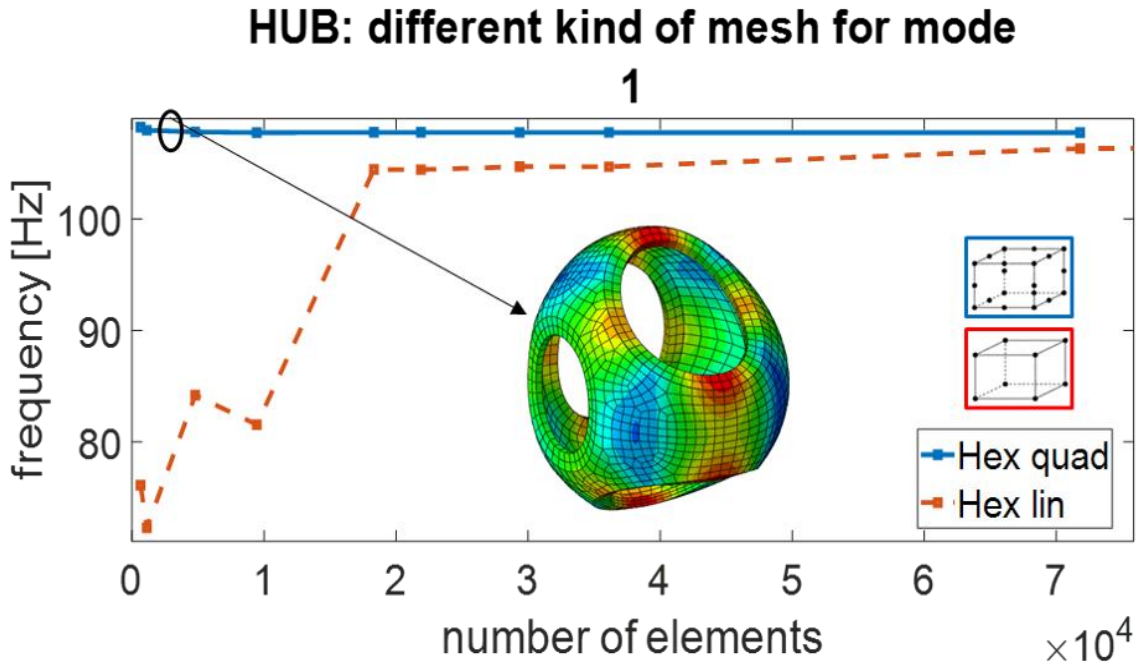


Figure 4.22: Hub: modal convergence analysis

Component	n. nodes	n. elements	Type of elements	Mass
Hub	19'096	2'803	C3D20R	26.94

Table 4.9: Hub: properties of the mesh

The convergence analysis for every component give the same trend of the results, the Hexagonal quadratic element makes a model stiffer than the other elements and the velocity of convergence with this kind of elements are faster than with the other elements. In Table 4.10 is given the summary of the properties of the mesh. In order to allow the best matching between the components that are in touch the size of the elements doesn't change and it is equal to 120.

Component	n. nodes	n. elements	Type of elements	Mass (FEM)
Frame	32'346	16'834	C3D10	22.69 ton
Shaft	11'680	1'640	C3D20R	15.86 ton
Connector	6'640	9'20	C3D20R	9.74 ton
Stator	36'912	5'864	C3D20R	70.06 ton
Rotor	16'836	2'222	C3D20R	24.90 ton
Hub	19'096	2'803	C3D20R	26.94 ton
System	123'510	30'283	C3D20R – C3D10	170.21

Table 4.10: Summary of the properties of the mesh

4.4 MAC matrix

In order to compare the direction of the mode shapes in ABAQUS and in SIMPACK the modal Mac matrix has been performed. As in previous section, the procedure to make the MAC matrix is describe only for one component, the hub, and the plot of the Mac matrix for the other components follow.

The process for to make the Mac matrix is an iterative process. The first step is to choose one set-nodes in ABAQUS: the nodes must be chosen in the position where there is the maximum absolute value of the displacement for each natural frequency. The second step is made the Auto Mac matrix, in order to see if the nodes that have been chosen are enough and in the right position to describe the eigenmodes during the FEM simulation. The third step is to make the freedom reduction in order to import the flexible body in SIMPACK, being careful to import the same node-set defined in ABAQUS. Also, the Auto Mac matrix in SIMPACK must be done, in order to see if the node-set is able to describe the mode shape during the MBS simulation. The last step is to make the comparison between the behaviour of the mode shape by the Mac matrix. If after the last step along the main diagonal of the MAC matrix there are a lot of value lower than 0.5 another iteration must be done, until the result has a sufficient degree accuracy. In Figure 4.23 is showed the different steps that had to be done to make the Mac matrix for the hub.

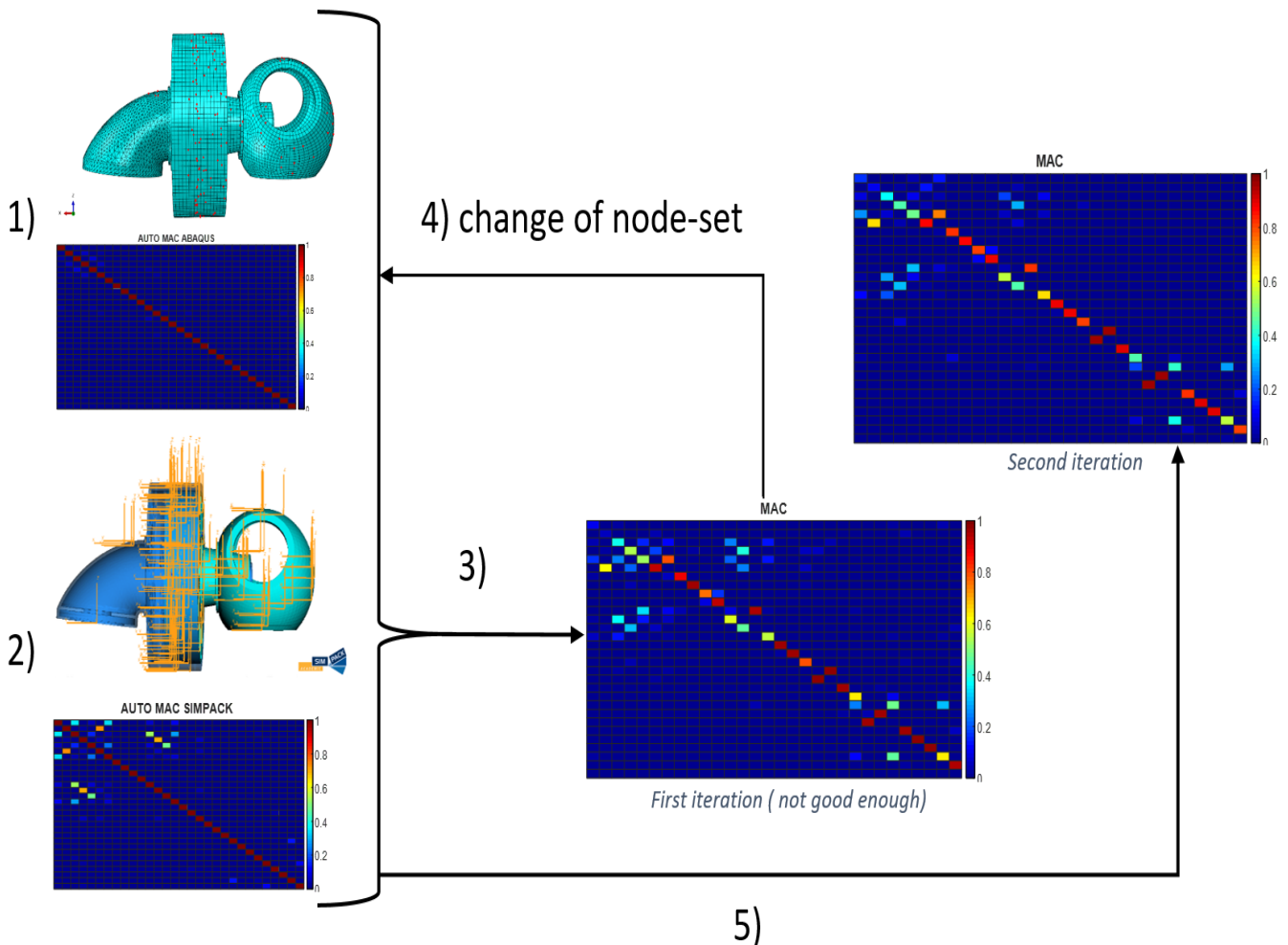


Figure 4.23: MAC matrix iterations

Figure 4.23 show that the first iteration with 52nodes gives good Auto MAC matrix but it is not able to make in correlation the mode shapes from ABAQUS and SIMPACK, in order to do it the second iteration with 120 nodes had to do. This second iteration gives a MAC matrix with a very high degree accuracy. The explanation of this MAC matrix follows.

Figure 4.30 shows the result of a comparison between MBS and FEM mode shapes considering the behaviour of 120 hub's nodes. The results show that the couples $20^{th} - 21^{th}$, $22^{th} - 23^{th}$, $24^{th} - 25^{th}$ and $27^{th} - 28^{th}$ are pair mode shapes, it means that their behaviour has reversed. Except for these cases along the main diagonal there are only value close to 1, it means that the matching between FEM and MBS are good.

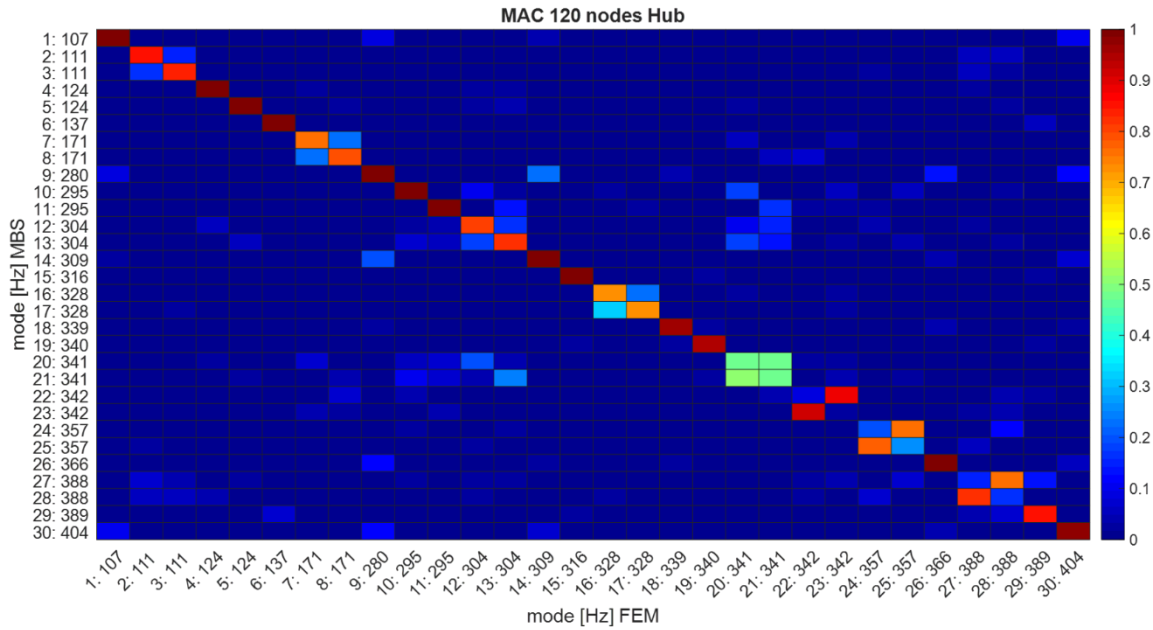


Figure 4.24: Hub: MAC matrix

For reason of understanding of the interim figures the Auto MAC matrix of the other components are in the appendix. The MAC matrix of the other components follows.

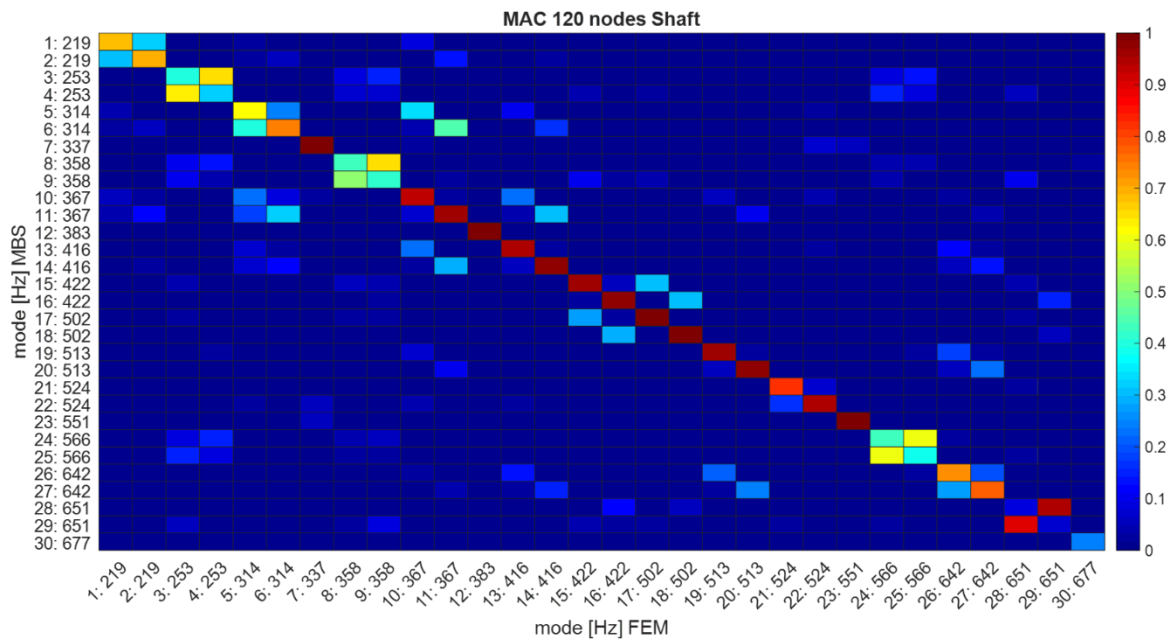


Figure 4.25: Shaft: MAC matrix

Shaft pair mode shapes couples: $3^{rd} - 4^{th}$, $8^{th} - 9^{th}$, $24^{th} - 25^{th}$ and $28^{th} - 29^{th}$

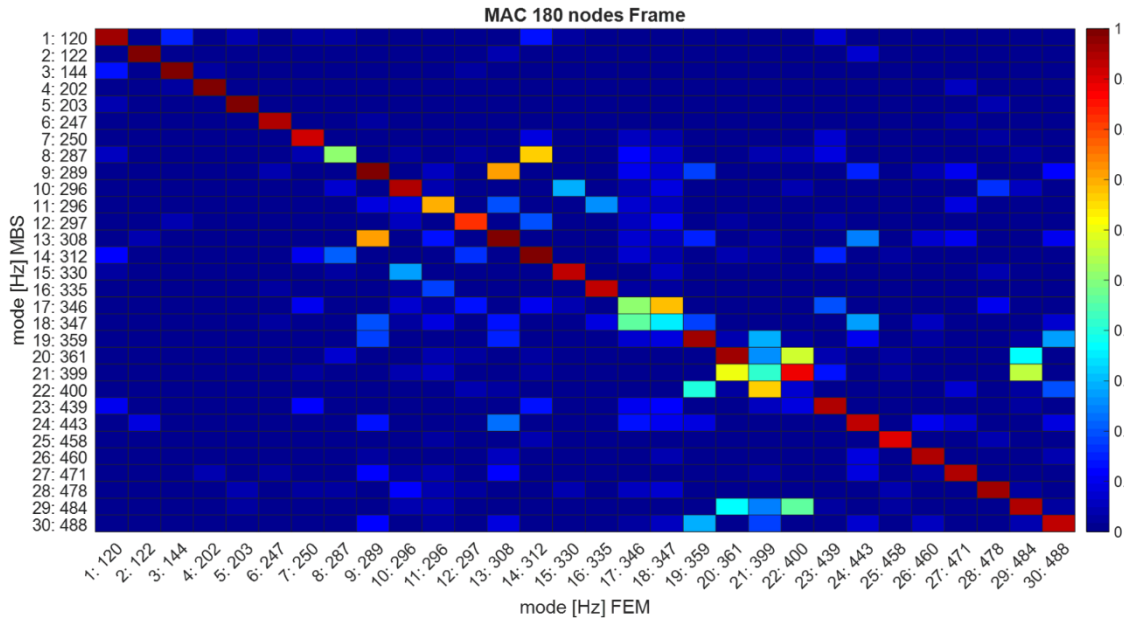


Figure 4.26: Frame: MAC matrix

Frame pair mode shapes couples: $17^{th} - 18^{th}$ and $21^{th} - 22^{th}$.

In this case the behaviour of 9^{th} mode is like 13^{th} mode and the behaviour of 8^{th} mode is like the behaviour of the mode number 14.

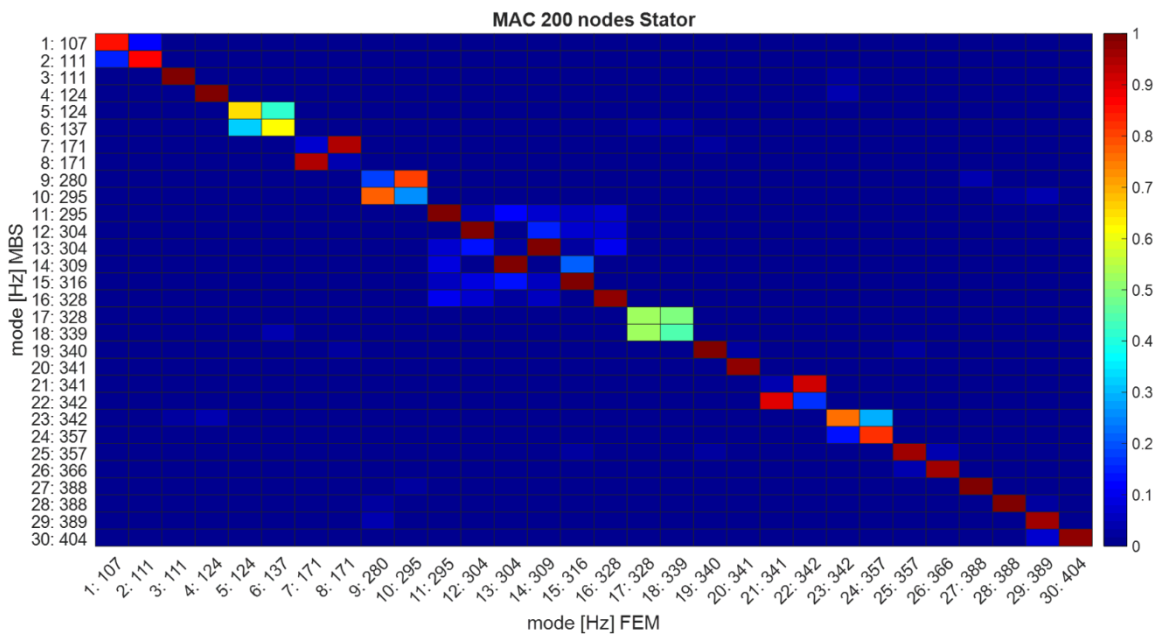


Figure 4.27: Stator: MAC matrix

Stator pair mode shapes couples: $7^{th} - 8^{th}$, $9^{th} - 10^{th}$, $13^{th} - 14^{th}$, $17^{th} - 18^{th}$ and $21^{th} - 22^{th}$

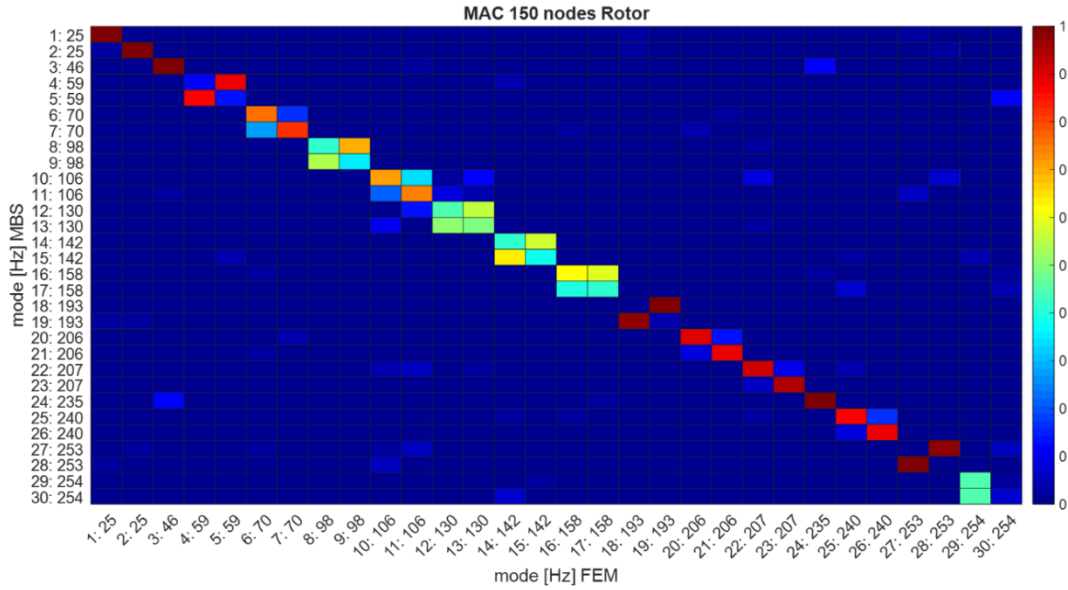


Figure 4.28: Connector: MAC matrix

Connector pair mode shapes couples: 16th – 17th, 23th – 24th, 25th – 26th and 27th – 28th

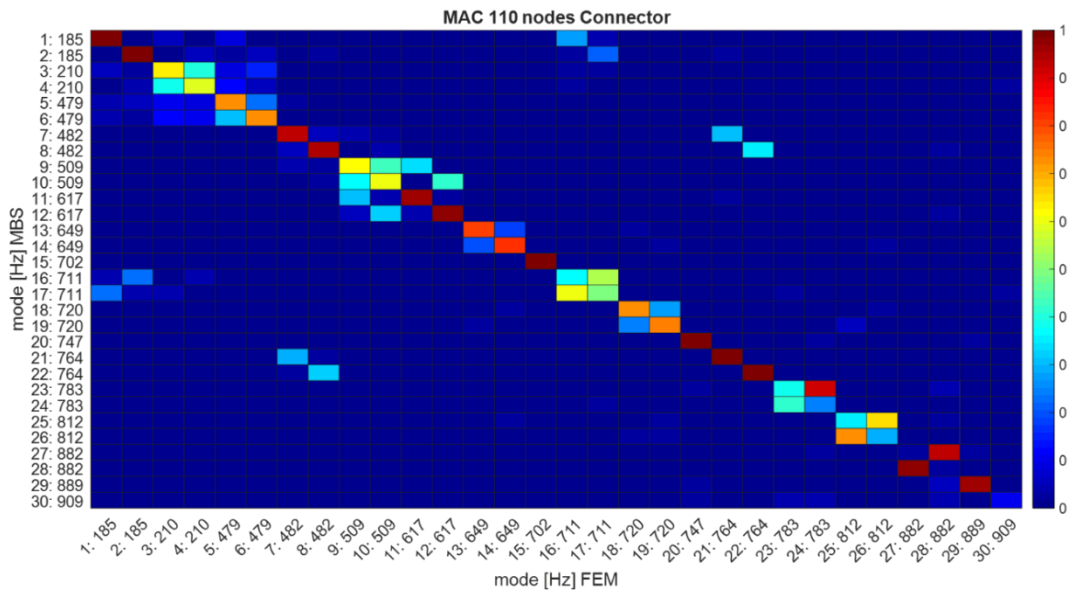


Figure 4.29: Rotor: MAC matrix

Rotor pair mode shapes couples: 4th – 5th, 8th – 9th, 12th – 13th, 14th – 15th, 16th – 17th, 18th – 19th and 27th – 28th

Every MAC matrix gives good results, along each main diagonal there are only value bigger than 0.5 and when it isn't it is because the mode shape is coupler with another mode shape with very close natural frequency, and ABAQUS and SIMPACK give them revers behaviour.

Figure 4.30 shows the auto FEM MAC matrix, on its main diagonal there are only value equal to 1 and outside there are only values close to zero, so the node-set chosen to the freedom reduction is good. Figure 4.31 shows the auto MBS MAC matrix, the matrix is symmetric, and it shows that the eigenmode number 2 3 4 5 have a similar behaviour respectively of 7 12 13 14. Figure 4.32 shows the MAC matrix between FEM and MBS, the first two modes in MBS and FEM have different behaviour and the behaviour of eigenmode number 11 and 25 are reversed, like also the behaviour of the eigenmode number 22 and 25, due to this the diagonal where there should be only 1 are shifted up.

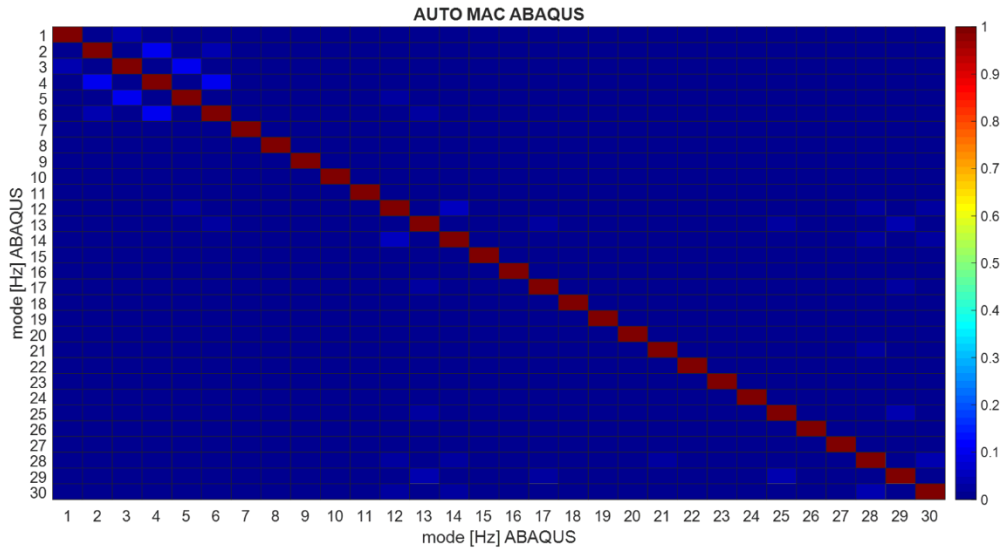


Figure 4.30: Auto MAC matrix FEM

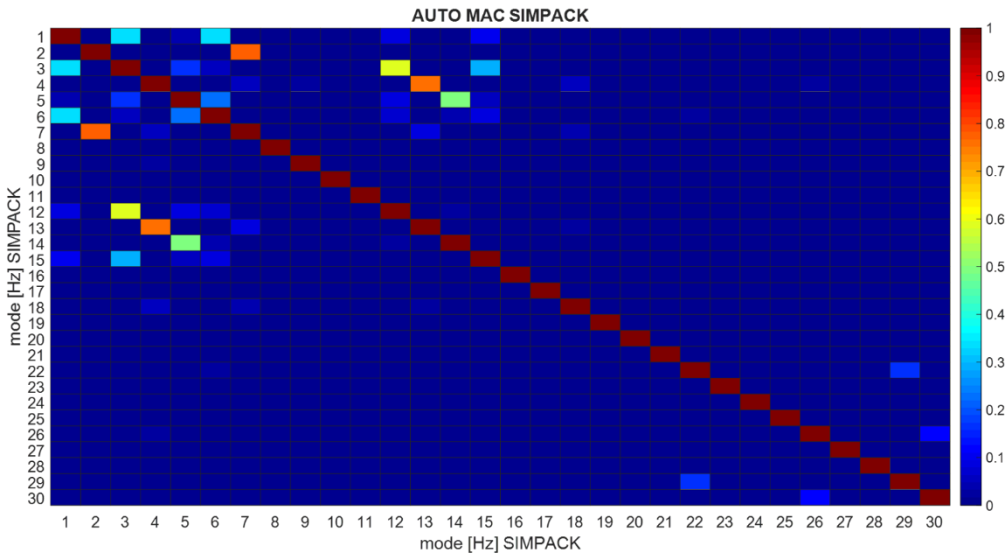


Figure 4.31: Auto MAC matrix MBS

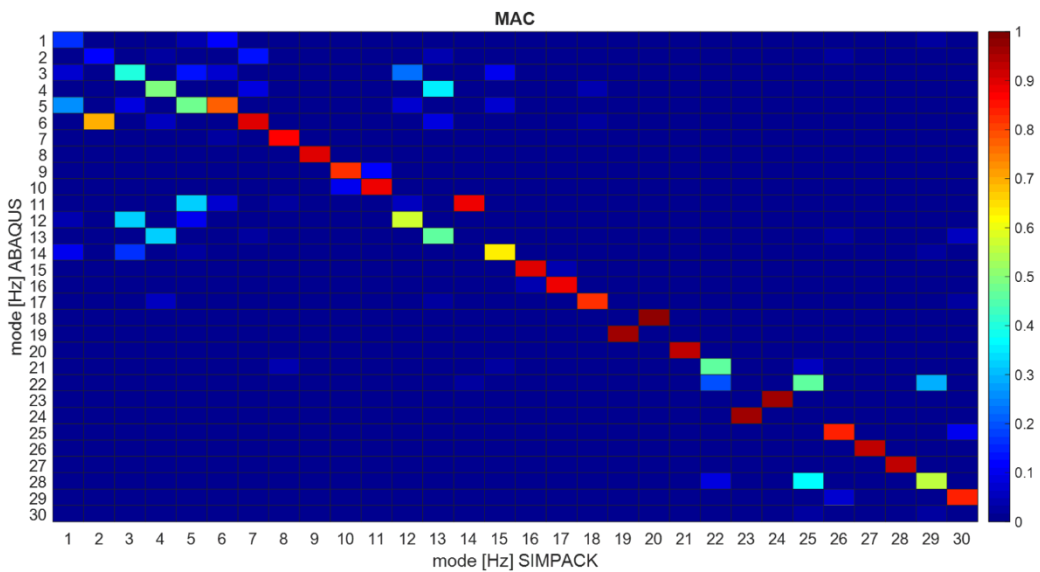


Figure 4.32: MAC matrix FEM - MBS

4.5 Tower

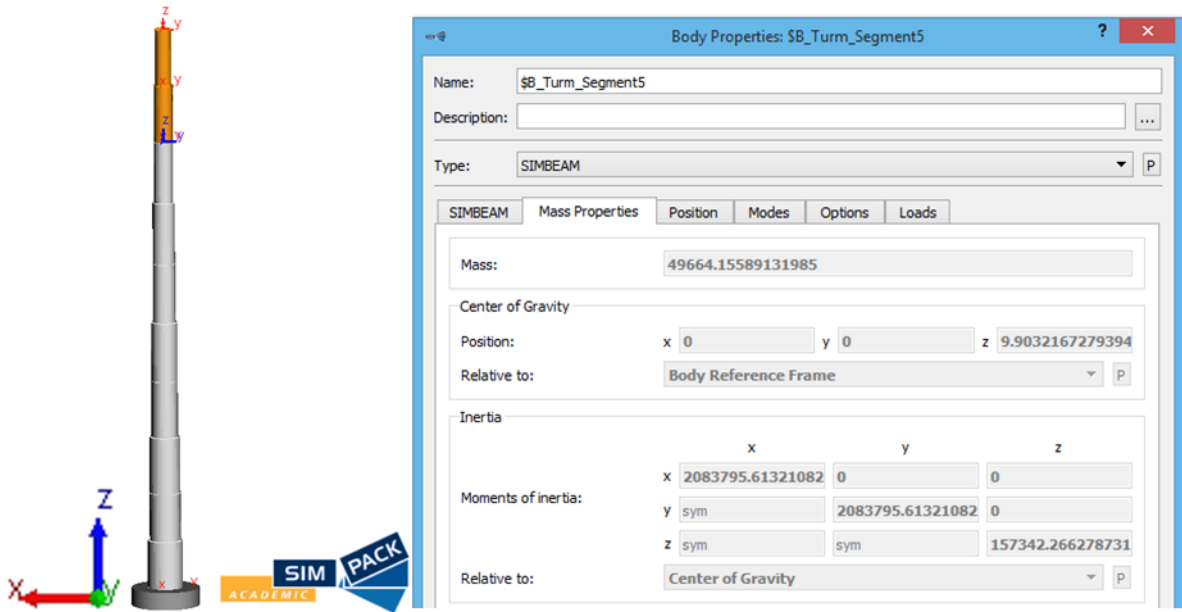


Figure 4.33: Tower SIMPACK model

The tower is modelled with five flexible bodies with different dimensions. Every part is modelled as Timoshenko beam by SIMBEAM body. Figure 4.33 shows how to make one body of the tower.

4.6 Blades

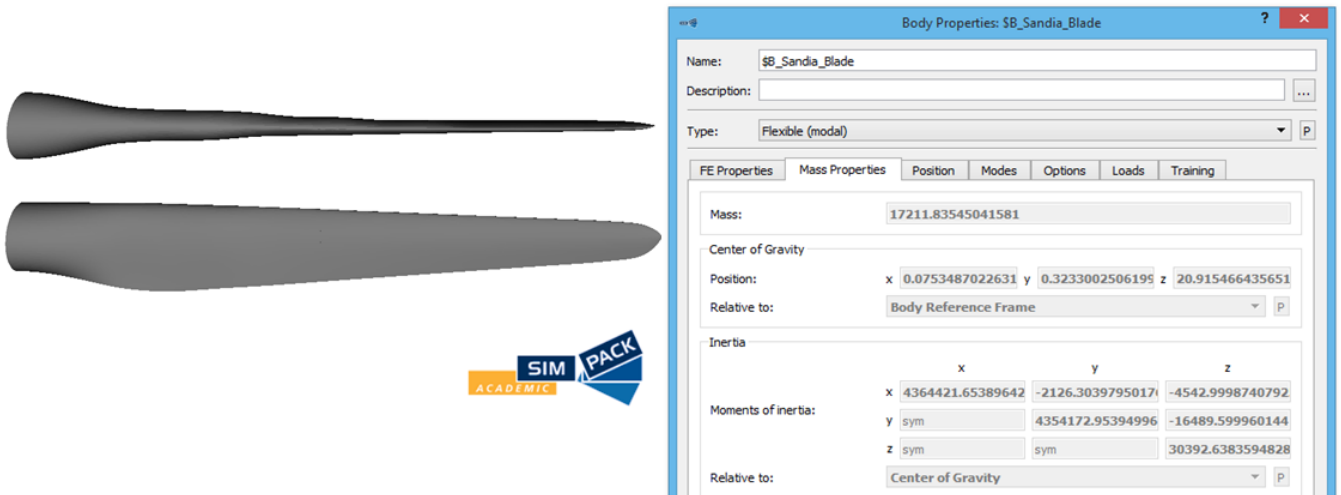


Figure 4.34: Blades SIMPACK model

Figure 4.34 shows the properties of one blade. The blades are modelled as modal flexible bodies, so their geometry has been made not in Simpack hence a *.fbi file from ABAQUS (or another CAD software) is needed. The mass for each blade without the adaptor is 17.21 ton, the mass of the blade with the adaptor is 27 ton. The adaptor is needed to have a rotor diameter equal to 130 m, because the length of the blades is 65 m and it cannot be changed. The adaptor is made by a SIMBEAM model with circular geometry depending on the dimension of the hub.

4.7 Entire model

In this chapter the whole models used for the simulation are showed. First of all, it is explained the finite elements model with special care in the air gap modelling. In the last part is described the MBS model.

4.7.1 Finite element model

The FEM model is showed in Figure 4.35. The properties of the mesh are showed in Table 4.10.

In Figure 4.35 it is possible to see that the x -axis is along the rotor-stator axis and not parallel to the ground, the reason for this choice is that it is easiest define the reference points in the middle of the generator in order to define the constraint for the bearings and for the magnetic pull. On the other hands all forces must be split in x -axis and z -axis. Table 4.11 shows the components in each direction and the magnitude of the forces that are considered in this thesis.

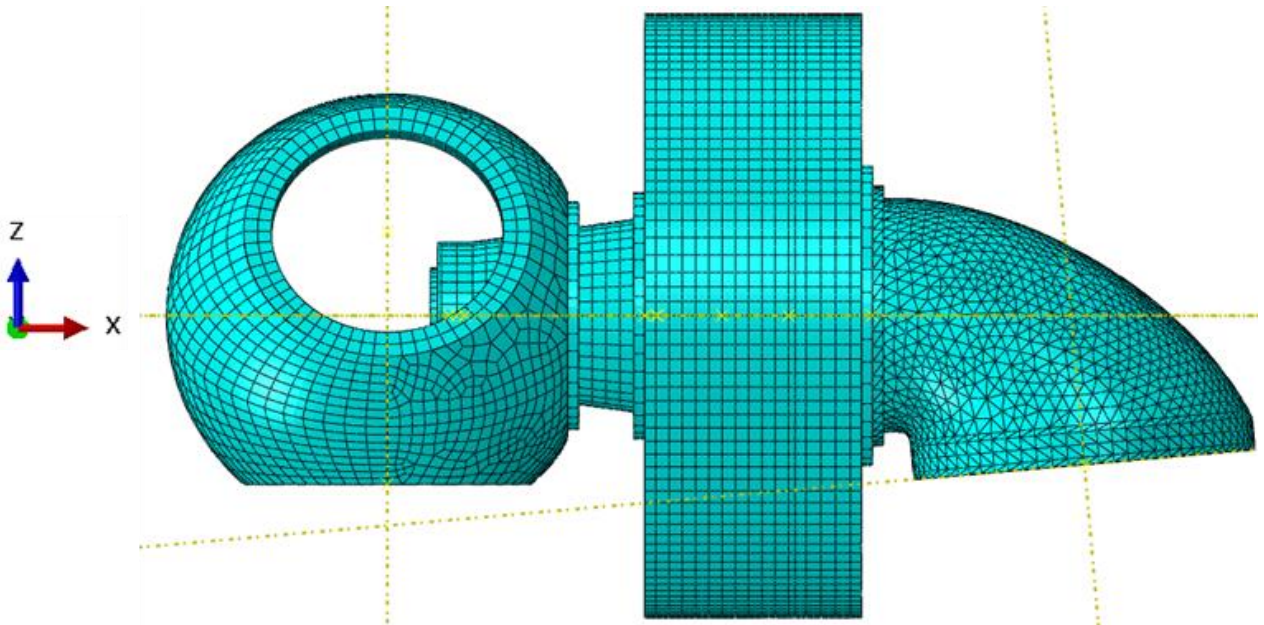


Figure 4.35: Generator F.E.M

The external forces and the boundary conditions have been applied in a reference point, which relates to the surface by a continuum distribution coupling. It has been chosen because it allows the movement of the surface where the constraint is applied. In Figure 4.36 is showed an example of this kind of constraint, it is the model for the blade's weight on one hub's hole.

Force	x	y	z	magnitude
Blade (x3) [N]	23'674	0	-270'595	271'628.62
Gravity [mm/s^2]	854.99	0	-9772.67	9'810
Wind force [N]	266'511	-41'000	-520'983	586'627.9
Wind torque [Nm]	$3 \cdot 10^9$	$1.53403 \cdot 10^9$	0	$3.37 \cdot 10^9$

Table 4.11: Forces and Moment

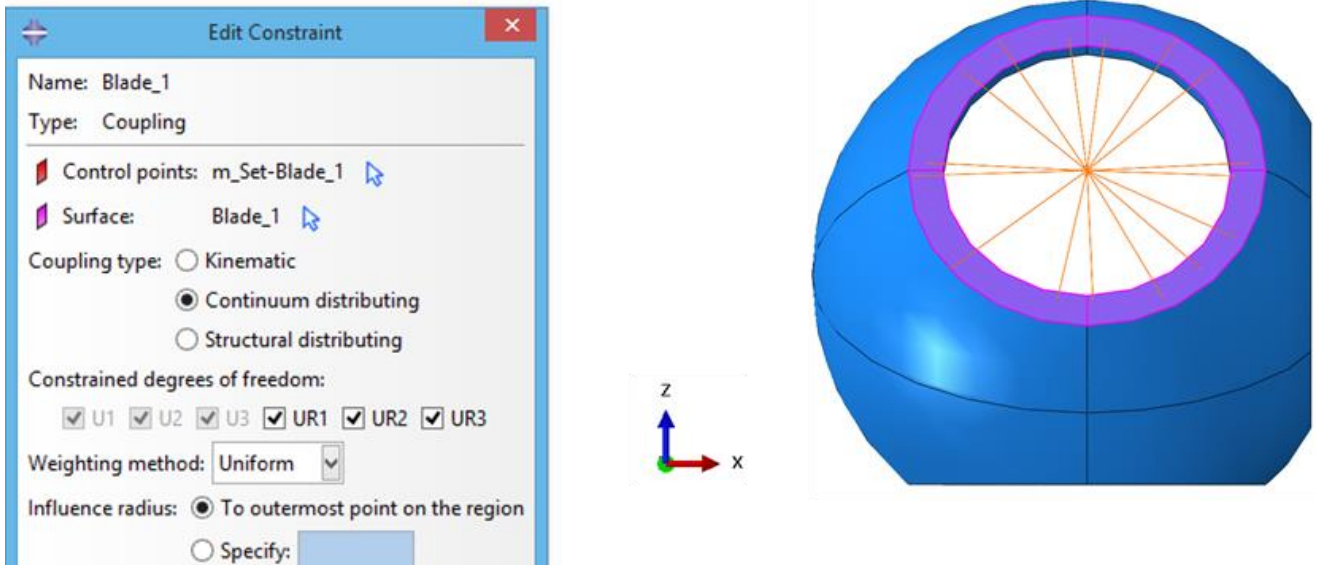


Figure 4.36: ABAQUS: constraint to apply the weight of the blades

The magnetic pull has been modelled like a bearing with negative stiffness. Five different models deep of magnetic pull have been simulated, the air gap surface has been split in: only one slice, three slices, five slices, ten slices and twenty slices. So, as the bearing, for each slice two reference point, one constrained with the external surface of the rotor and the other one constrained with the internal surface of the stator, joint by a wire are used. Also, in this case a radial trust connector element has been used. The magnetic pull for every model deep is showed in Figure 4.37.

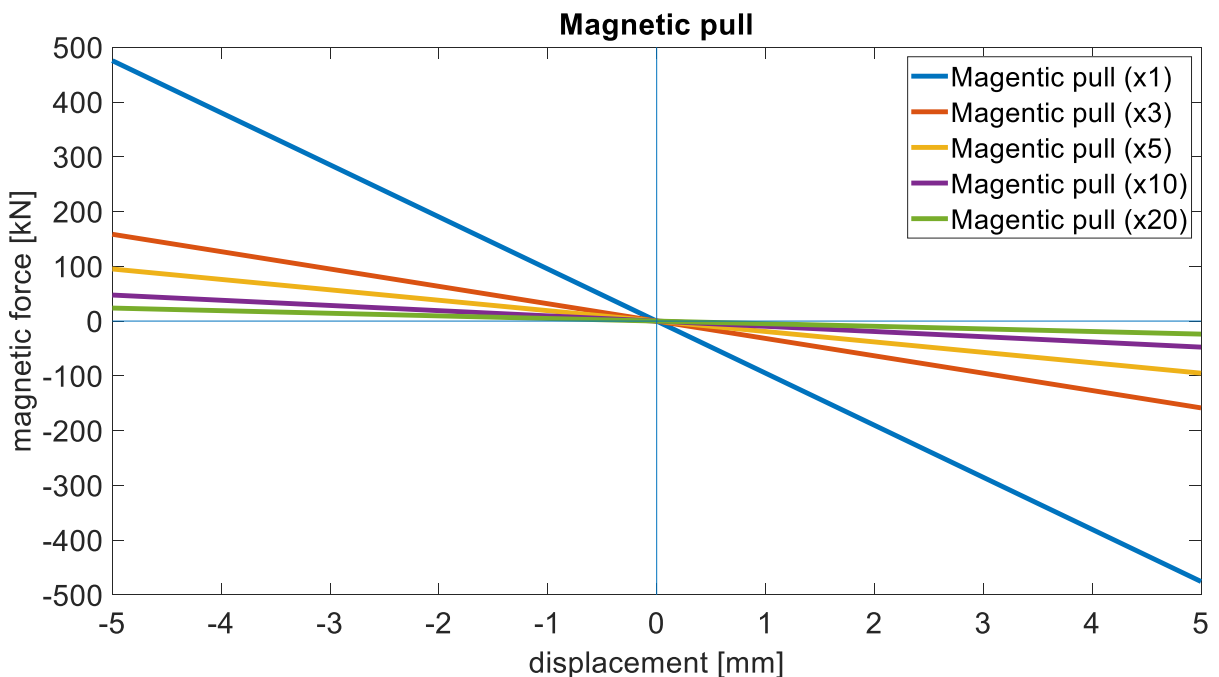


Figure 4.37: Magnetic pull for different model deep

x1-3-5-10-20 mean in how many slices the air gap has been split up to model the magnetic pull

Figure 4.38 is showed the ABAQUS model for the magnetic pull with one slice, the constraint coupling continuum distribution has been used to constrain the control points with the surfaces and a wire has been used to join the control point and to allow the communication between the stator and the rotor. The tie constraint has been used to connect the components when they are fix with each other. This kind of constraint has been chosen because it ties two surfaces together for the duration of a simulation. In Figure 4.39 is showed

an example of tie constraint, it is the constraint between the machine frame and the shaft.

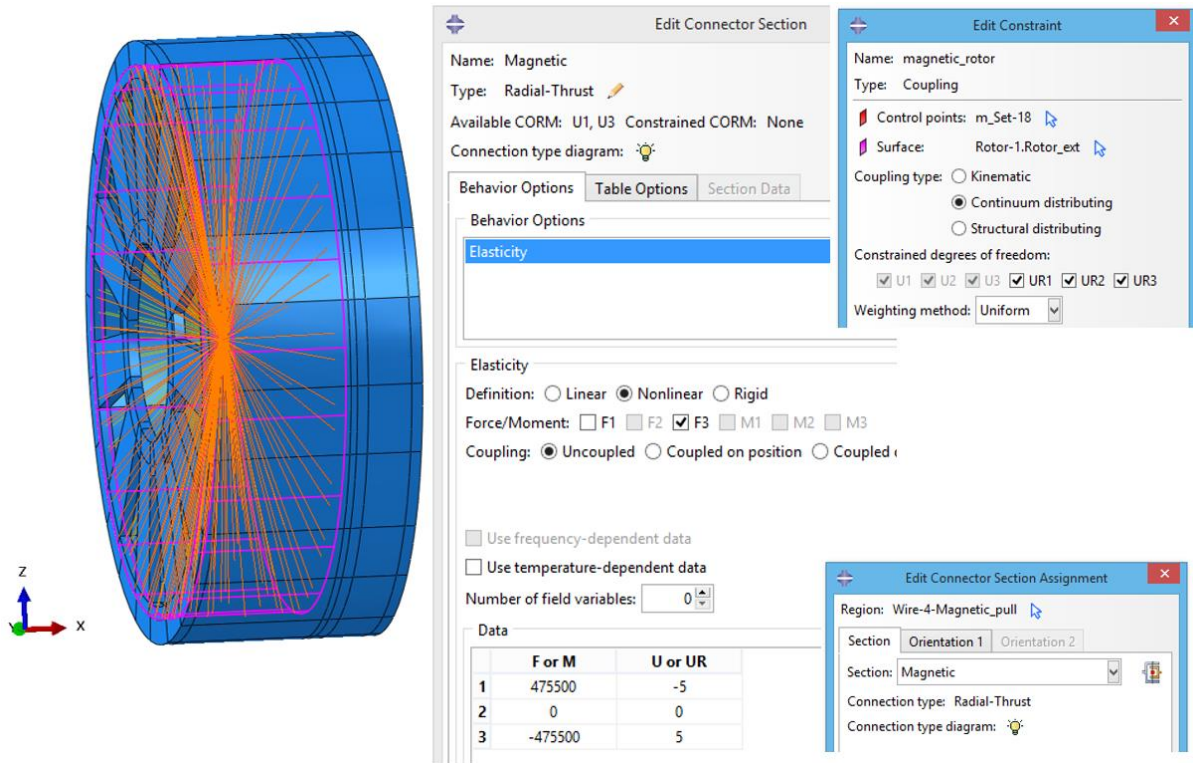


Figure 4.38: ABAQUS: Connector- constraint-wire to apply the magnetic pull with one slice

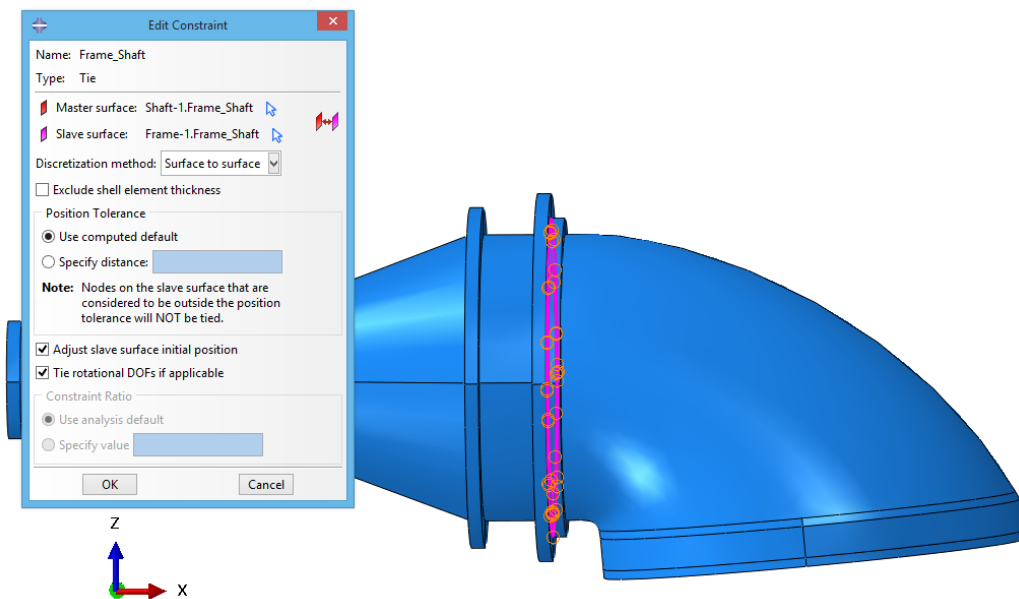


Figure 4.39: ABAQUS: tie constraint between frame and shaft

4.7.1.1 Air gap

The air gap has been modelled as an interaction between stator and rotor. In ABAQUS there are two possible discretization method to model an interaction: Surface to Surface and Node to Surface. Both methods need of one master surface and one slave surface. In the node to surface method each slave node is projected on one side of a contact interface effectively interacts with a point of projection on the master surface on the opposite side of the contact interface, hence the slave surface can be defined as a group of nodes- a node-

based surface. The contact direction is based on the normal of the master surface [27]. The surface to surface method considers the shape of both the slave and master surfaces in the region of contact constraints. Contrary to the node to surface method, the contact direction is based on an average normal of the slave surface in the region surrounding a slave node and the averaging regions are approximately centered on slave nodes, so each contact constraint will predominantly consider one slave node but will also consider adjacent slave nodes [27].

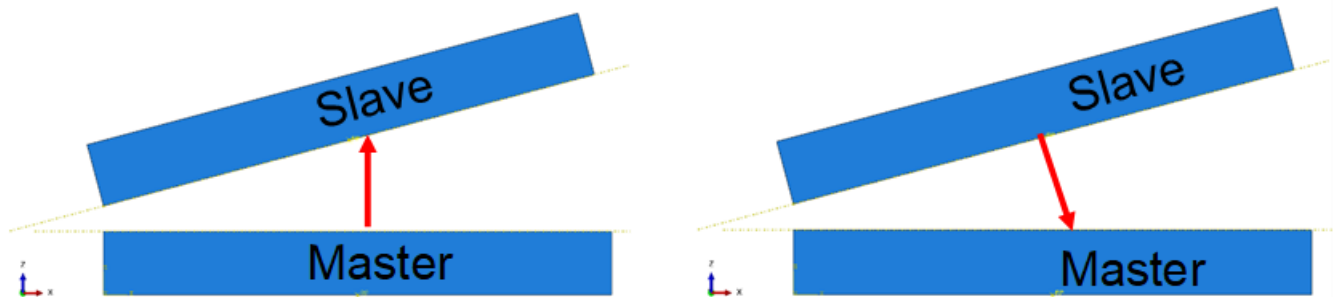


Figure 4.40: Sketch of: Node to Surface & Surface to Surface

Figure 4.41 are showed the static simulations of the two plates in Figure 4.40. Both plates are fixed and between them there is an angle equal to 30° , there is no load applied. The clearance between the surfaces has to change if the discretization method or the master and slave surface change. In the Figure 4.41 is showed how the distance output change if one parameter changes. As far as the clearance is concerned in the simulations the only comparisons that make sense are between the simulations a.1 and b.2 and between the simulations a.2 and b.1. The difference between the simulation a.1 and b.2 is equal to 0.04 mm , that is 0.18% of the clearance in the simulation a.1.

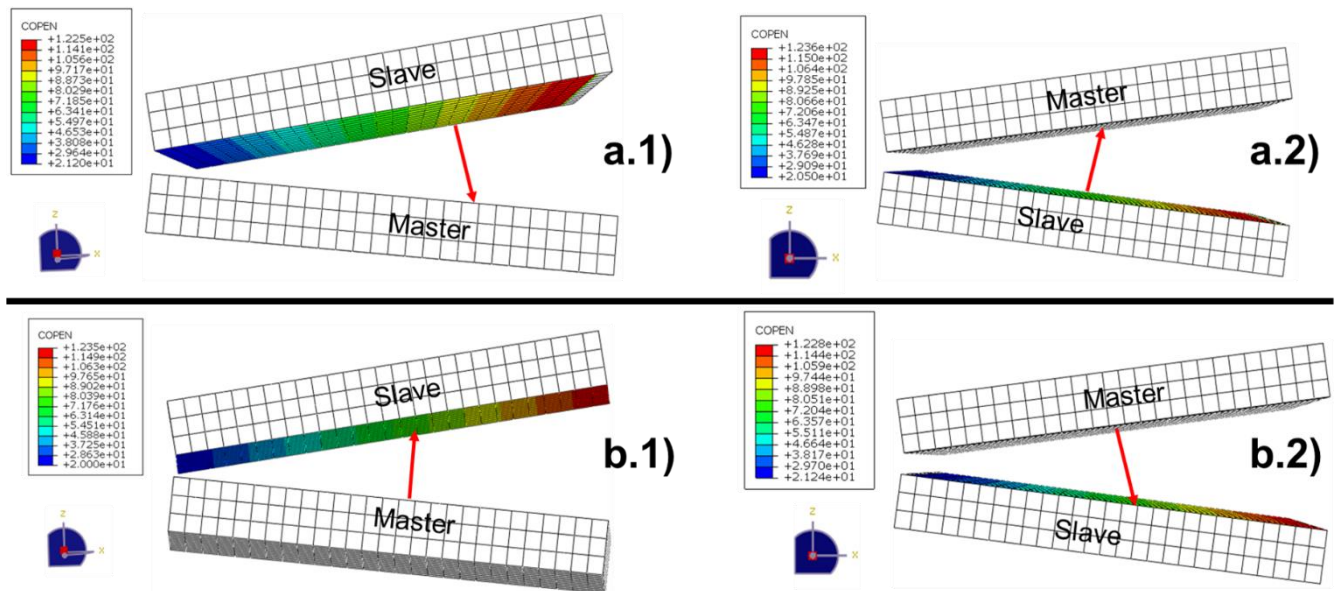


Figure 4.41: COPEN output static simulation of two plate. a) Surface to surface & b) Node to surface

The difference between the simulation a.2 and b.1 is equal to 0.5 mm , that is 2.5% of the clearance in the simulation b.1. So, it is possible to claim that the two method measure the same distance if the master and the slave surface are the same. If the master and the slave surface are reversed the result could change depending on the geometry of the problem. In this case the difference between a.1 and a.2 is 0.7 mm (3.3%) and between b.1 and b.2 it is 1.24 mm (6.2%), hence the effect of the master and slave surface is lower in surface to surface method.

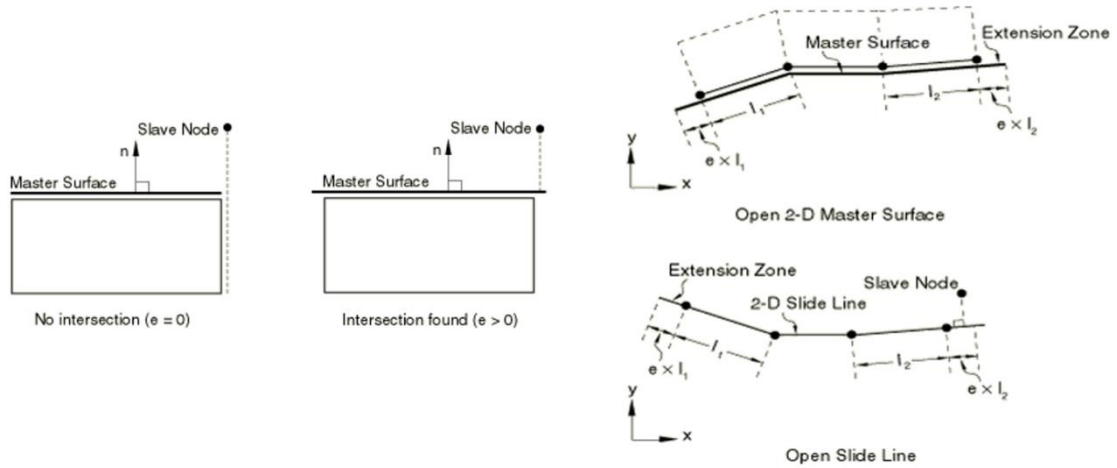


Figure 4.42: Missing Master surface problem [27]

The main problem of the node to surface method is the “master surface missing” (Figure 4.42), it means that a slave node misses the interaction with the opposite side of the master surface. This problem could be resolved by adding an extra master surface, but the length of the extra master surface has to be specificity in the input file and must not be more than 20% of the master’s surface length [27]. This problem doesn’t exist in the surface to surface method, if the sliding is less than the length of one element, because the constraint formulation considers the region of the slave surface near a slave node. For this region the extra surface is not allow in the surface to surface method.

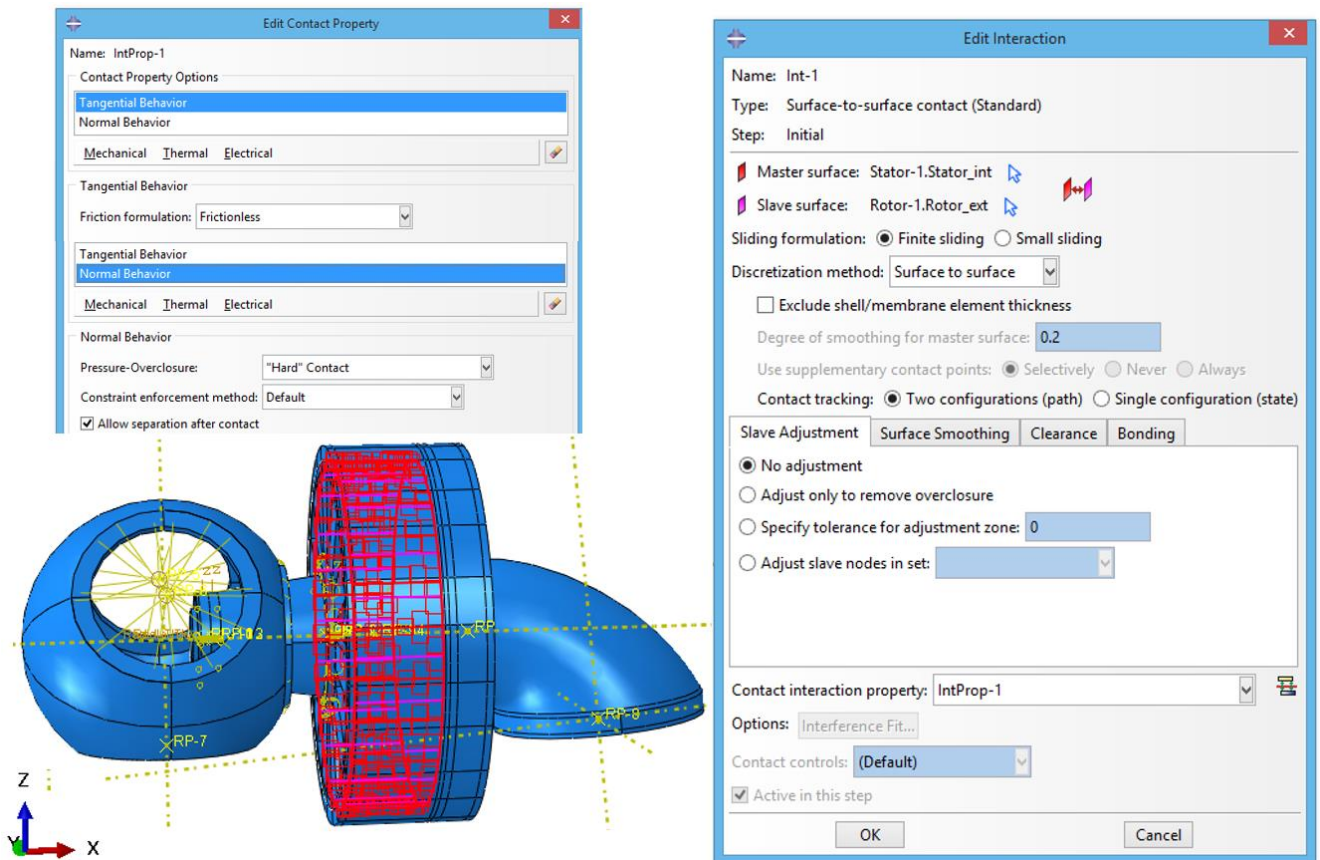


Figure 4.43: ABAQUS: air gap modelling

In this thesis in order to model the air gap behaviour an interaction with “Finite sliding” formulation has been used, it is the most general and allows any arbitrary motion of the surfaces, and with “Surface to Surface” as

discretization method. The rotor's external surface has been chosen as slave surface but, in this case, even if the master and slave surface are reversed the results don't change. Paragraph 5.1 shows what happens when the surfaces are reversed. The Surface to Surface has been selected because during the motion stator and rotor won't be misaligned: this means no master surface missing and no need to add extra master surface, which it is unknown. The surface to surface contact using surface-to-surface discretization is also less sensitive to master and slave surface designations than node-to-surface contact. The surface-to-surface formulation is primarily intended for common situations in which normal directions of contacting surfaces are approximately opposite.

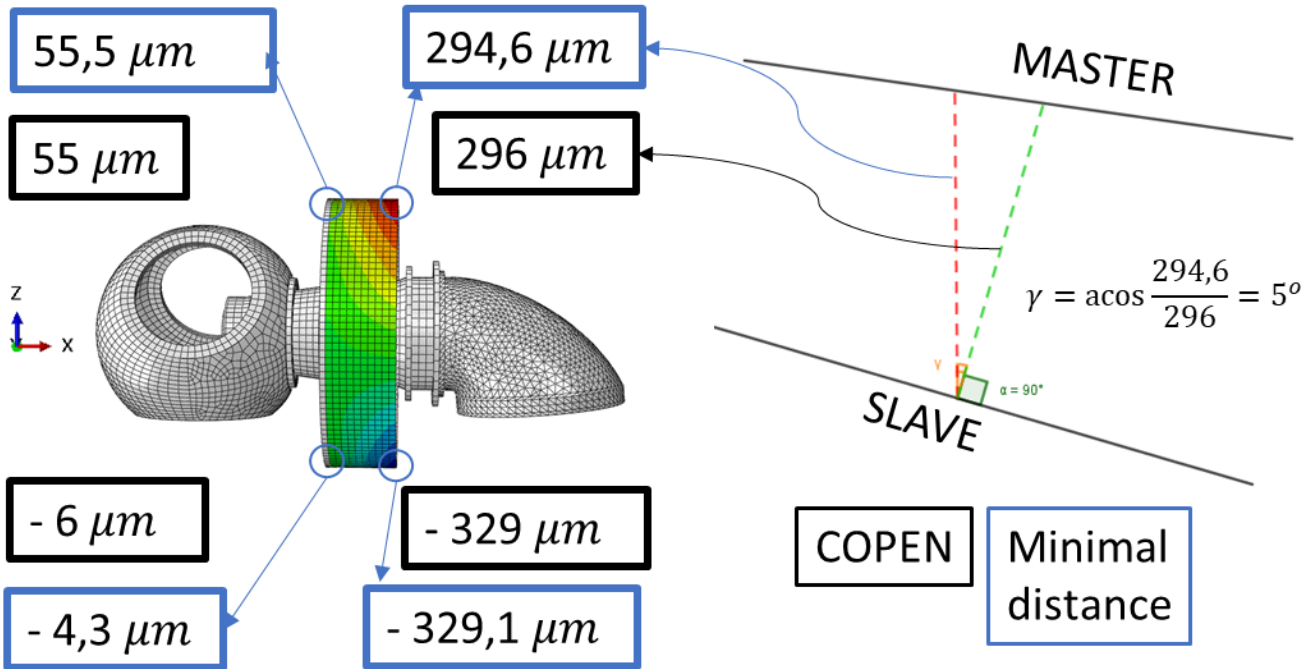


Figure 4.44: Comparison between COPEN and minimal distance

In Figure 4.44 is showed the COPEN output of one analysis made during the simulations. It is compared with the minimal distance between two surfaces, the difference between them is always lower than 2 micro meter so, the conclusion is that the clearance measure by COPEN can be approximated as the minimal distance. To validate the model one simulation without loads has been done in ABAQUS. Figure 4.45 shows the results of that simulation, it possible to see that the distance between stator and rotor is 5 mm in each point of the air gap and the magnitude displacement of the whole model is 0. These results confirm that the model is in the right configuration before starting all other simulations.

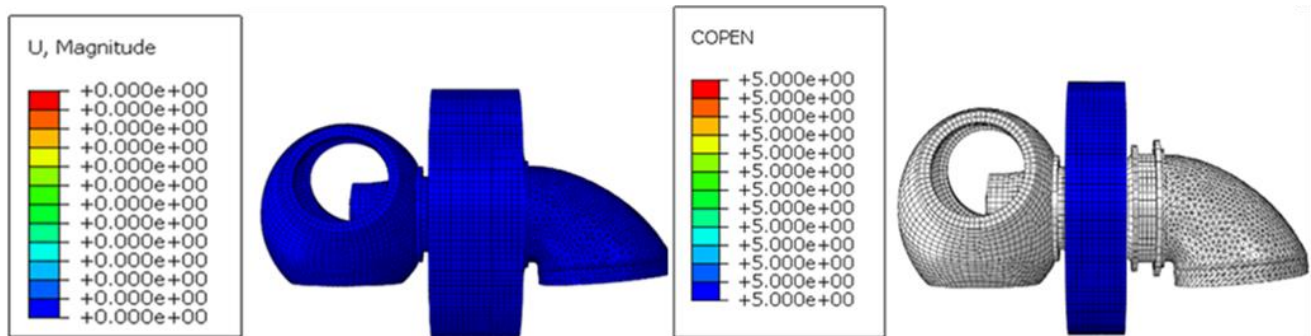


Figure 4.45: Magnitude displacement of whole system & Air gap clearance – Simulation WITHOUT LOADS

4.7.2 Multi body model assembled

In order to make the MBS model the freedom reduction of the FEM generator parts has been done. During the freedom reduction two, or more, bodies that are constrained with the tie constraint can be reduced as only one body, so the hub, the connector and the rotor have been reduced in one part (the Rotor part) and the machine frame, the shaft and the stator have been reduced in another part (the Stator part). The coupling constraints can be reduced but their control point shall be indicated in the input file (*.inp) before to run the job in ABAQUS. Figure 4.46 shows the rotor part and figure Figure 4.47 shows the stator part, both bodies are flexible body and for each of it the first 100 eigenmode have been reduced.

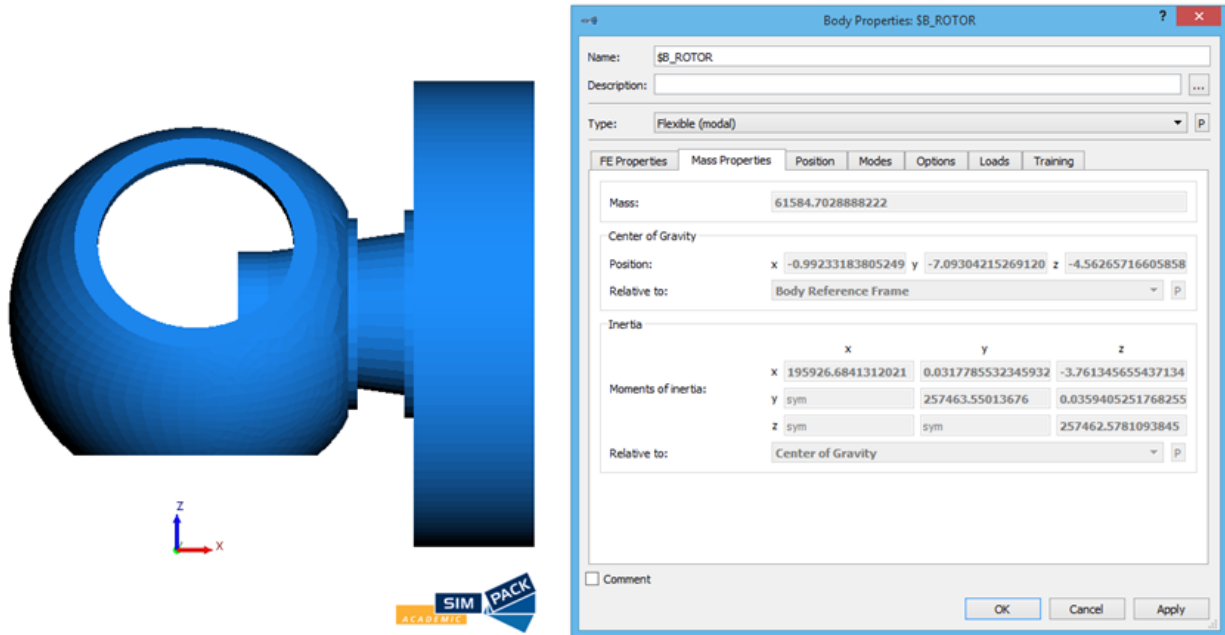


Figure 4.46: Rotor MBS part

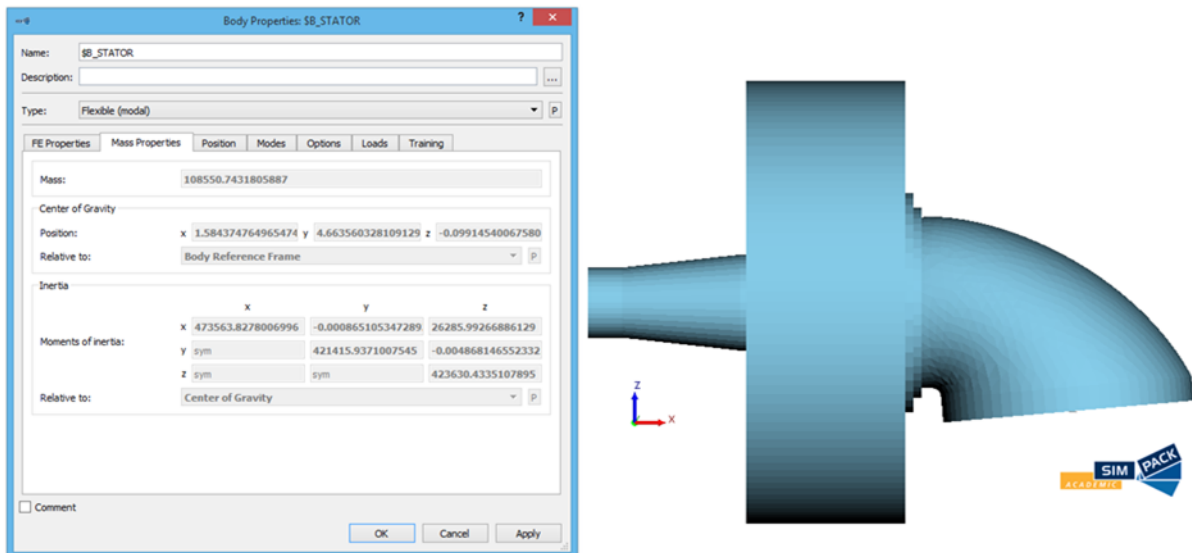


Figure 4.47: Stator MBS part

Figure 4.46 and Figure 4.47 show also the marker of fixed bearing, loosed bearing, magnetic pull, bleads and tower. The bearings stiffness has been modelled for each bearing with a force element type bushing Cmp, this kind of element applying spring and damper forces and torque between two markers in multiple direction axis direction and it doesn't allow clearance between the markers [34]. The magnetic pull and the and the blades weight have been modelled as force element type spring damper parallel Cmp, this kind of element applies

spring and damper forces between two markers in axis multiple directions and it allow optional clearance between the markers. Figure 4.48 shows how to make the force element in Simpack and the 2D model of the Generator, there are three element type 43 (Bushig Cmp) one element type 5 (Spring damper parallel Cmp) and the constraint (6 *dof* for fix the position of the bearing and 0 *dof* to fix the stator).

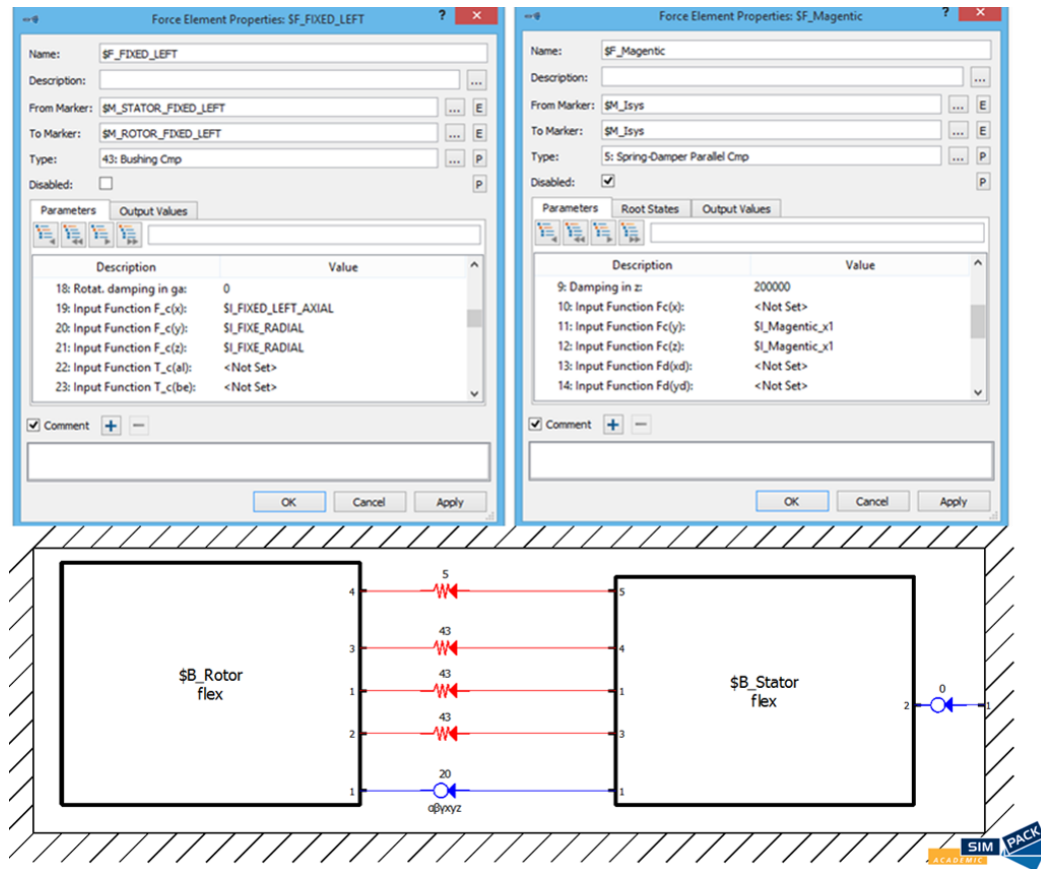


Figure 4.48: Force element type and 2D Generator model

The study of the air gap displacement has been done by the study of the displacement between the marker constraints with the internal surface of the stator to the marker constraints with the externa surface of the rotor, hence a sensor between these two markers is needed. Figure 4.49 shows the implementation of the sensor.

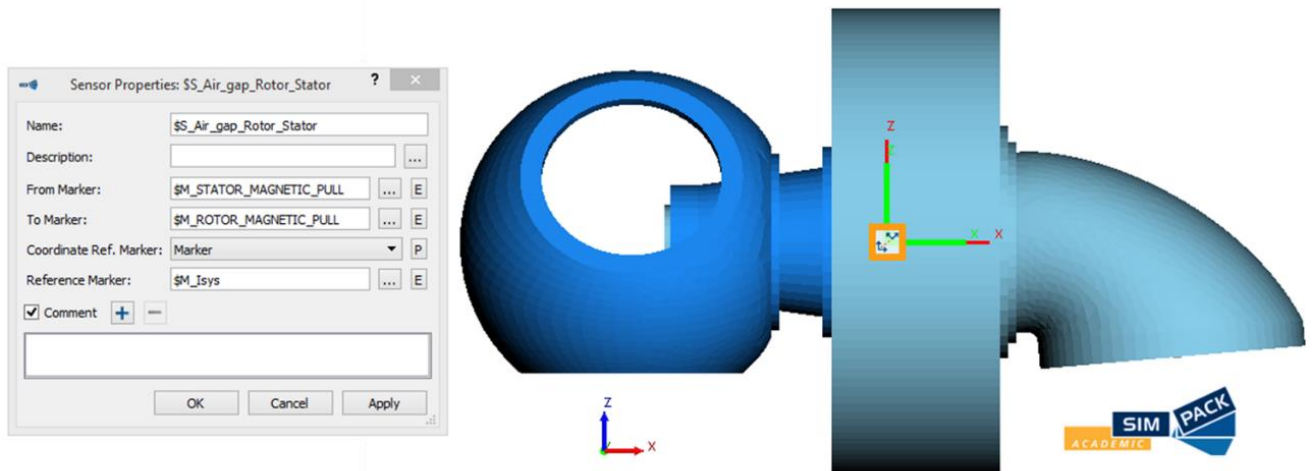


Figure 4.49: SIMPACK sensor to study the air gap displacement

The properties of the blades and the tower are explained respectively in paragraph 4.5 and paragraph 4.6. Figure 4.50 shows the 2D model of the all wind turbine. It possible to see that the blades are constrained to

the hub with a rheonomic 1 *dof* joint, it is to allow the yaw moment that is needed to move the blades depending the wind direction. The only rigid body is the foundation because it is normally made by the reinforced concrete.

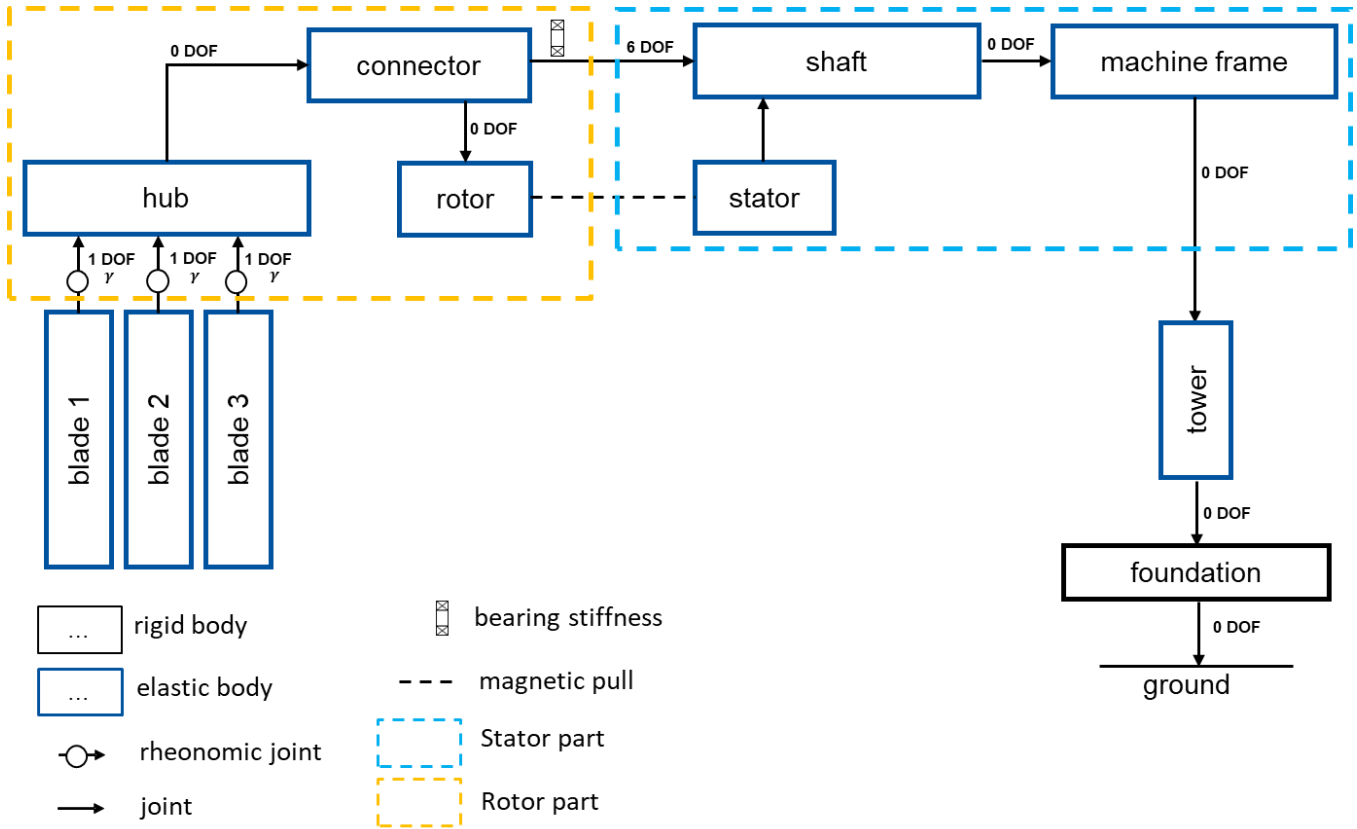


Figure 4.50: 2D model of the wind turbine

5. Simulation results

This chapter shows and explains the results of each simulation. The first part illustrates how the results are presented. The second part shows the result of the FEM simulation and then the comparison between FEM and MBS. At the end of the chapter the Campbell diagram of the whole wind turbine is explained.

5.1 Air gap displacement

The air gap's displacement has been plotted in a 2D-diagram: the abscissa represents the angle theta (θ) around the whole air gap surface, the ordinate represents the length (x) of the airgap and every cell of the matrix represents the air gap displacement (positive if the clearance increases and negative if the clearance decreases).

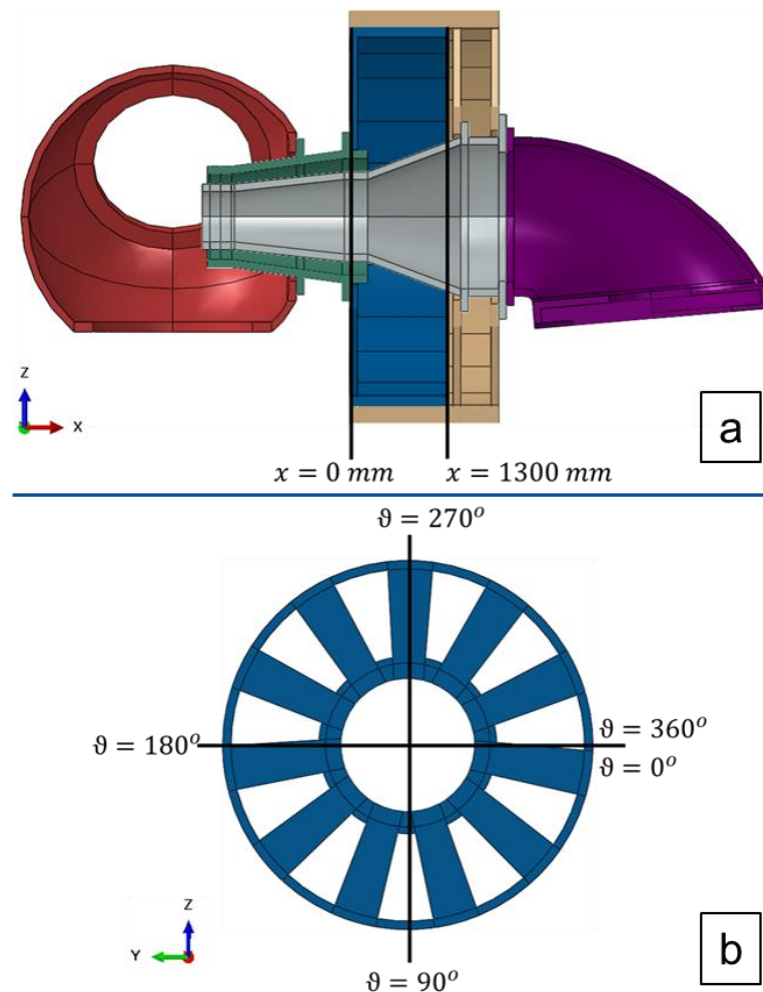


Figure 5.1: a) Side view of generator & b) Front view of rotor

In Figure 5.1 a is defined the ordinate axis (x) as:

- $x = 0$ is the air gap's part on the rotor's arms and closer to the hub;
- $x = 1300 \text{ mm}$ is the air gap part closer to the stator's arms where there are no rotor's arms.

In Figure 5.1 b is defined the abscissa axis as:

- $\vartheta = 90^\circ$ is the bottom part of the air gap
- $\vartheta = 270^\circ$ is the top part of the air gap

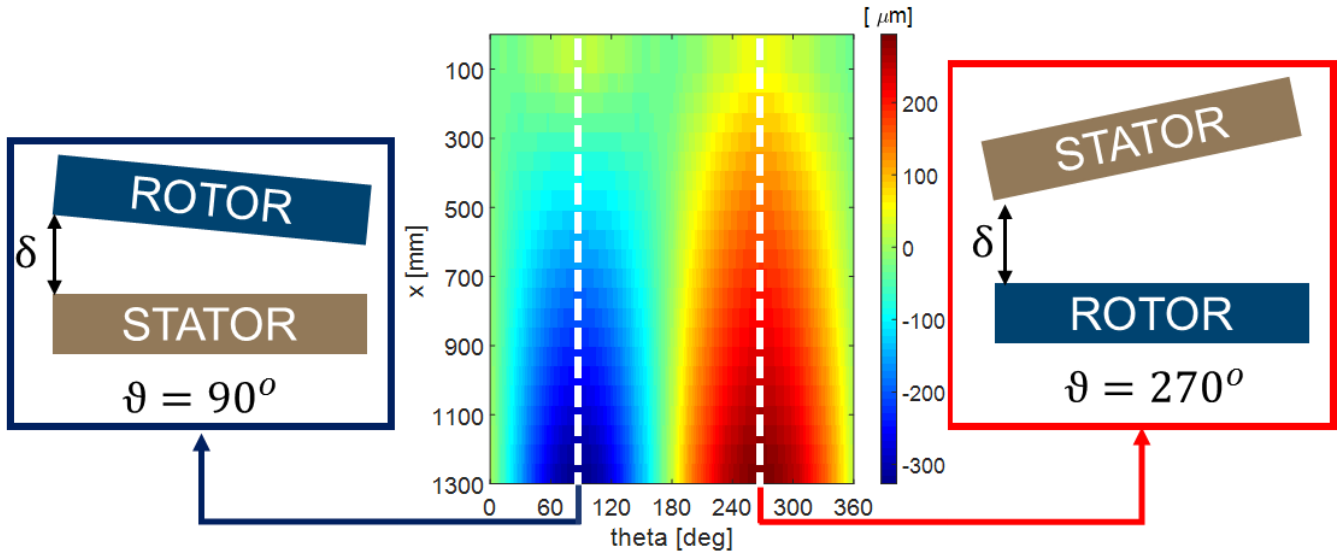


Figure 5.2: Air gap 2D plot example

Figure 5.2 shows an example of the plot that has been used to describe the air gap displacement. Along the all length of the air gap to 90° (bottom part) there is at $x = 0 \text{ mm}$ almost no displacement and at $x = 1\,300 \text{ mm}$ there is a decrease of about $300 \mu\text{m}$. Along the all length of the air gap to 270° (top part) there is at $x = 0 \text{ mm}$ almost no displacement and at $x = 1\,300 \text{ mm}$ there is an increase of about $290 \mu\text{m}$.

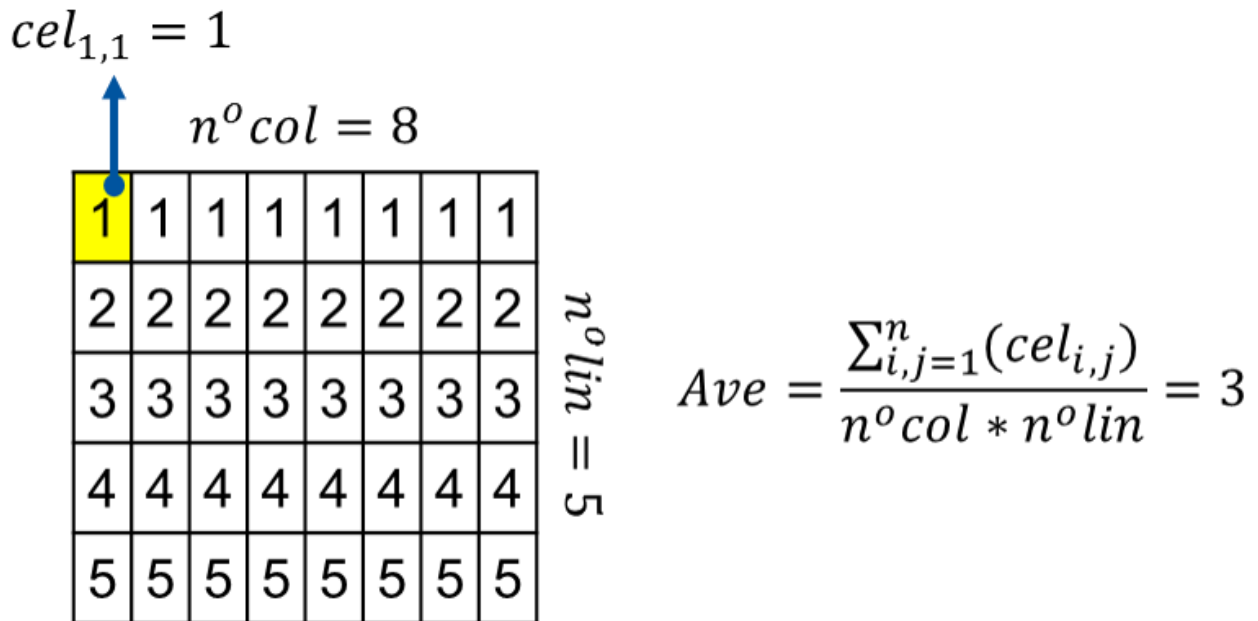


Figure 5.3: Air gap average displacement calculation

The graph used to show the air gap displacement is basically a matrix, hence in order to analyse the global displacement the average between each cell has been calculated. The average displacement is the sum of each cell divided by the number of cells. Figure 5.3 shows a very easy example of how to make the average (*ave*).

In order to see how the result change if the master and the slave surface are reversed the first two simulation that have been done are the simulation with the impact of the gravity and the blades weight with the master and slave surfaces reverse. The results are in Figure 5.4.

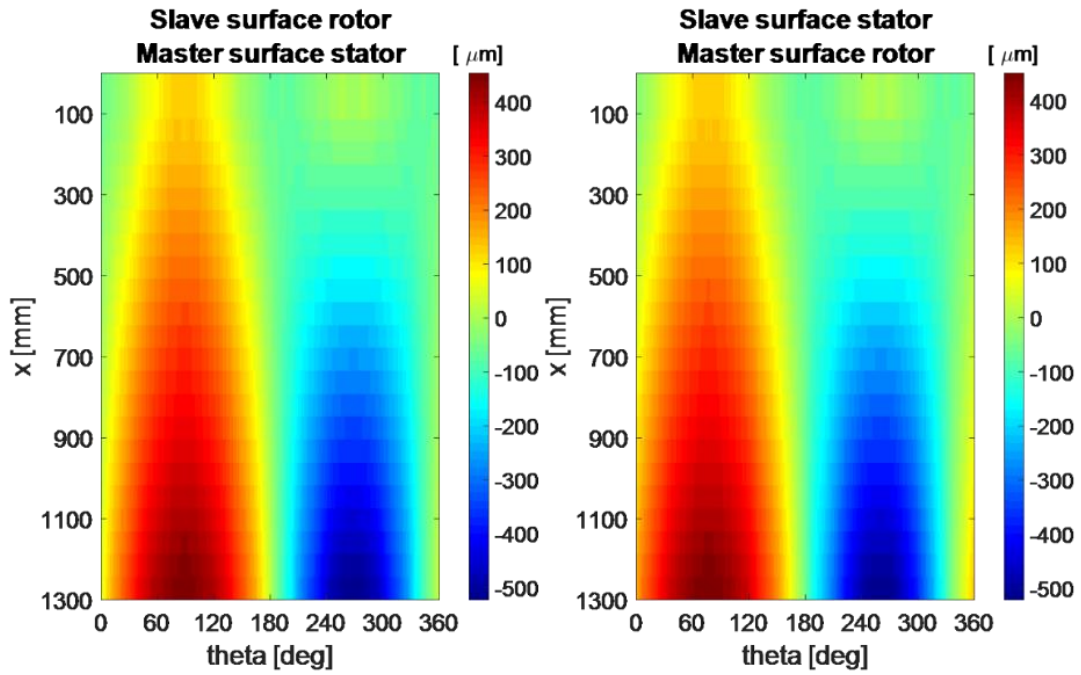


Figure 5.4: Air gap displacement distribution

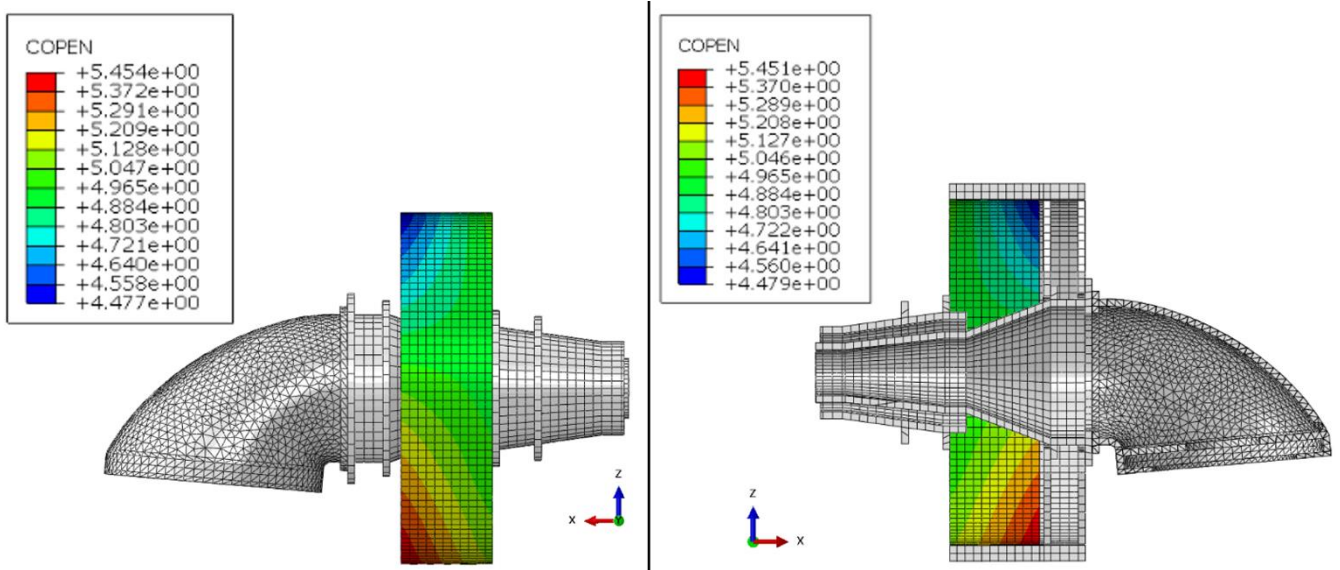


Figure 5.5: ABAQUS COPEN: slave surface rotor & slave surface stator

Slave surface	Max. increase[μm]	Min. decrease[μm]	$\theta - \text{max}$ [°]	x-max [mm]	$\theta - \text{min}$ [°]	x-max [mm]
Rotor	454	523	90	1'300	270	1'300
Stator	451	521	90	1'300	270	1'300

Table 5.1: Maximum and minimum displacement: slave surface rotor & slave surface stator

In Figure 5.4 and Figure 5.5 and Table 5.1 are showed the differences if the master and slave surface are reversed. The differences are always lower than 1% and the displacement distribution is almost the same, it means that the influence of the slave and master surface could be neglected. In the next simulations the master surface is the internal surface of the stator and the slave surface is the external surface of the rotor.

5.1.1 Static finite element simulation

Due to the high stiffness of the model, during the static analysis, an artificial damping needs to be implemented, without it the simulation doesn't converge. Figure 5.7 shows how the damping has been added to the whole model. More damping has been added also on the bearings, Figure 4.7 shows how to add it.

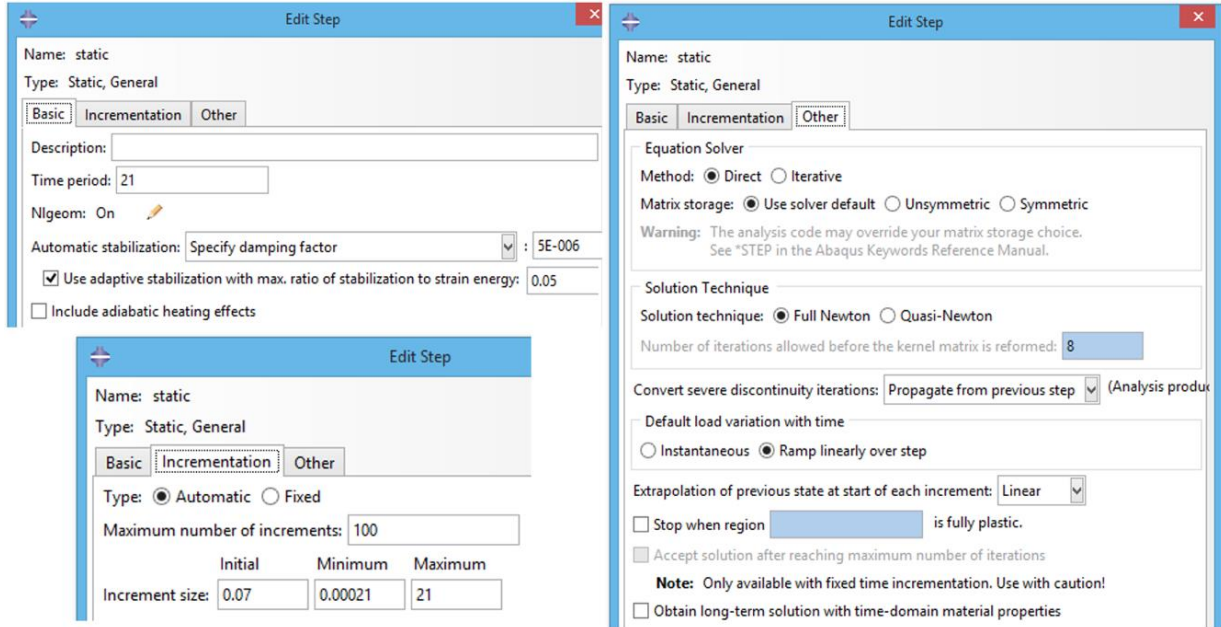


Figure 5.7: ABAQUS: stabilization of the system by the specific damping factor

A damping factor equal to $5 \cdot 10^{-6}$, combined to the damping on the bearings, in this case, is enough to stabilization the system. When more damping is added in the model, the energy dissipated by the artificial damping (ALLSD) must be maximum 10% times to the strain energy of the system (ALLSE). If the static stabilization energy (ALLSD) is bigger the strain energy (ALLSE) the results of the simulation are not reliable, so the damping factor has to be decrease until this condition is satisfied. Even if the loads in the simulation are not as function of time the time period of the simulation has been increase until 21 s in order to allow at the energy to get a good value. Figure 5.8 presents the plot of the strain energy and the static dissipation energy for the simulation with only the gravity. The plots for the other simulation are showed in the appendix.

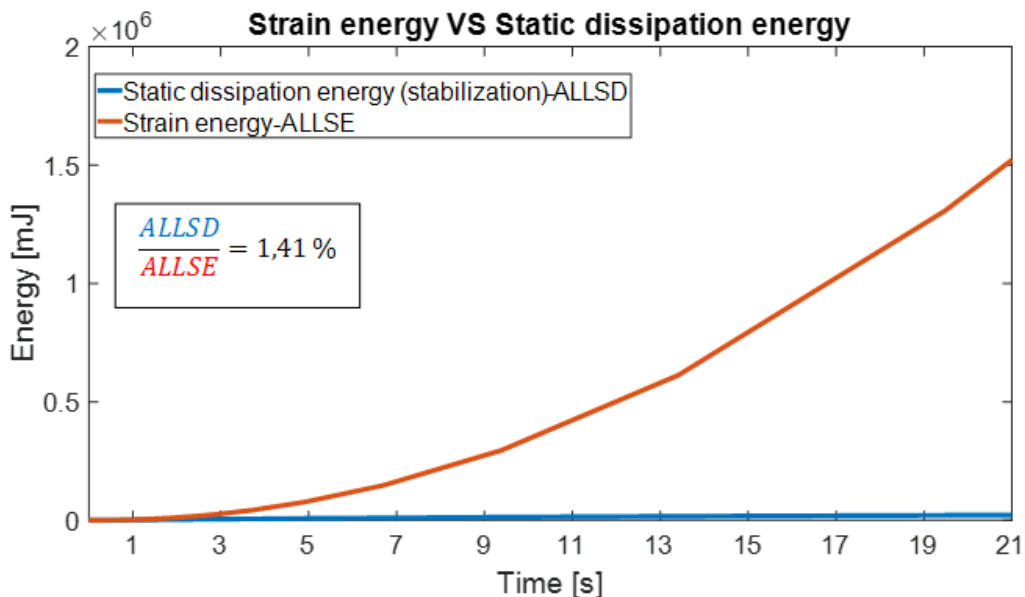


Figure 5.8: ABAQUS plot of ALLSD and ALLSE

Figure 5.8 shows that ALLSD is 1.41% of the ALLSE, it means that the damping factor added to the model is not too big and that the results of the simulation are reliable.

The simulation without any kinds of loads has been done as first simulation, in order to see if all component of the model was in the right position and if the MATLAB script written to plot the displacement distribution worked in the right way. The ABAQUS output are showed in Figure 4.45 and the MATLAB plot is in Figure 5.9.

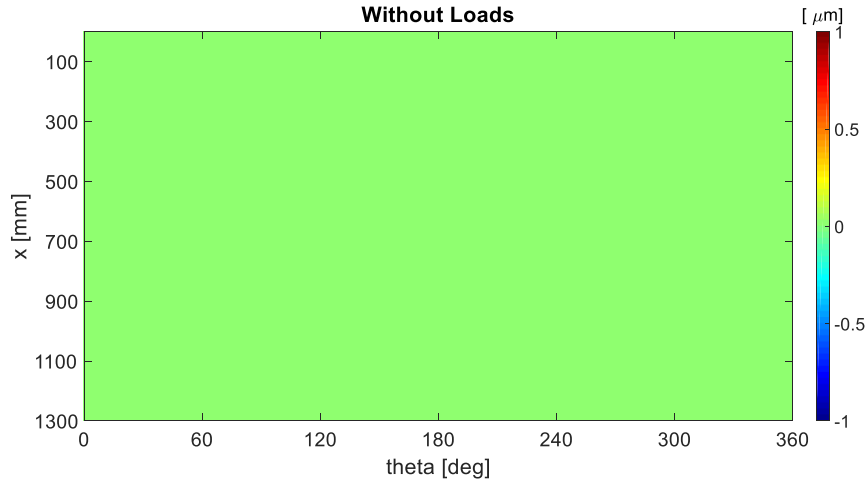


Figure 5.9: Air gap displacement: no loads applied

As expected, the whole plot in Figure 5.9 is green it means that the air gap's displacement during this first simulation is 0 mm in every nodes of the mesh, that's make sense because there are no loads.

Figure 5.10 shows the results for the simulation with only the gravity. On the right side there is the graphic deflection of the lateral section of the whole system, the maximum displacement is at the end of the hub and it is 5.645 mm of magnitude. Always on the right side there is the zoom of the top part and bottom part of the generator, it possible to see that in the bottom part of the generator ($x = 1300\text{ mm}$ and $\vartheta = 90^\circ$) there is a decrease of the air gap's size and in the top part of the generator ($x = 1300\text{ mm}$ and $\vartheta = 270^\circ$) there is an increase of the air gap's size. On the left side there is the plot of the air gap's displacement, it has a negative value (decrease of clearance) close to $\vartheta = 90^\circ$ and a positive value (increase of clearance) close to $\vartheta = 270^\circ$. The air gap's movement is in a range between $-327\text{ }\mu\text{m}$ and $294\text{ }\mu\text{m}$.

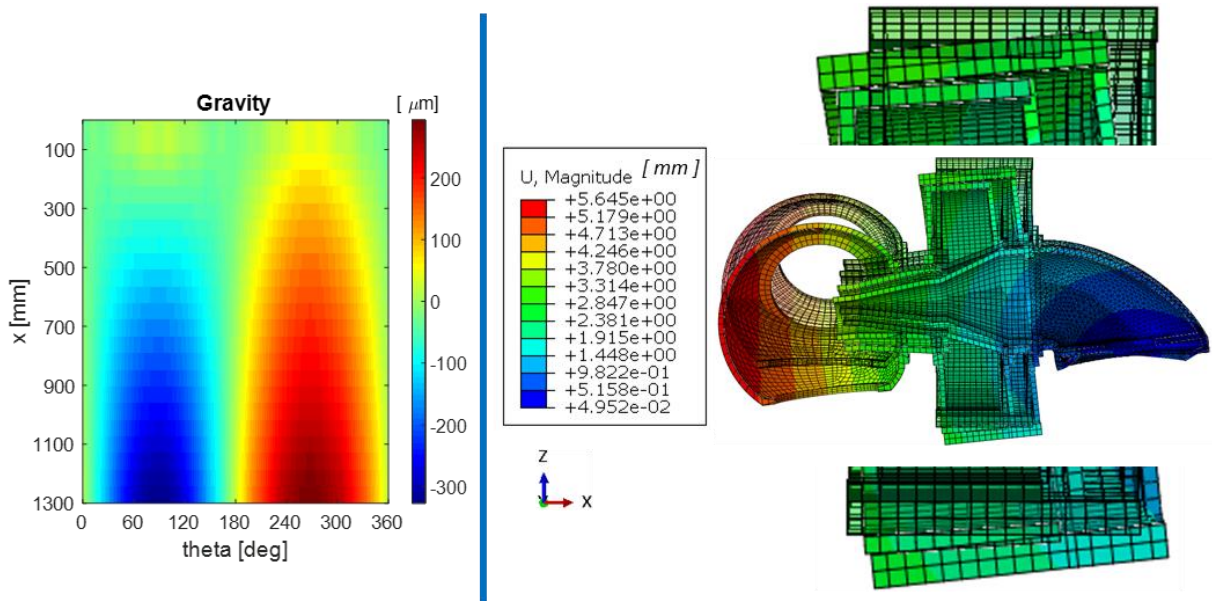


Figure 5.10: Air gap displacement: Gravity

Figure 5.11 shows the results for the simulation with the influence of gravity and the blades' weight. The right side and the left side are the same of Figure 5.10. For $x = 1300 \text{ mm}$ and $\vartheta = 90^\circ$ there is a positive value in the plot, it means that the zoom of the lateral section of the bottom part of the generator must show an increase of size, as it does. For $x = 1300 \text{ mm}$ and $\vartheta = 270^\circ$ there is a negative value in the plot, it means that the zoom of the latera section of the bottom part of the generator must show a decrease of size, as it does. The air gap's movement is in a range between $-440 \mu\text{m}$ and $330 \mu\text{m}$. The maximum displacement is at the end of the hub and it is 14.20 mm of magnitude.

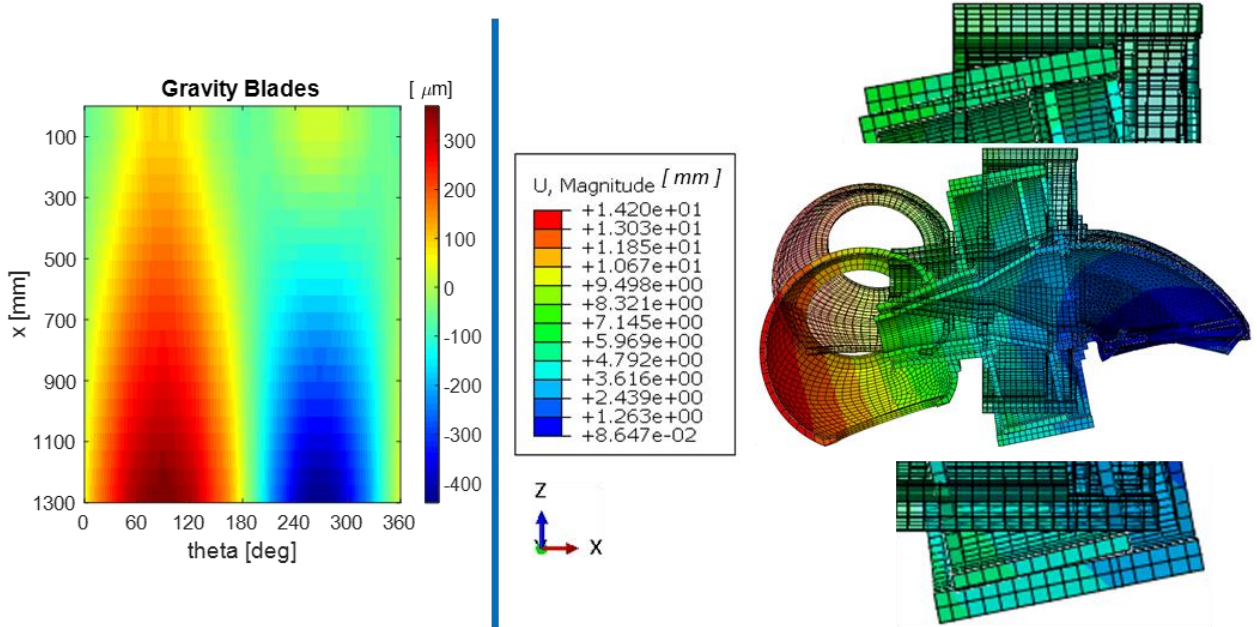


Figure 5.11: Air gap displacement: Gravity Blades weight

Figure 5.12 Figure 5.13 Figure 5.14 Figure 5.15 and Figure 5.16 show the results of the simulations with the gravity, the weight of the blades and the magnetic pull with, respectively 1-3-5-10-20 slices. The air gap's displacement is always in a range between $-534 \mu\text{m}$ and $462 \mu\text{m}$. The maximum displacement is always at the end of the hub and it is close to $14.3(\pm 2) \text{ mm}$ of magnitude.

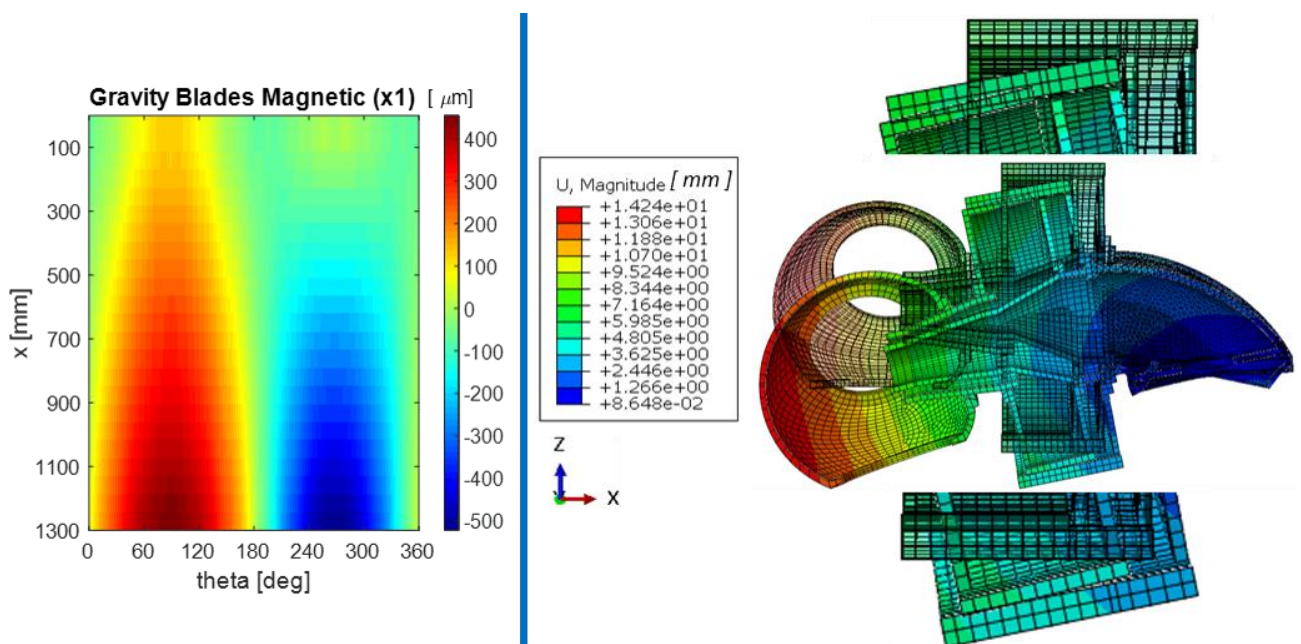


Figure 5.12: Air gap displacement: Gravity Blades weight Magnetic pull 1 slice

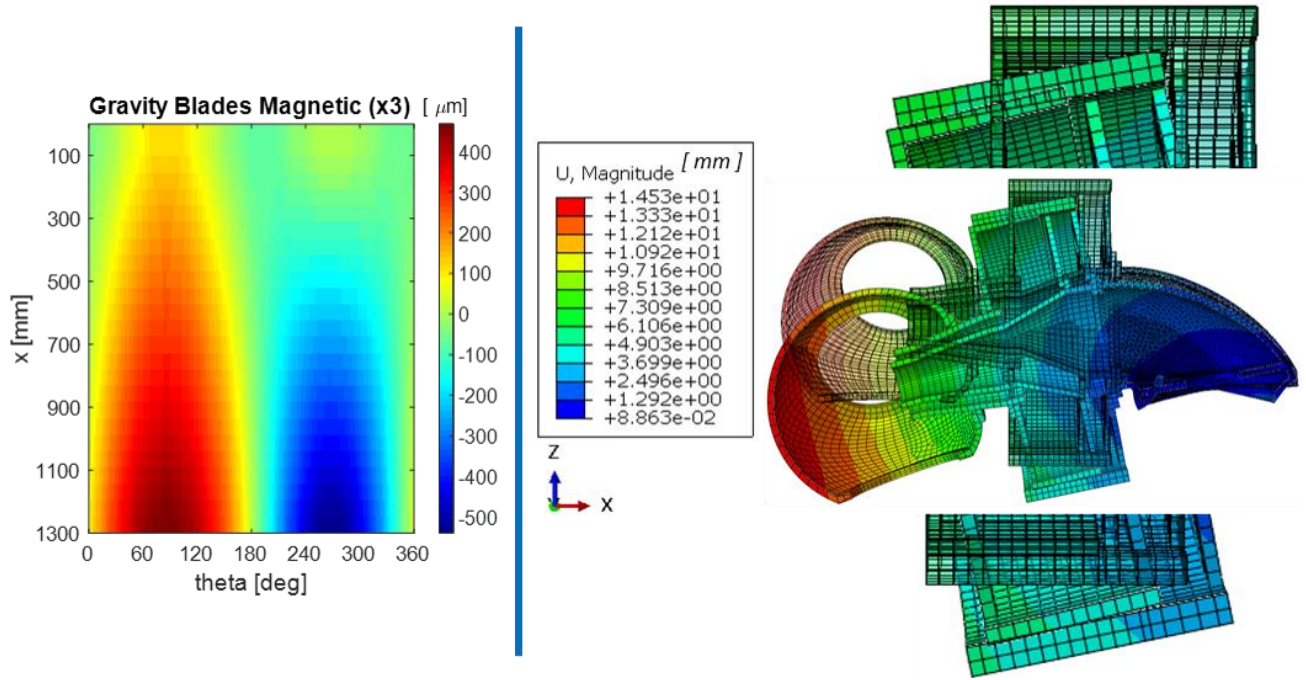


Figure 5.13: Air gap displacement: Gravity Blades weight Magnetic pull 3 slices

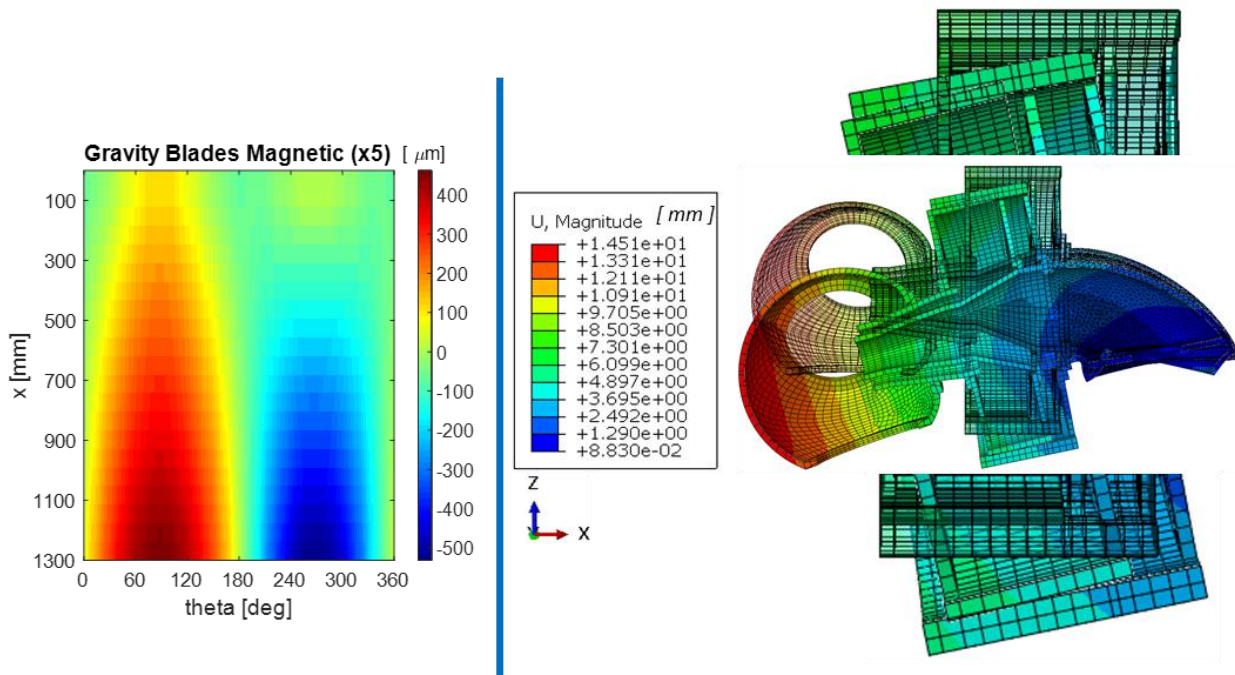


Figure 5.14: Air gap displacement: Gravity Blades weight Magnetic pull 5 slice

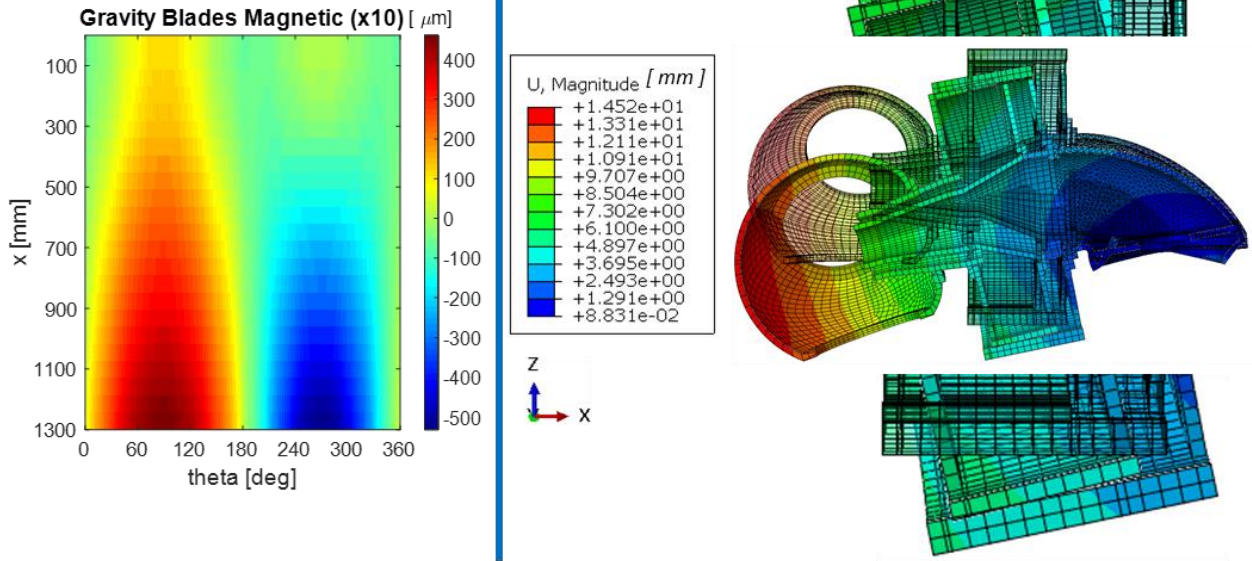


Figure 5.15: Air gap displacement: Gravity Blades weight Magnetic pull 10 slices

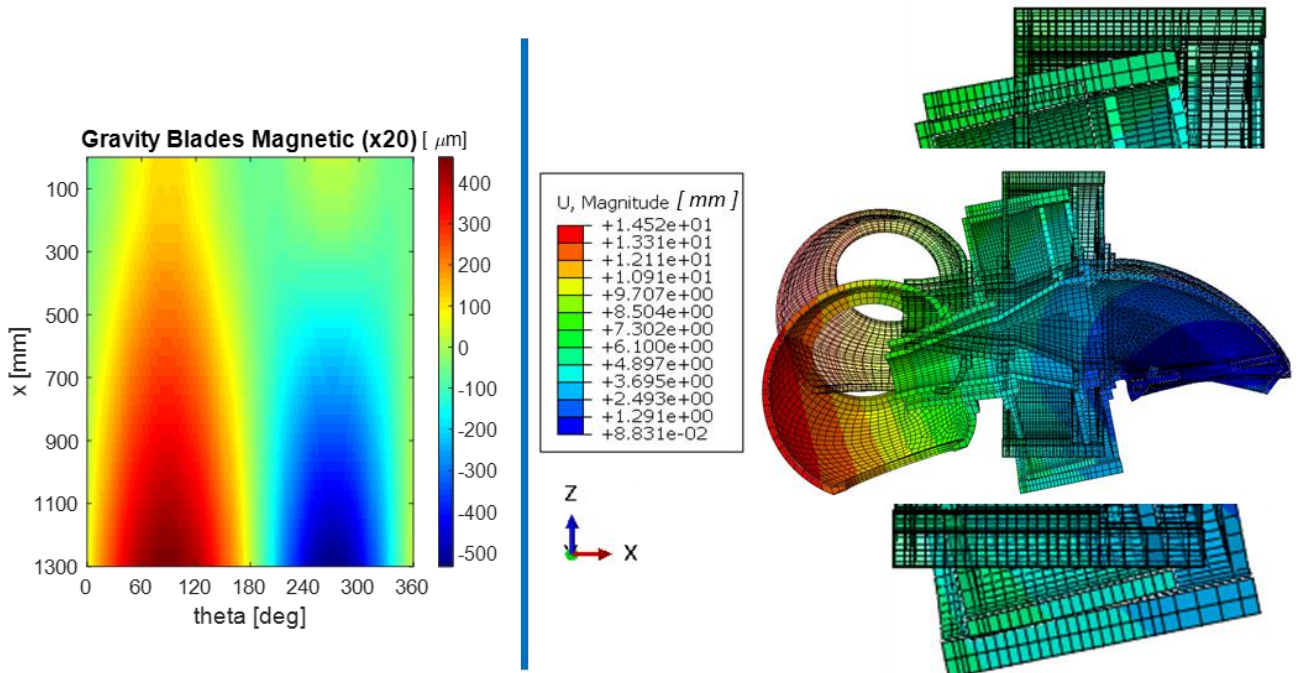


Figure 5.16: Air gap displacement: Gravity Blades weight Magnetic pull 20 slices

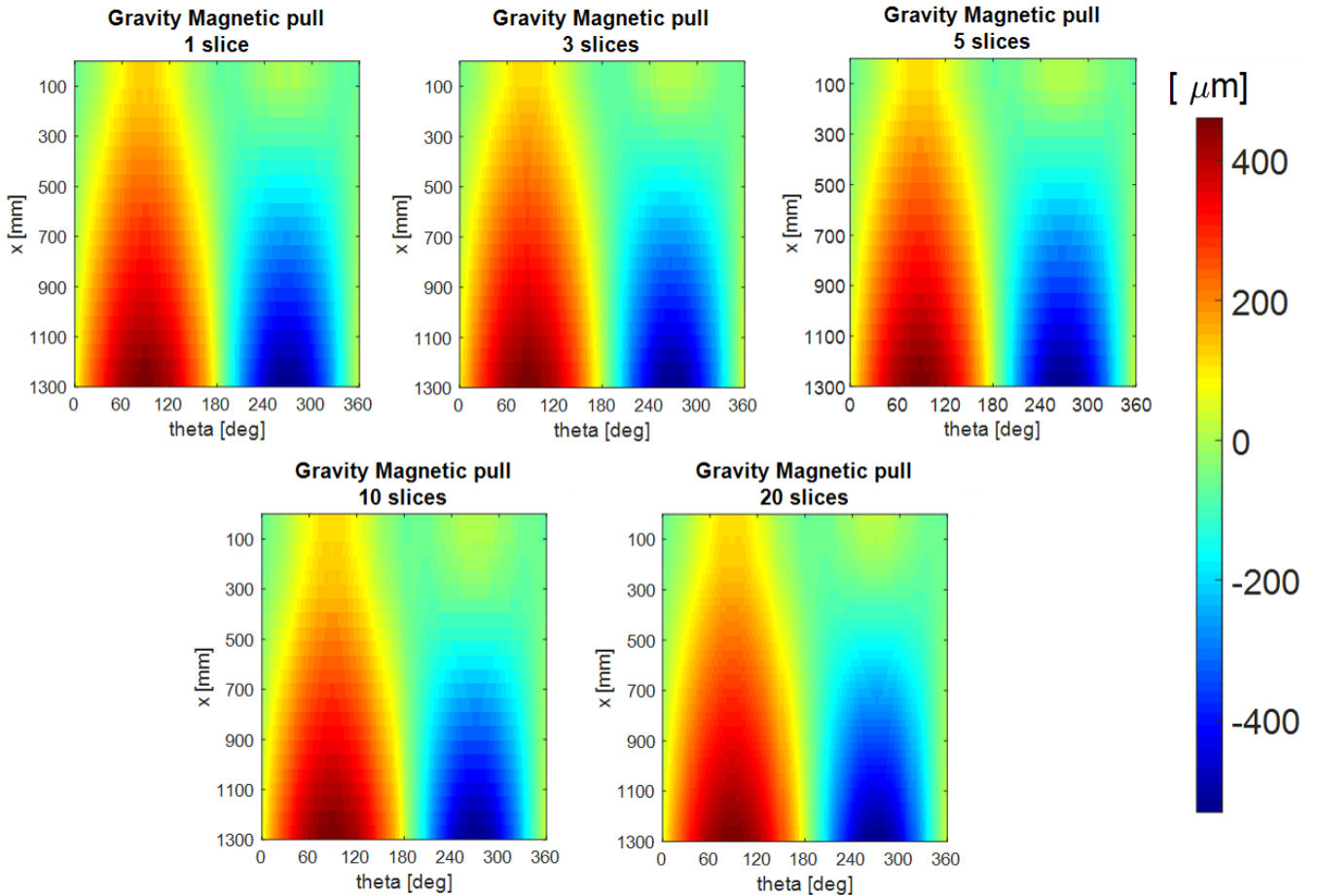


Figure 5.17: Airgap displacement: Comparison between the impact of the number of the slices

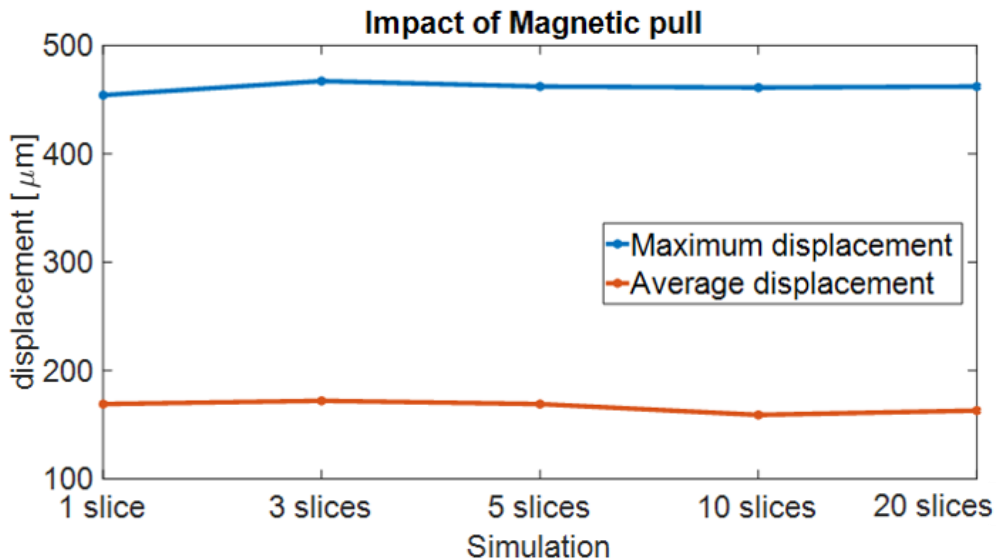


Figure 5.18: Maximum and Average displacement for magnetic pull split up in different number of slices

Figure 5.17 and Figure 5.18 show how the air gap clearance change if the magnetic pull is split in more slice than 1. The change of the maximum increase size between each simulation is lower than 3% as the average displacement and looking Figure 5.17 is evident that the displacement distribution is always the same. Hence, for the static simulation in this case one slice is enough to model the magnetic pull.

In order to have a static condition when the generator torque and the wind loads are added at the model all loads are applied in only one reference point that is constrained with the external surfaces of the hub 's holes

and the rotation around x of the wire that joins the stator and rotor surfaces is locked. A torque equal and opposite to the generator torque is applied on a reference point constrained with the external rotor surface. Figure 5.19 shows the boundary condition that are used for the simulation with the torque around x axis.

Figure 5.17 show the results for the simulations with the impact of the gravity, the blades and the magnetic pull split up in 1-3-5-10-20 slices. The difference between every simulation is always lower the 1%, and the displacement distribution is always the same, so for this kind of generator and for the static simulation 1 slices in enough to model the magnetic pull.

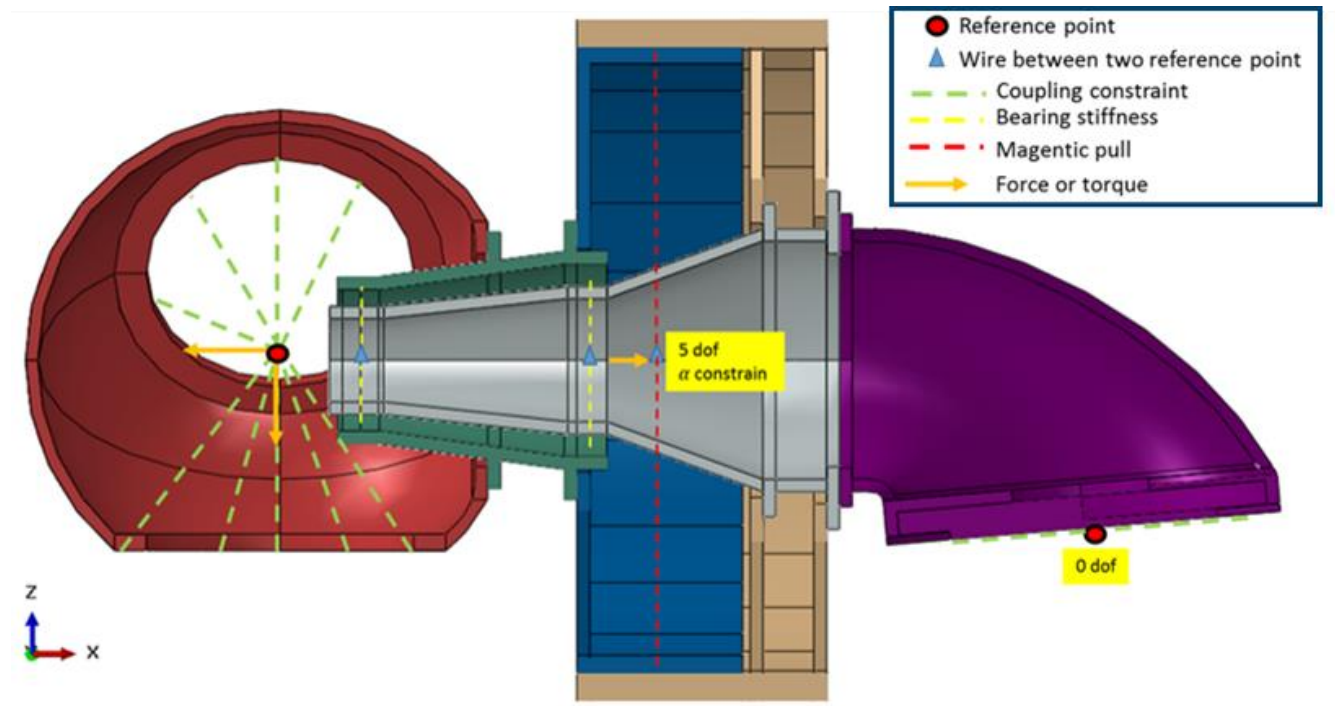


Figure 5.19: Boundary conditions for the simulation with torque around x

In the follow graphs in the gravity is also included the impact of the blades

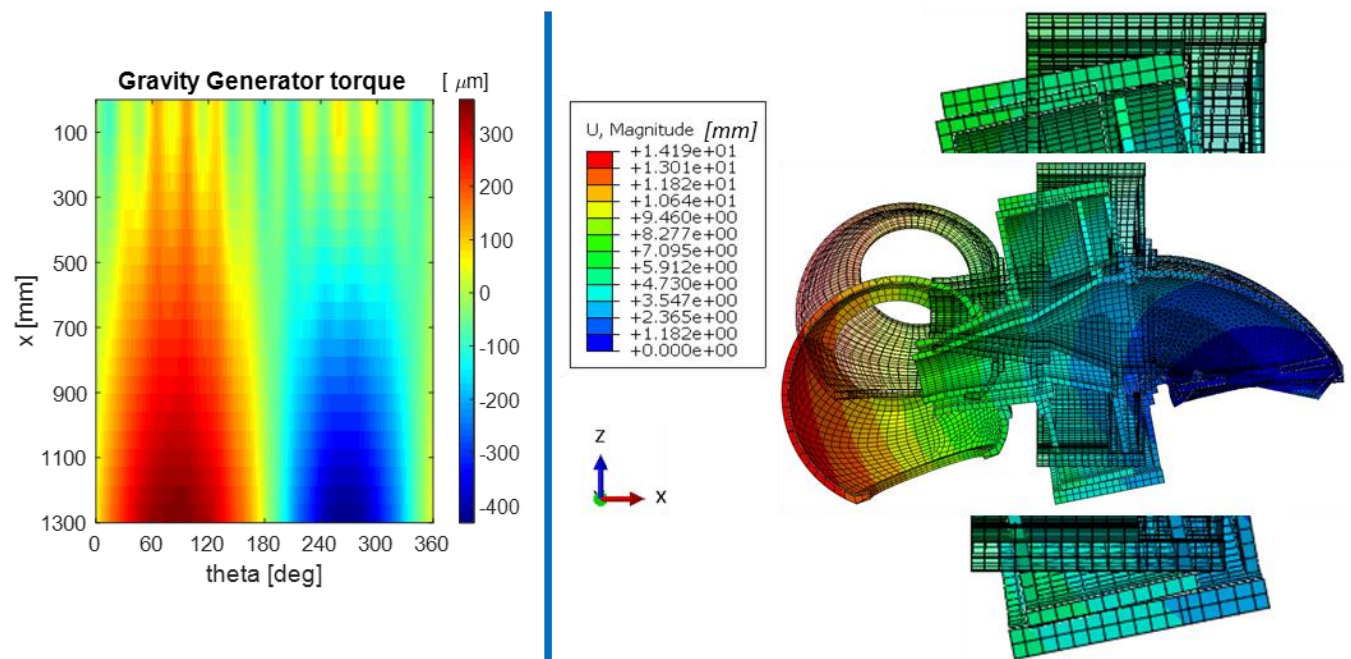


Figure 5.20: Air gap displacement: Gravity Blades weight Generator torque

Figure 5.20 shows the impact of the generator torque combined to the gravity on the air gap. The maximum decrease is $-432\mu\text{m}$ and the maximum increase is $363\mu\text{m}$. The global impact of the generator torque is lower than the impact of the magnetic pull but looking Figure 5.20 in the region from $x = 0\text{ mm}$ to $x = 150\mu\text{m}$ it is evident that the rotor's arms are more stressed.

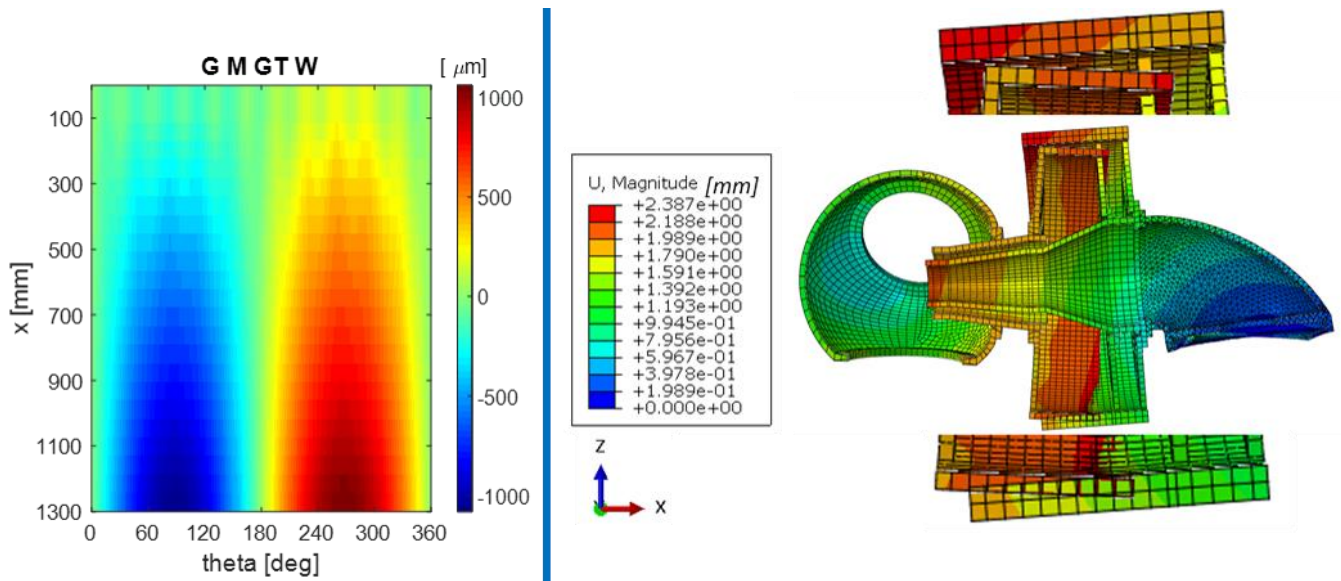


Figure 5.21: Air gap displacement: Gravity Blades weight Magnetic pull Generator torque Wind

- G** is gravity and weight blades
- M** is the magnetic
- GT** is the generator torque
- W** is the wind loads

Figure 5.21 shows the impact of all loads, the air gap displacement range is from $-1081\mu\text{m}$ to $1062\mu\text{m}$. In the region plot from $x = 0\text{ mm}$ to $x = 300\mu\text{m}$ there is an harmonic behaviour due to the deflection of the rotor's arms due to the generator torque. The impact of the bending moment due to the wind is evident, the maximum decrease is at the bottom of the generator and the maximum increase is at the top of the generator, in the other simulations their position are revers. The hub moves up of 1.3 mm , contrary without the impact of the wind the hub moves down of 14 mm .

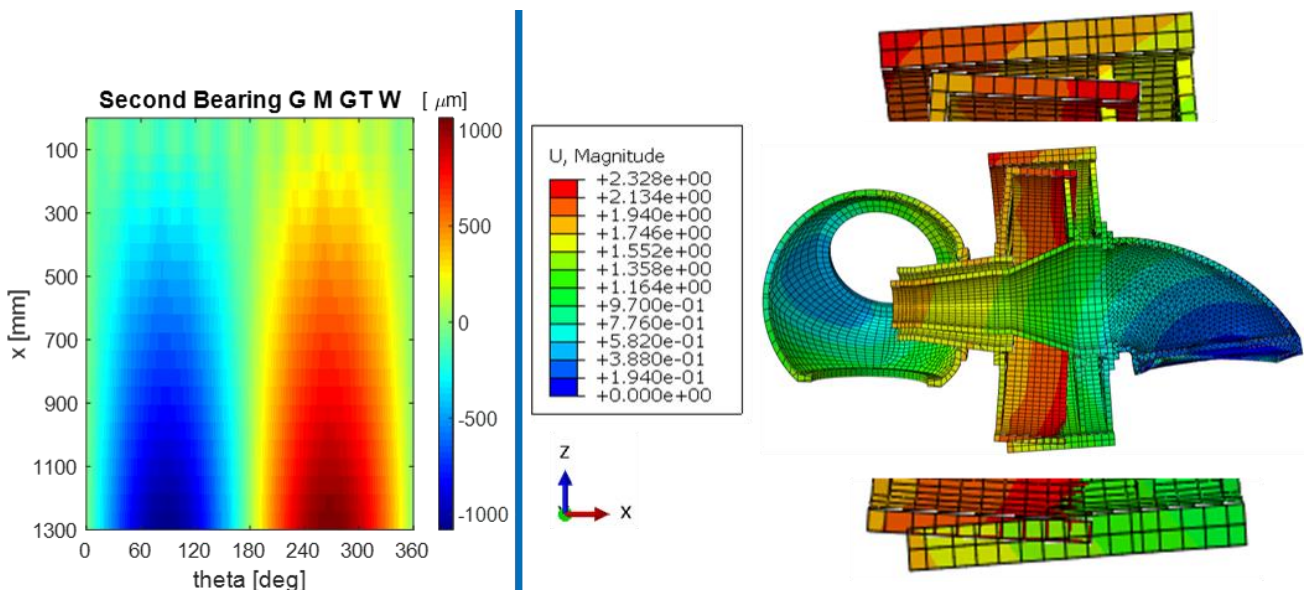


Figure 5.22: Second bearings configurations: Gravity Magnetic pull Generator torque Wind

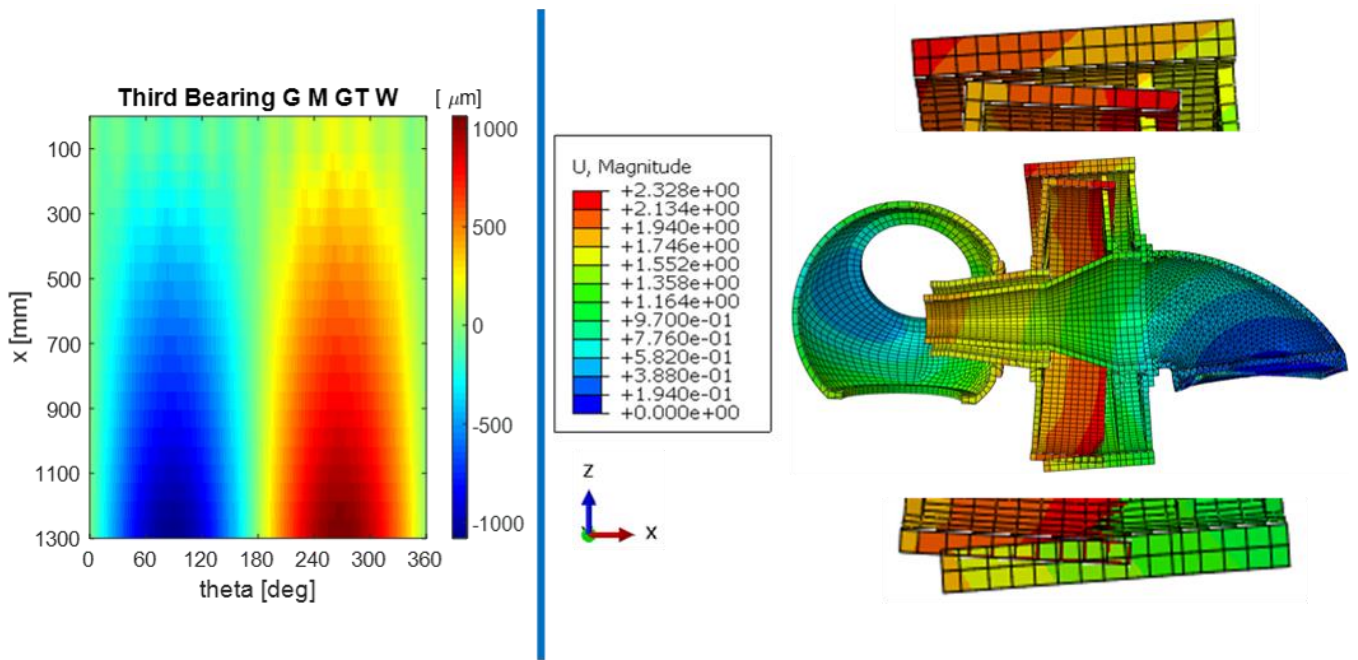


Figure 5.23: Third bearings configurations: Gravity Magnetic pull Generator torque Wind

Figure 5.22 and Figure 5.23 show the results come from the simulations with the second and third bearing configurations. The difference between the simulation with the first configuration to the other configuration is always lower than 5% and the displacement distribution is the same, so the first bearing configurations has been selected to make the comparison with the other loads case.

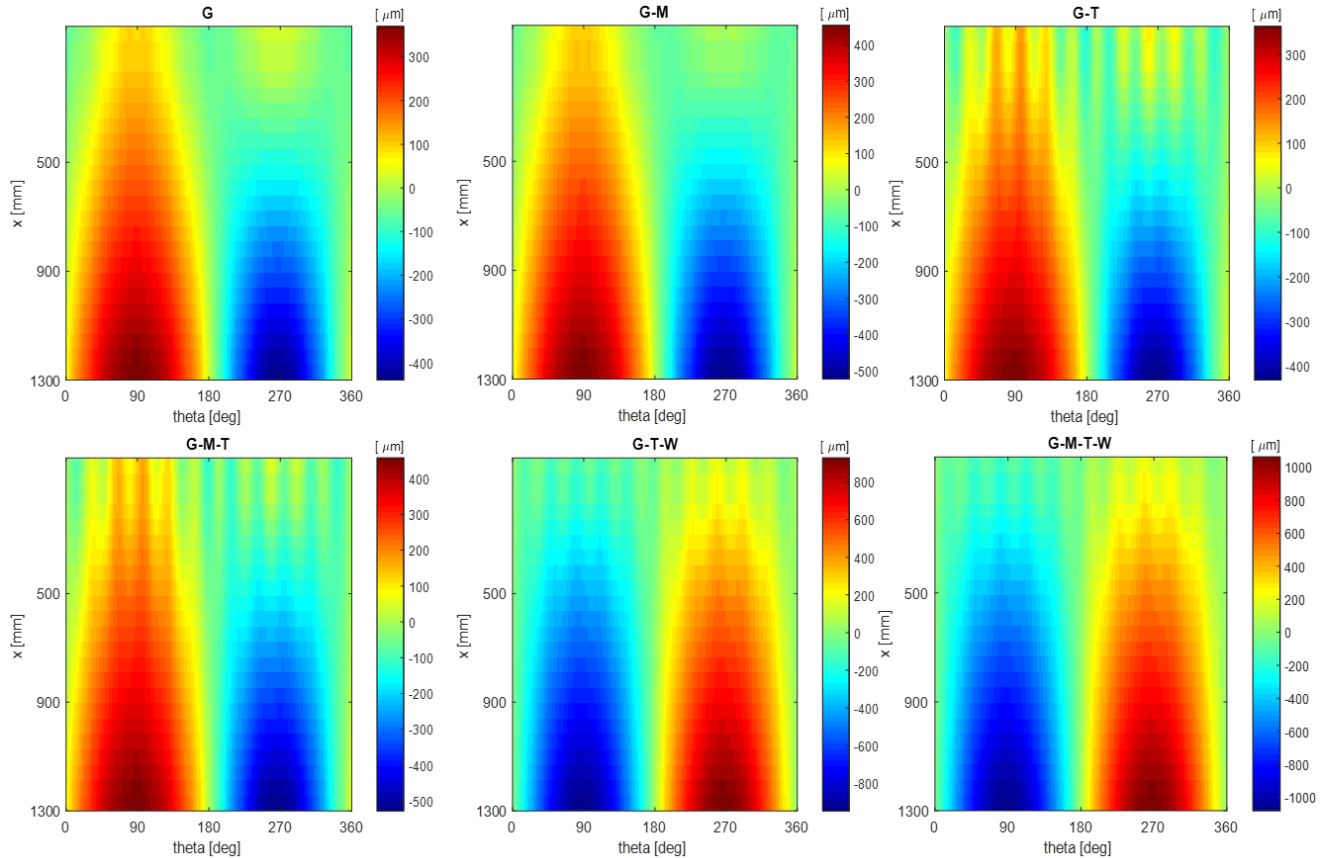


Figure 5.24: Airgap displacement: Comparison between impact of different load set

- G** means gravity and blades
- M** means magnetic pull
- T** means generator torque
- W** means wind loads

Figure 5.24 compares all simulation, the maximum absolute value with only the gravity is $440 \mu m$ and its value doubles when all loads are added. The effect of the bending moments due to the wind change the distribution of the displacement so the position of the maximum decrease and increase are reversed between the first simulation to the last simulation and the generator torque change the displacement distribution by the deflections of the rotor arms

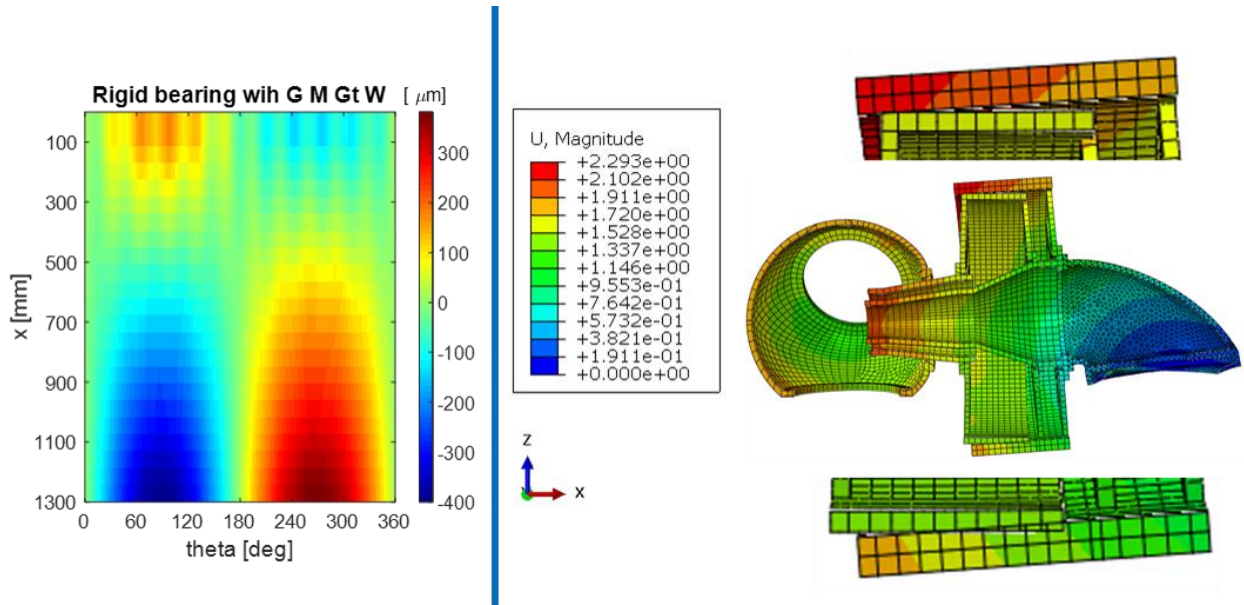


Figure 5.25: Rigid bearings air gap displacement: Gravity Blades weight Magnetic pull Generator torque Wind

Figure 5.25 shows the impact of the bearings in the generator. The displacement range goes to $-400 \mu m$ until $382 \mu m$. Looking at Figure 5.21 and Figure 5.25 it appears that more than half of the air gap displacement is due to the elasticity of the bearings, the average displacement with rigid bearing is $111 \mu m$ (2,2%) and with normal bearings is $387 \mu m$ (7,4%).

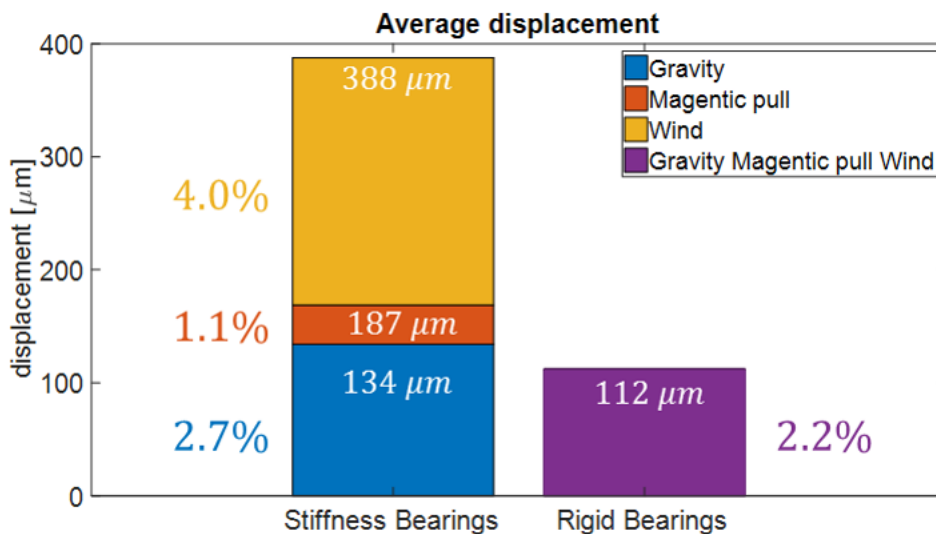


Figure 5.26: Average displacement: real bearing VS rigid bearing

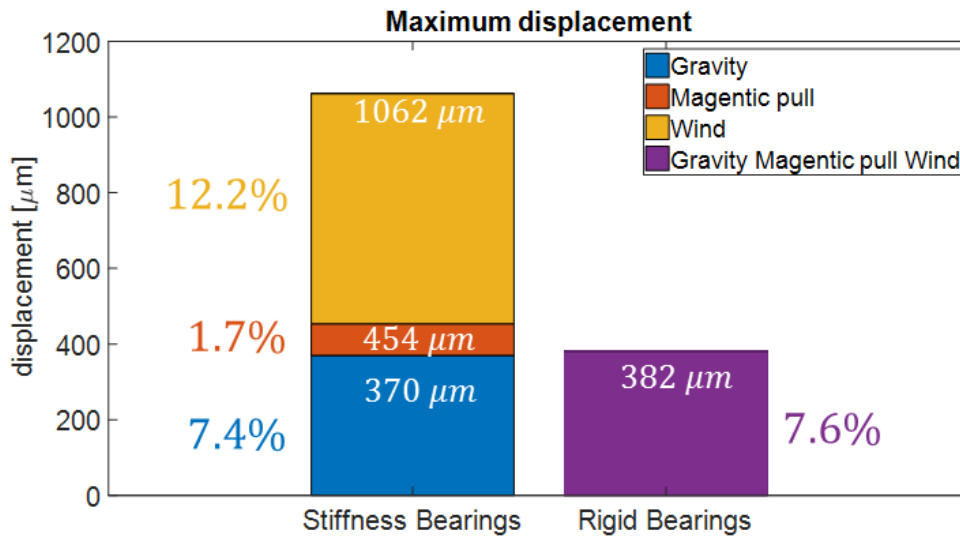


Figure 5.27: Average displacement: real bearing VS rigid bearing

1 means real bearings

2 means rigid bearings

Figure 5.26 and Figure 5.27 show respectively the comparison between the real bearings to the rigid bearing. In the real bearings configuration, the biggest impact on the airgap size is due to the wind loads, the 3.3% of the average displacement and 12.1% of the maximum displacement are due to it, the impact of the gravity is 2.7% on the average displacement and 7.4% on the maximum displacement, the lower size deflection is due to the magnetic pull, 0.7% on the average displacement and 1.7% on the maximum displacement. In the configuration with the rigid bearings the average displacement is 2.2%, 5% lower than with a real bearings, and the maximum displacement is 7.6%, 13.6% lower than with the real bearings. Hence the highest impact is due to the bearing stiffness.

5.1.2 Comparison results FEM to MB

The air gap in MBS has been analysed with two coupling of marker, the first coupling to analyse the top part of the generator and the other coupling to examine the bottom part of the generator. Two coupling of marker have been chosen because the results from FEM show that the displacement between top part and bottom part of the generator is not symmetric, so one marker coupling is not enough to compare the air gap behaviour. Figure 5.28 shows how the air gap displacement in SIMPACK has been calculated for the generator’s top part. The distance between stator and rotor has been measured in the middle of the air gap length and the clearance at $x = 0$ and $x = 1\,300\text{ mm}$ has been calculated as

$$\delta_{(x=0)} = \Delta z - 650 \tan(\beta) \tag{Equation 5.1}$$

$$\delta_{(x=1300)} = \Delta z + 650 \tan(\beta) \tag{Equation 5.2}$$

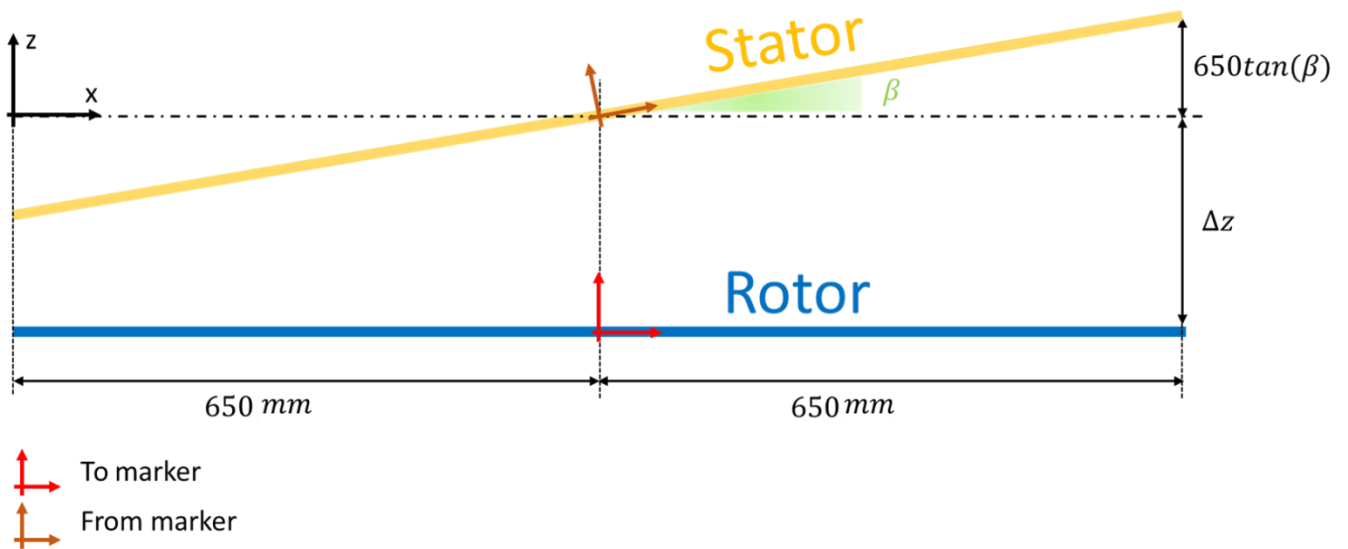


Figure 5.28: MBS air gap displacement sketch of the top generator’s top part

The displacement distribution is made with a linear interpolation between the displacement at $x = 0$ to $x = 1300\text{mm}$

The first comparison between MBS to FEM has been for the analyse only with the impact of the gravity, the blades weight and the magnetic pull. Figure 5.29 shows result with only 20 eigenmode active in Simpack without the IRM frequency. The MBS model is stiffer than the FEM model the displacement trend is the same but the difference between the two simulation is too high, 20 eigenmode are not enough. Figure 5.30 shows what happen is the number of eigenmode is increase until 40, the difference between the two models is still bigger than 10% so also 40 eigenmode are not enough. Also, when the activated eigenmode are 50 the gap between the MBS and FEM is too big, Figure 5.31. In order to have a good matching 80 eigenmode active are needed, Figure 5.32 shows the biggest percentual variation is at $x = 0\text{ mm}$ where the displacement is smallest but for $x = 1300\text{ mm}$ the matching coefficient is bigger than 90%. Looking the solid lines (they are regard to the FEM model) in Figure 5.29, Figure 5.30, Figure 5.31 and Figure 5.32 the linear behaviour of the displacement is clear but for $x = 0\text{ mm}$ and $x = 1300\text{ mm}$ there is an increase of stiffness due to the arms that broke the liner behaviour and decrease the slop, it is not possible to see this effect in Simpack because the displacement distribution has made as a linear interpolation between two points

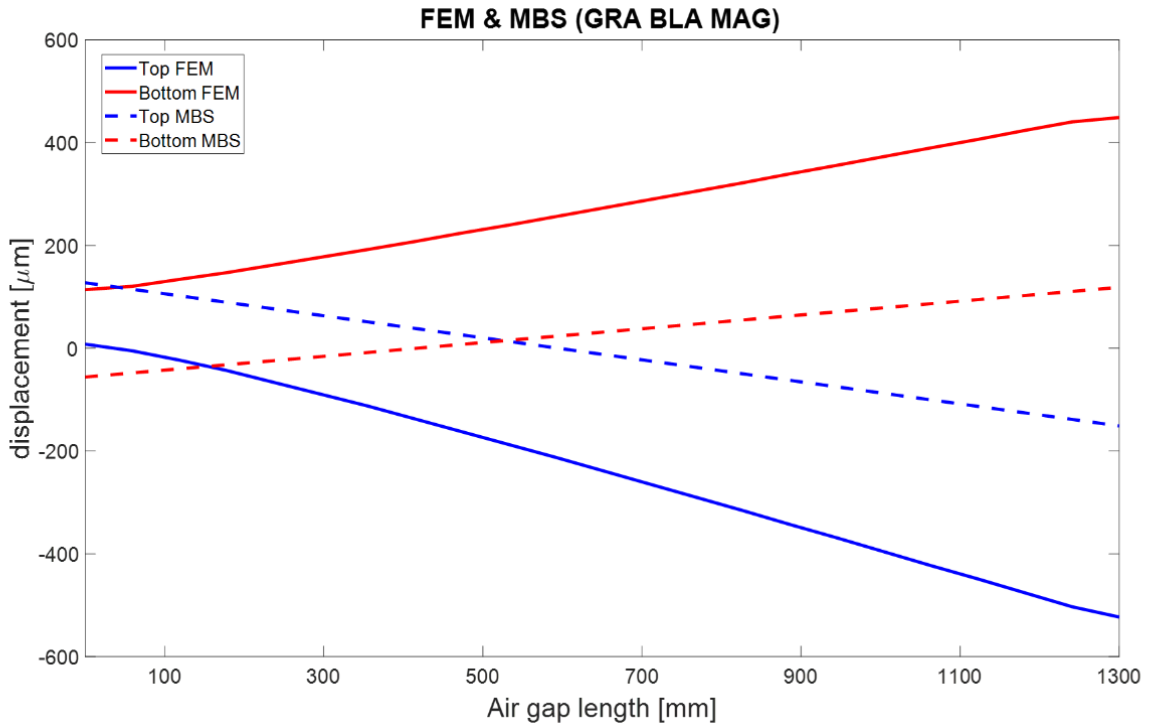


Figure 5.29: 20 eigen mode active

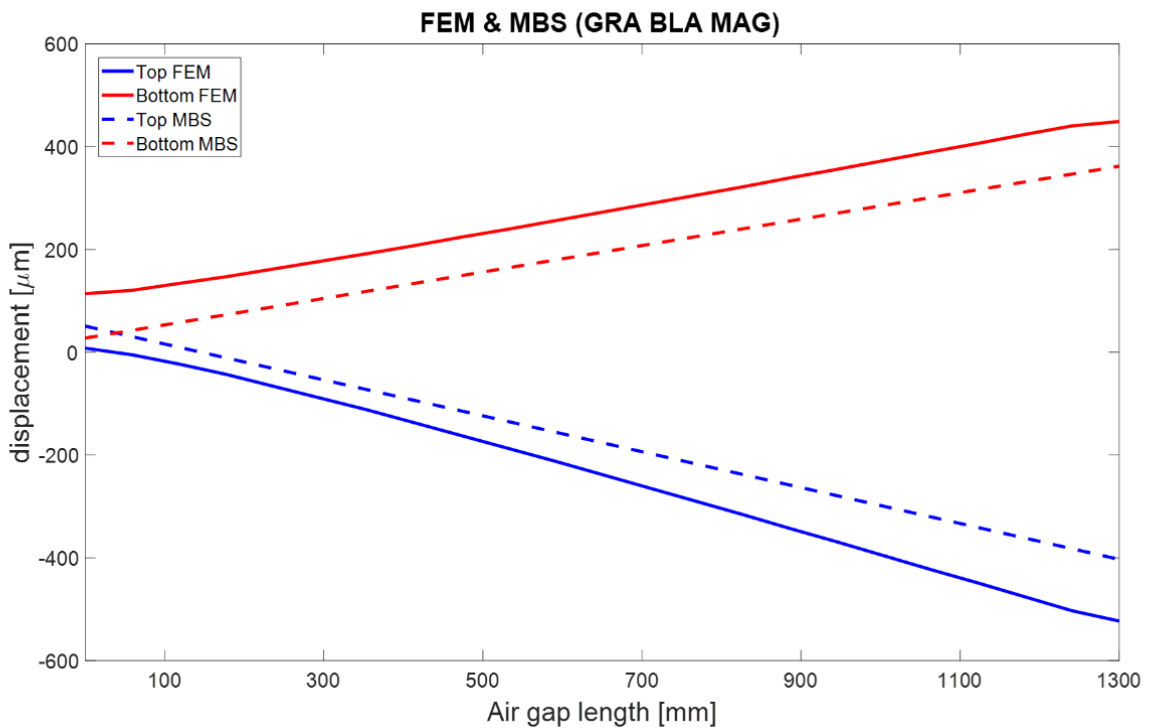


Figure 5.30: 40 eigen mode active

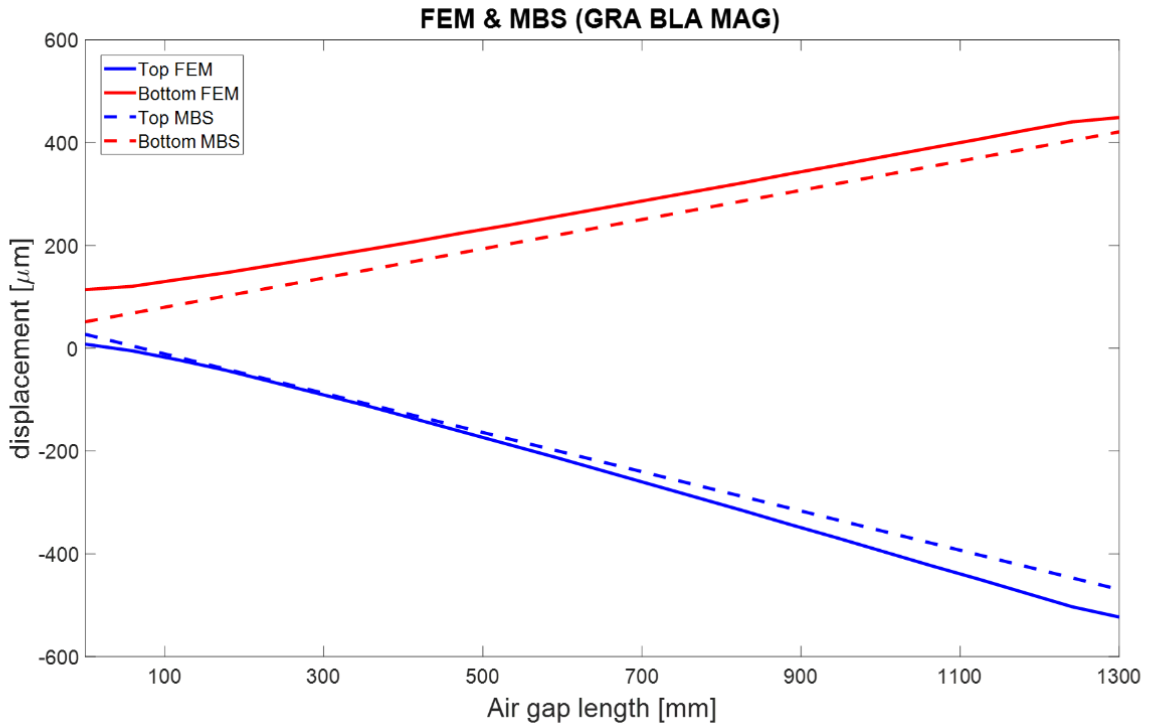


Figure 5.31: 50 eigen mode active

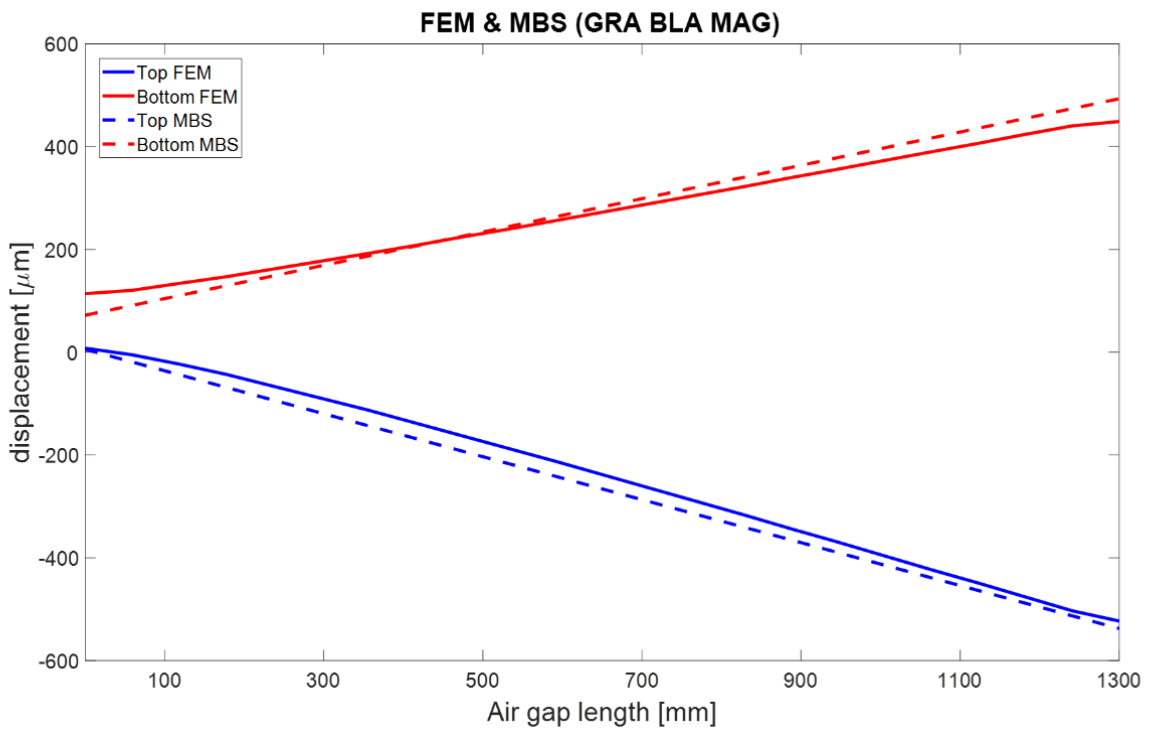


Figure 5.32: 80 eigen mode active

Figure 5.33 shows the result of the comparison when also the wind loads are added. Following the previously results 80 eigenmodes have been directly chosen because. As in the last case the matching at $x = 1300 \text{ mm}$, where there is the biggest impact is bigger than 90 %.

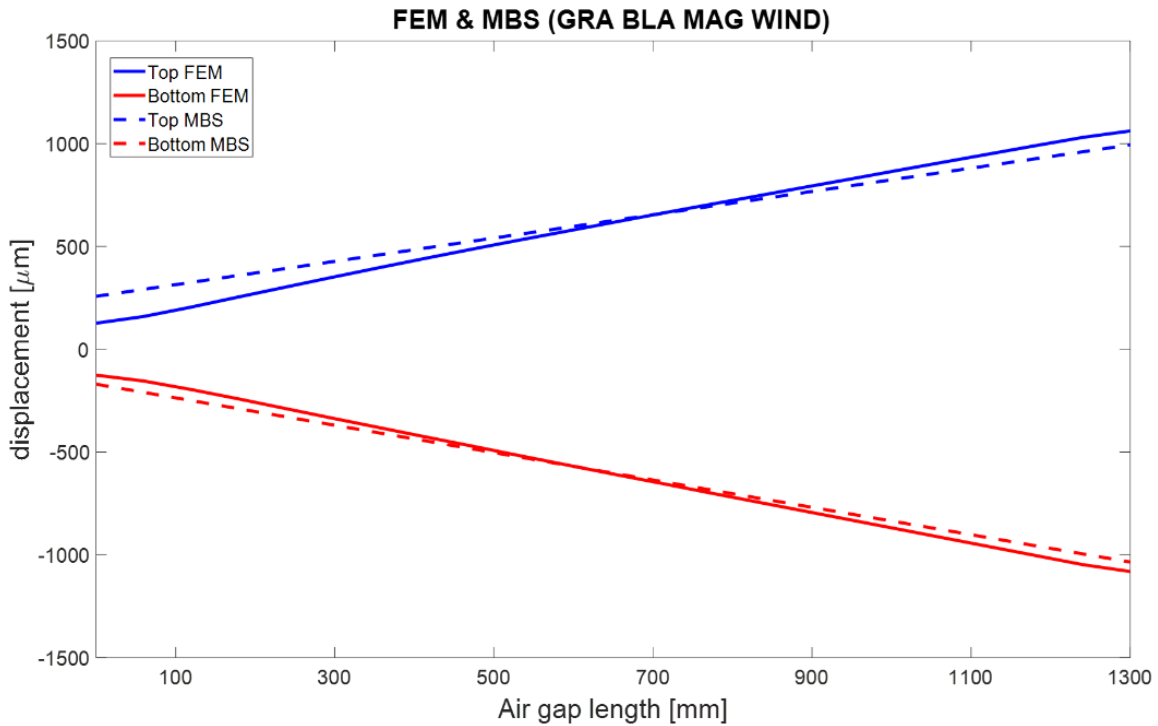


Figure 5.33: 80 eigen mode active

In order to see how many eigenmode and the value of the cut IRM frequency needed to do the MBS simulation the convergence analysis has been done. Figure 5.34 shows the result of the simulation, the minimum air gap size in MBS is always lower than in FEM, it is due to the number of degree of freedom in ABAQUS and in Simpack, ABAQUS use a very high number of nodes to make the constrain contrary Simpack uses only one marker to make the constraint, so the structure in Simpack is stiffer than the structure in ABAQUS.

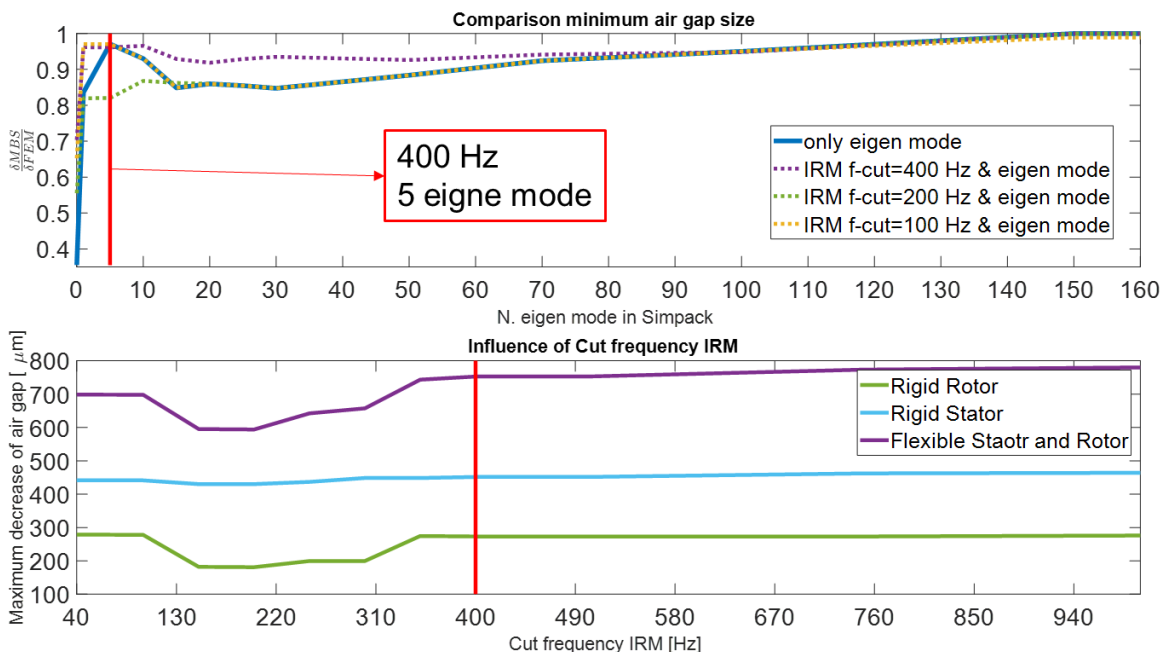


Figure 5.34: Convergence analysis for the cut IRM frequency and for the number of eigen mode

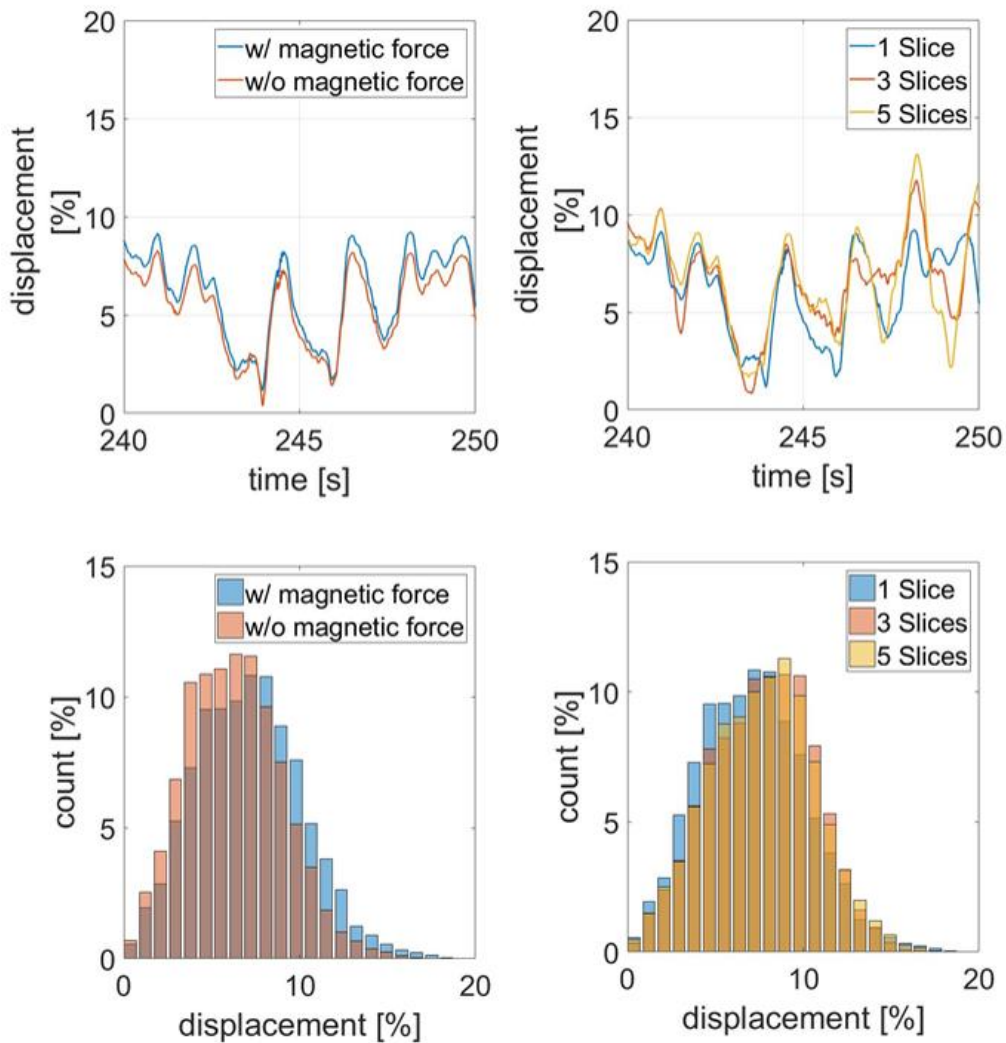


Figure 5.35: Air gap displacement from MBS simulation

Figure 5.35 shows the results from the MBS simulation with the wind speed equal to 12 m/s and the turbulence class A, with and without the magnetic pull. The percentage displacement in the middle of the air gap length for a window out of 10 s is shown at the top of the figure and at below it there are the histogram of the summarized displacement over 600 s (600 s are needed due to the norm), the displacement is always in a range between 0% to 20% . Contrary to the FEM analysis, during the MBS analysis one slice is not enough to have the convergence displacement but three slices are needed. The percentual displacement is in a range between 0 to 20% , it confirms the FEM analysis, that are made for the worst loads case.

5.2 Campbell diagram

Figure 5.36 shows the Campbell diagram for the first 30 natural frequency. The external excitation $1p\ 3p\ 6p\ 9p\ 12p$ from the wind and the excitation $80p$ from the bearings have been drawn in the graph, they are the black lines. The nominal speed is 12 rpm and the operating speed range is between 7.8 rpm to 13 rpm , the yellow rectangle in the graph, hence the resonance could happen only for the frequency lower to the 12^{th} mode (3.78 Hz).

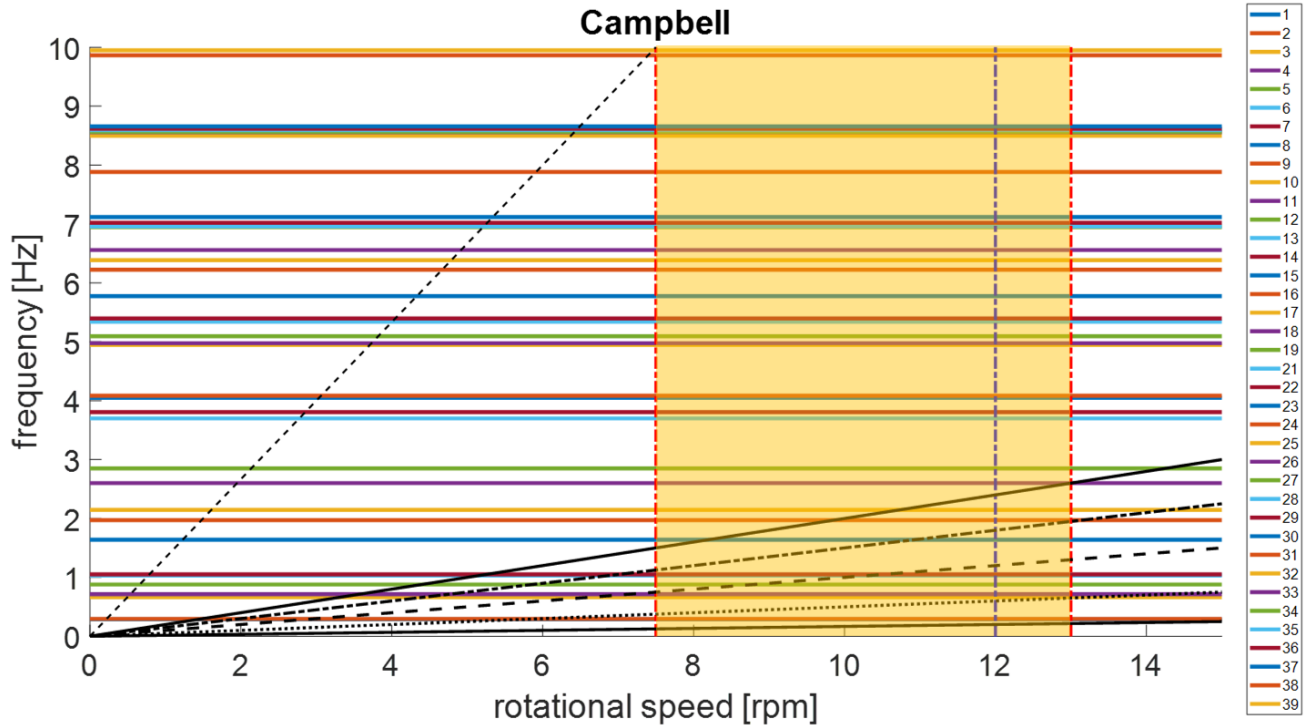


Figure 5.36: Campbell diagram for the eigenfrequency until 39

Figure 5.37 shows the Campbell diagram for the frequency lower to 3 Hz, there are 6 possible resonance points, the red circle, but there is no resonance point at the nominal speed and there is no resonance point for the external excitation $3p$, which is the most dangerous excitation for the system due to its very high energy.

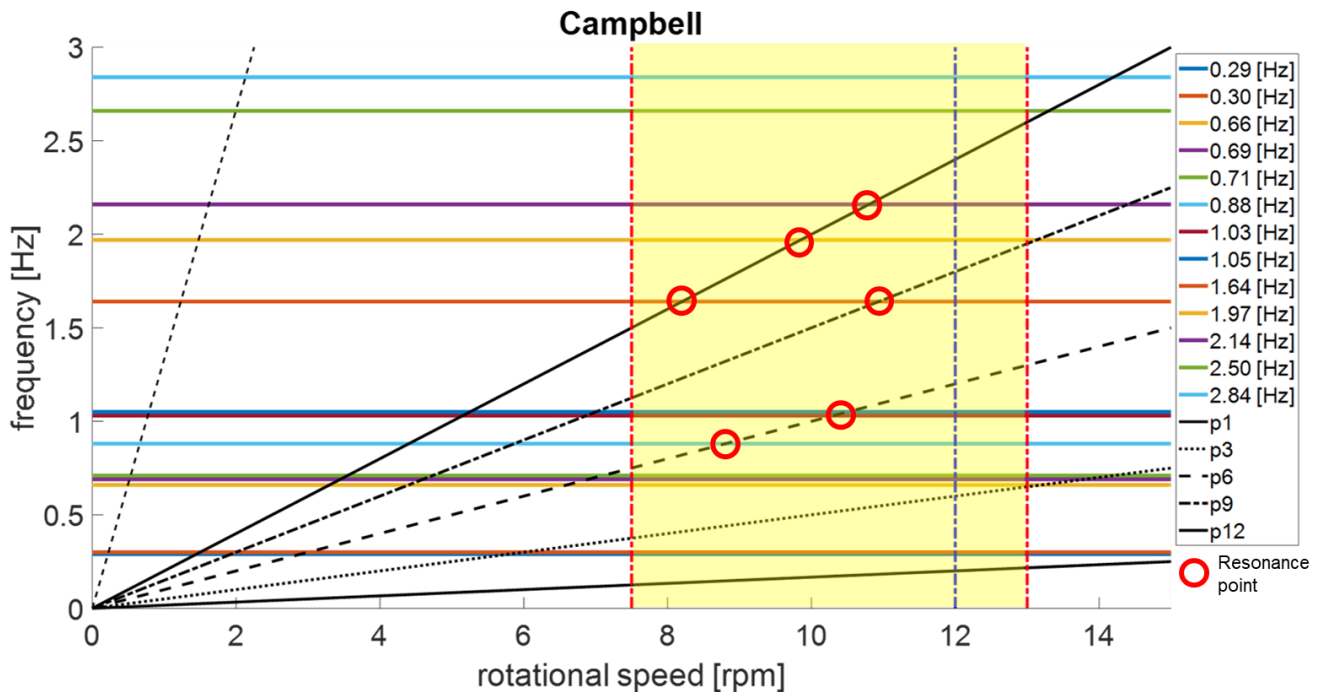


Figure 5.37Campbel diagram for natural frequency lower to 3 Hz

mode	Description	[Hz]
1 st	1 st Tower force-aft swing	0.29
2 nd	1 st Tower lateral swing	0.30
3 rd	1 st Collective blade flap	0.66
4 th	1 st Collective blade flap	0.69
5 th	1 st Asymmetric blade flap in bending axis	0.71
6 th	1 st Symmetric blade flap in bending axis	0.88
7 th	1 st Symmetric blade edgewise mode	1.03
8 th	1 st Asymmetric blade edgewise mode	1.05
9 th	2 nd Asymmetric blade flap in bending axis	1.64
10 th	2 nd Symmetric blade flap in bending axis	1.97
11 th	2 nd Symmetric blade flap bending axis	2.14
12 th	2 nd Symmetric blade flap bending axis	2.66
13 th	1 st Rotor edgewise-drive train mode	2.84

Table 5.2: Description of eigenmode

5.3 Optimization

In order to reduce the air gap's deflection another concept of inner rotor generator as designed and analysed. In Figure 5.38 is showed a lateral section of the optimization model.

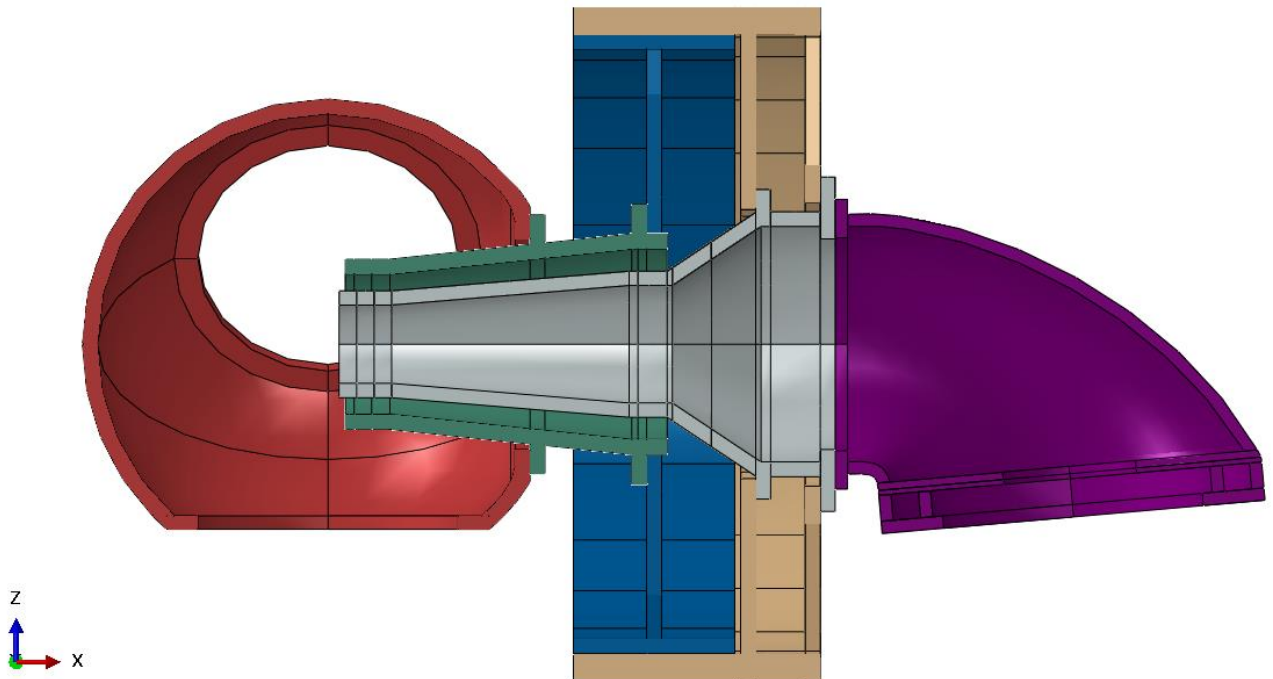


Figure 5.38: Lateral section of the optimization model

The thickness of all components increases from 100 mm to 120 mm, the machine frame has one more component along where is in touch with the tower, the arms of the rotor are in the middle of the air gap and

the two sets of stator's arms are shifted. All these changes are made to design a stiffer model and decrease the displacement of the whole generator into the middle of air gap. The mass of the new model is 190,61 ton before was 170.2 ton, there is an increment of 11.7%.

Also, for the optimization model the first simulation that has been done is whit no loads for to see if all components are in the right position. The results are showed in Figure 5.39.

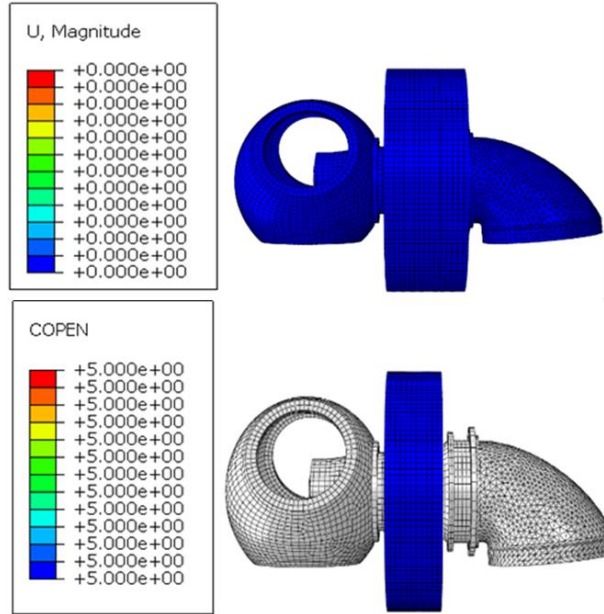


Figure 5.39: Optimization model analysis without loads

The result says that there is no displacement and that the air gap's clearance is 5 mm, as it should be. So, the model is correct.

Figure 5.40 shows the result for the simulation with all loads, the air gap displacement is in the range between $-420 \mu m$ to $410 \mu m$. the influent of the blades is evident in the middle of the plot where there is an harmonic behaviour an like in the model not optimization the maximum decrease is at the top of the generator and the maximum increase is at the bottom of the generator.

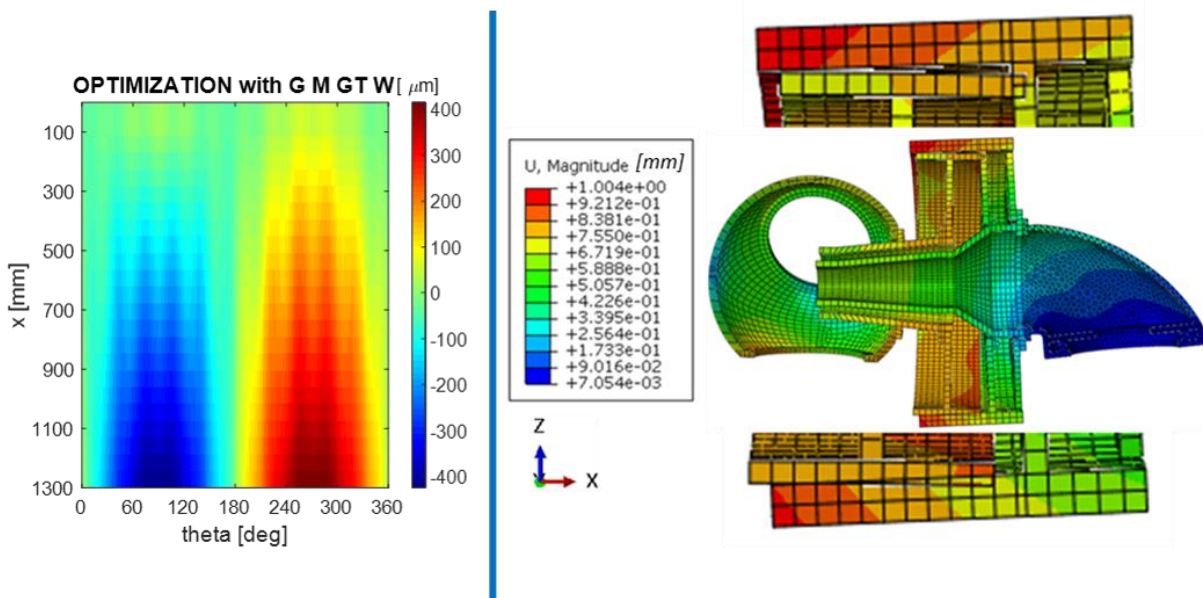


Figure 5.40: Optimization model air gap displacement: Gravity weight Generator torque Magnetic pull Wind

Figure 5.41 shows that there is an improve in the average displacement equal to 5% and Figure 5.42 shows that there is an improve in the maximum displacement equal to 12.9%. The optimization model is like the first model with the rigid bearings.

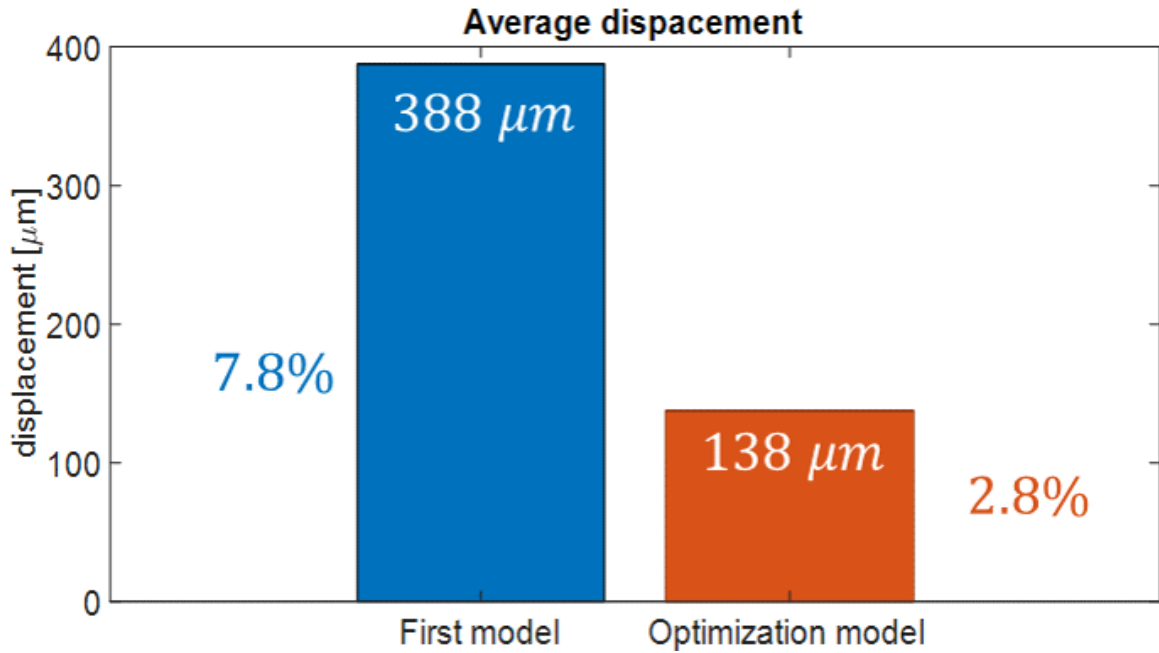


Figure 5.41: Average displacement comparison

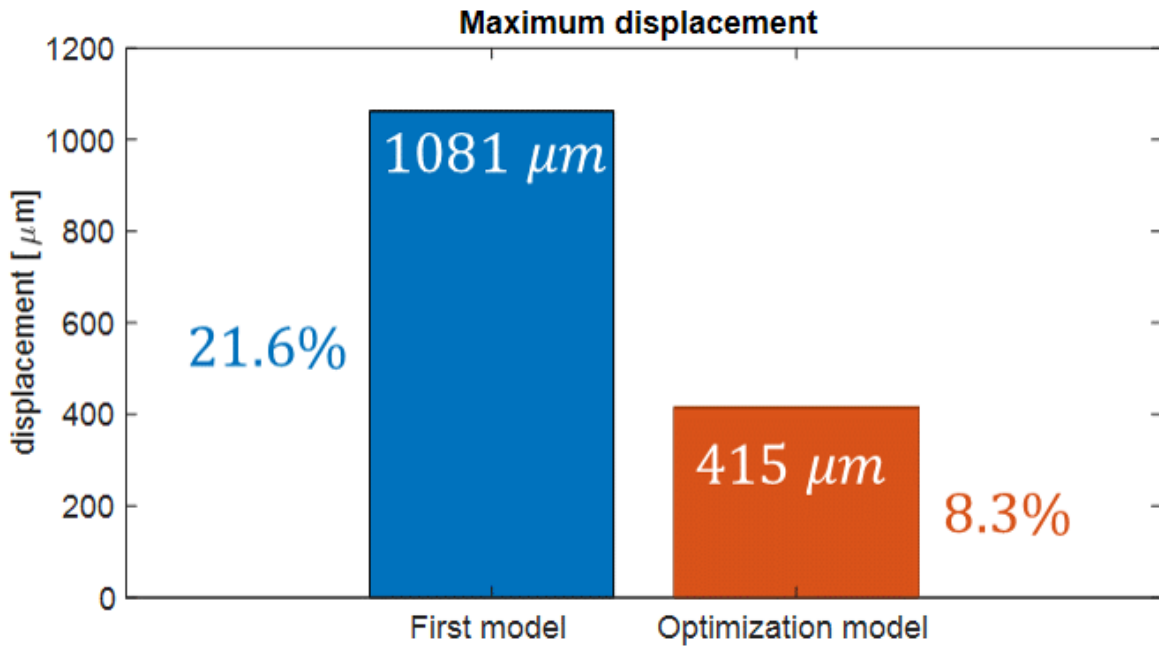


Figure 5.42 Maximum displacement comparison

6. Outlook and further studies

The purpose of this thesis had been to study the impact of gravity, magnetic pull and wind loads on the air gap size in FEM and in MBS for one generator configuration, hence a lot off possible further works could be done. The follow bullet list shows my proposals:

- Include the impact of the temperature during the FEM analysis in order to see how much the cooling system has to the strong.
- Only one bearing set has been analysed, taper roller (fixed bearing) with roller bearing (loosed bearing) so other interesting insights could be change the bearing set concept in order to find the optimization set that minimizes the air gap displacement
- In the first model, extend the length of the shaft and the connector up to the middle of the hub in order to move the impact of the weight blades and the wind loads between the two bearings. So, with a small increase of mass, there should be a decrease of air gap displacement due to the increase of the stiffness of the system. Figure 6.1 shows the sketch of how to change the bearings position.
- Only one optimization model has been performed with all the parameter change, the decrease of the displacement has been very big but is not easy to understand which parameter has more impact. The parameters that have been change are: the thickness of each components (from 100 mm to 120 mm), the rotor's arms position (from the beginning to the middle of the air gap length), the stator arm's orientation (in the first model the two set of stator's arms have the same orientations and in the optimization model they are out of phase) and the machine frame(in the optimization model there are one more component where there should be the bearing in touch to the tower). One simulation changing only one of the last parameters could be needed.
- To make sure that the optimization model has not impact on the resonance of the whole system the Campbell diagram for the wind turbine with the optimization model could be needed. There shouldn't be relevant difference between the two diagrams because the mass of the system doesn't change a lot off.
- Another model deep that could be that could be done is to make the freedom reduction of the generator component by component and make the same simulations that are already done, in order to see the differences.

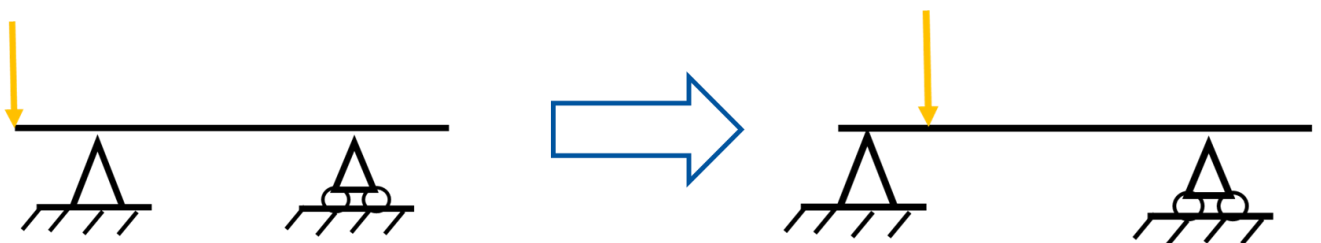


Figure 6.1: Different bearing position

7. Summary

The goal of this master thesis is to compare different model depths of a direct drive wind turbine to regard the generator air gap behaviour under the impact of the gravity, the magnetic pull and the wind loads in the FEM and MBS.

After the introduction, in the second chapter an overview of the wind turbine market and of the wind turbine technology has been shown. It has been observed that the last global meeting that has been done is the Paris agreement in 2015 and it enshrines the propose of parties to take the temperature increase under $2\text{ }^{\circ}\text{C}$ compared to the pre-industrial ages. In this political contest the wind turbine field having a business increase. At 2018 there were 870'000 employer (of which 160'200 in Germany and 260'00 in Italy) who worked in the wind turbine field for a capacity of 440'475 MW and a market value of 45'000 million dollars, and there are a lot off possibilities of market expansion. Right now, the maximum efficiency that a wind turbine has managed to reach is lower than 50% where the maximum physical limit is 59% (Belts limit), so there are still possibilities to increase it. The two configurations to build a multi MW wind turbine are the Gearbox (GB) and the Direct Drive (DD) the main difference between them are the absence of the gearbox in the second one. This difference makes the DD more reliability but more expansive because its generator must be bigger than the GB's generator. Due to its size (normally the diameter is around 5m) the DD generator is very heavy so very stiff materials needed in order to don't allow the air gap displacement (to have the maximum efficiency the air gap clearance should be 1/1000 times the air gap diameter) and however its deflections should be lower than 20% of original clearance. At the end of the chapter the main causes of the air gap displacement have shown, the author has focused on the loads that are in the topic of the work without, however, ruling out the other loads.

The third chapter shows the mathematical theories that are used to make the simulation with ABAQUS and SIMPACK. First, the FEM theory is explained, and the properties of each finite elements are described with an example from the literature to explain how to make the convergence analysis. After it, the MBS theory is shown with attention on the method to calculate the eigenmode because SIMPACK works with the natural frequency of the bodies. At the end the MAC matrix theory to compare the eigenmode behaviour in FEM and MBS has been explained

The wind turbine that has been analysed has a rated power of 3.6 MW it works with the nominal speed equal to 12 rpm, its rotor diameter is 130 m, the hub height is 115 m and between the ground and the rotor axis there is an angle equal to 5° . All part of the generator have been modelled with general steel. The mass of the generator is 160 ton and the mass of each blade is 27 ton. The air gap the length is 1300 mm, the diameter is 5000 mm, and its size is 5 mm.

The first model that has been done is the FEM generator model. The first stage required is the convergence analysis for the mesh of each component, a test load equal to 1 ton in each direction has been applied and the displacement and the natural frequencies have been estimated. The results of this first step have led to make the generator FEM model with 30'283 elements and 123'510 nodes, the only component made by tetragonal quadratic elements (C3D10) is the machine frame and all other components are made by hexagonal quadratic elements (C3D20R). The next stage has been made the generator MBS model. It has been made with only two bodies, one for the stator part (machine frame, pin, stator) and one for the rotor part (hub, connector, rotor). To make SIMPACK model the *.fbi files for both parts are needed and they are made with the modal reduction with the CRAIG BAMPTON method in ABAQUS. In both models the bearings stiffness is been applied and the auto MAC matrix and the MAC matrix have performed, first between each component and later between the two whole models. The results from the MAC matrices show that the behaviour of the eigenmode of the FEM and MBS models have a good matching with some coupling eigenmodes, this means that the eigenmodes with almost the same eigenfrequency have reversed behaviour in SIMPACK and in ABAQUS.

Right when the validation of the generator models has been done the impact of the gravity (gravity means the impact of the gravity plus the weight of the blades), the magnetic pull and the wind loads has been analysed. The air gap displacement has been modelled with an interaction between the external rotor surface and the internal stator surface, the data needed from ABAQUS is called COPEN and it measures the distance between two surfaces. The static analysis have led that the air gap displacement under the effect of the only gravity is in the range between $-440 \mu\text{m}$ to $370 \mu\text{m}$ (-8.8% to 7.4%) with an increase of size in the bottom of the air gap and a decrease in size in the top of the generator. Different model depths for the magnetic pull are compared, its properties have been split in 1 slice up to 20 slices, and the results show that the air gap displacement is always in a range from $-534 \mu\text{m}$ to $462 \mu\text{m}$ (-10.7% to 9.2%), so the configuration with only one slice has been chosen for the other simulations. The displacement distribution is the same as with only the gravity. The second model depth analyses how much the bearings surface on the pin and on the connector has to be: it has to take the bearing's whole surface, only half surfaces in the middle or only one slice in the middle. These simulations include also the wind loads and the displacement is always between $-1081 \mu\text{m}$ to $1062 \mu\text{m}$ (-21.6% to 21.4%). There is not significant change, so the first model has been chosen to make the modal reduction. In this last simulation the displacement distribution is reversed to the simulations without wind loads, this is because the impact of the bending moment is bigger than the impact of the gravity plus the magnetic pull. Comparing the three load cases to regard the maximum displacement the impact of the different loads is respectively: due to the gravity is 7.4% , due to the magnetic pull is 1.7% and due to the wind loads is 12.2% for the total percentual of 21.3% . Moreover, the impact of the bearings stiffness has been estimated and one simulation without the bearings properties (rigid bearings) has been done. The maximum air gap displacement is $382 \mu\text{m}$, 7.6% , it means that the biggest impact on the air gap size is due to the stiffness of the bearings, which, fortunately, is a changeable parameter.

To plot the air gap displacement from the FEM simulations a MATLAB scrip was made. It takes from the output ABAQUS files the position of every node of the rotor and with a sequence of loops it extrapolates coordinates of the nodes on the rotor's external surface and it attaches at each one the COPEN data minus 5, in so doing it makes a matrix with the air gap displacement for each node. This matrix has been plotted for each simulation with the imagesc MATLAB tool in order to have a plot with the length of air gap along the y axis and the angle between 0 to 360 along the x axis.

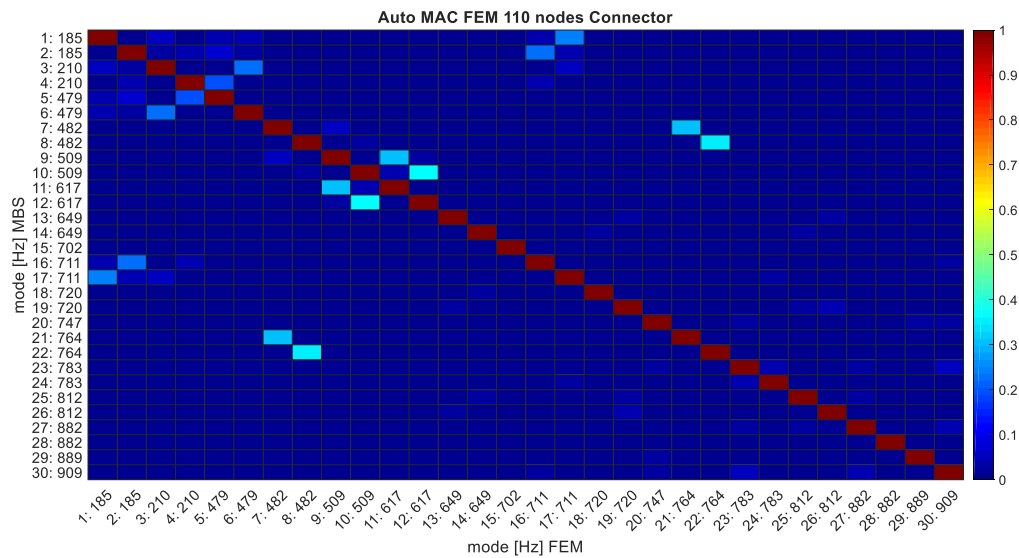
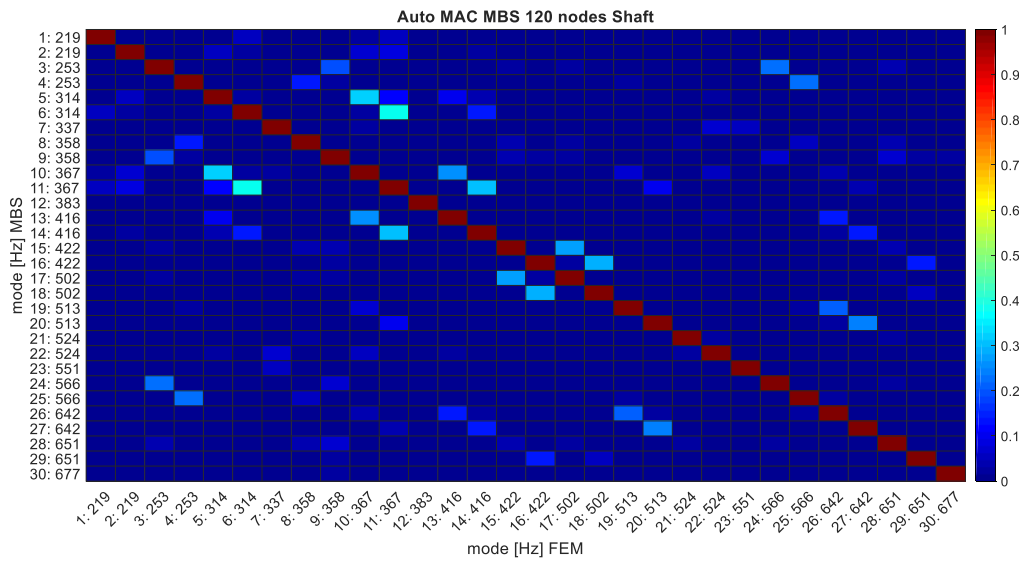
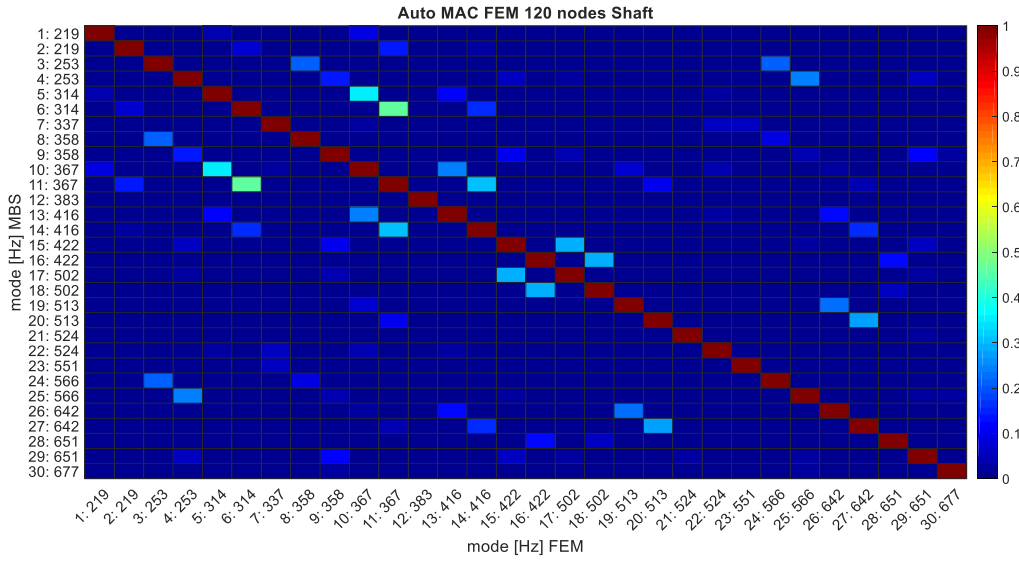
The MBS generator has been analysed for the same loads case of the FEM generator, but the air gap size has been studied only as the displacement between two markers in the middle of the air gap, one constrained with the internal stator surface and one constrained with the external rotor surface. The clearance at the begin and at the end has been measured as the half length of the air gap times the tangents of the angle between the x axis of the two markers plus (or minus) the delta z distance between them. In order to see how many eigenmode (without the IRM frequency) are needed different simulations with a different number of eigenmode active have been done. To have a good matching between the FEM and MBS output 80 eigenmodes are needed Before to implement the generator model in the wind turbine the required number of eigenmodes and the IRM cut frequency to calculated reliable deformations are identified. The number of eigenmodes needed is 10 and the IRM cut frequency is 400 Hz . After that the generator model has been implemented in the wind turbine system.

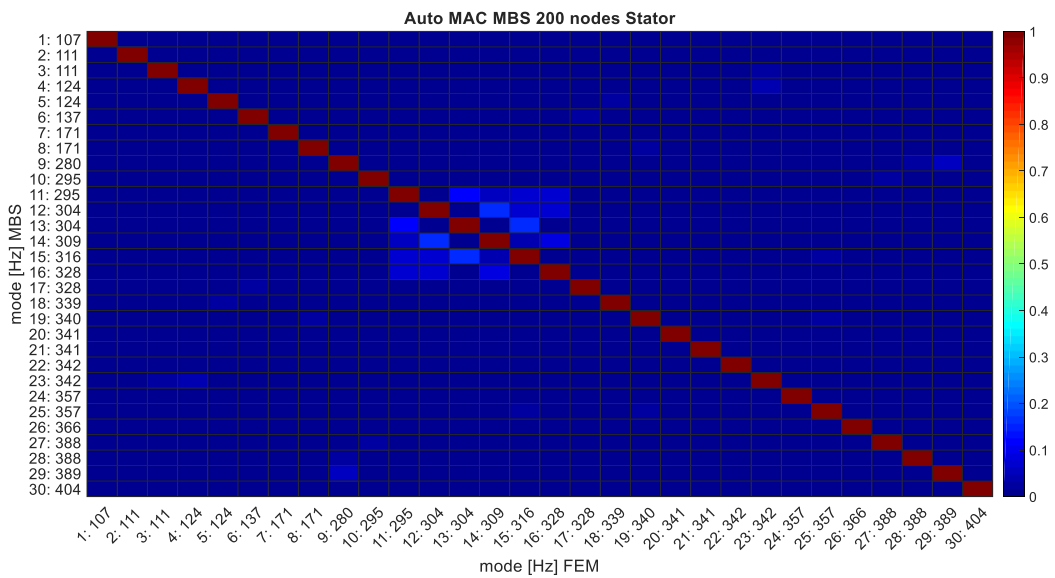
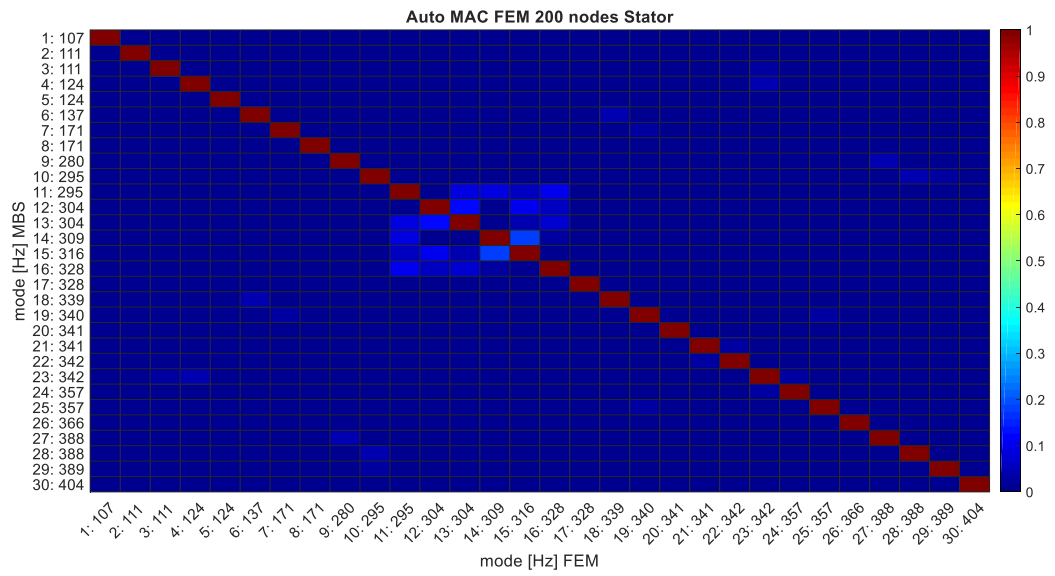
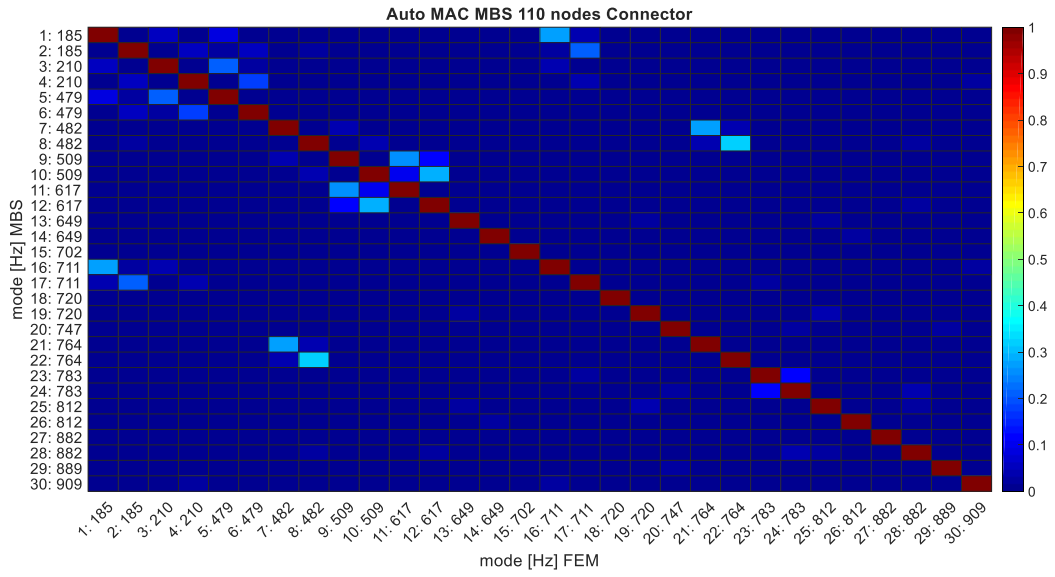
The Campbell diagram for the wind turbine has been charted and it shows that there are 6 resonance points in the working range but there is no resonance point at the nominal speed and there is also no resonance point for the $3p$ excitation, this means there are not dangerous criticalities which could cause critical failure of the system. The MBS simulations have been done with a wind speed of 12 rpm , a turbulence class A and for 600 s , as required by the norm. Only three different model depths for the magnetic pull have been analysed (1 up to 5 slices) and the results show that the difference between them is not relevant, hence one slice are enough to have good results. The air gap displacement is always in a range between 0 to 20% of the original

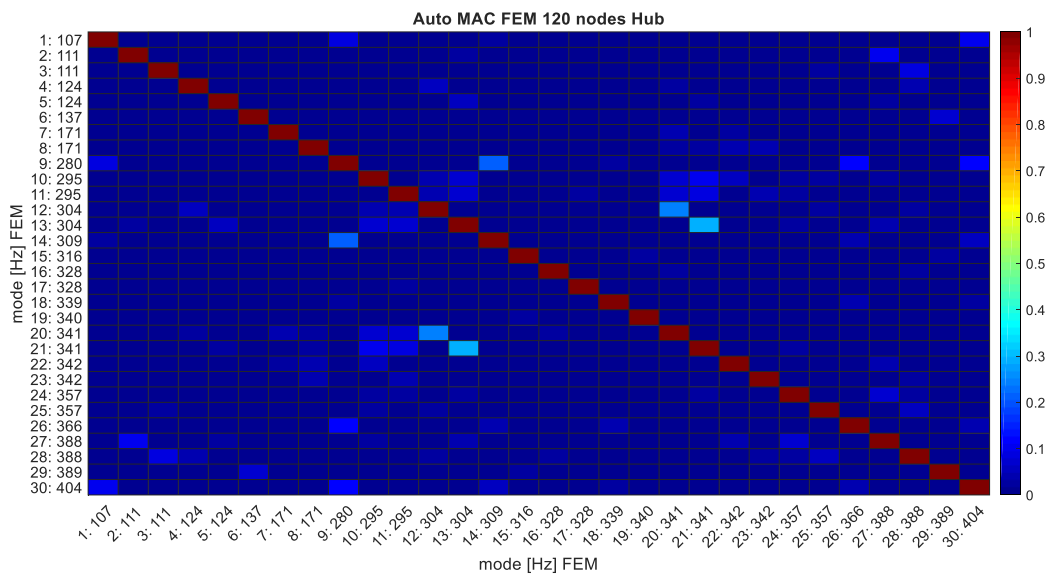
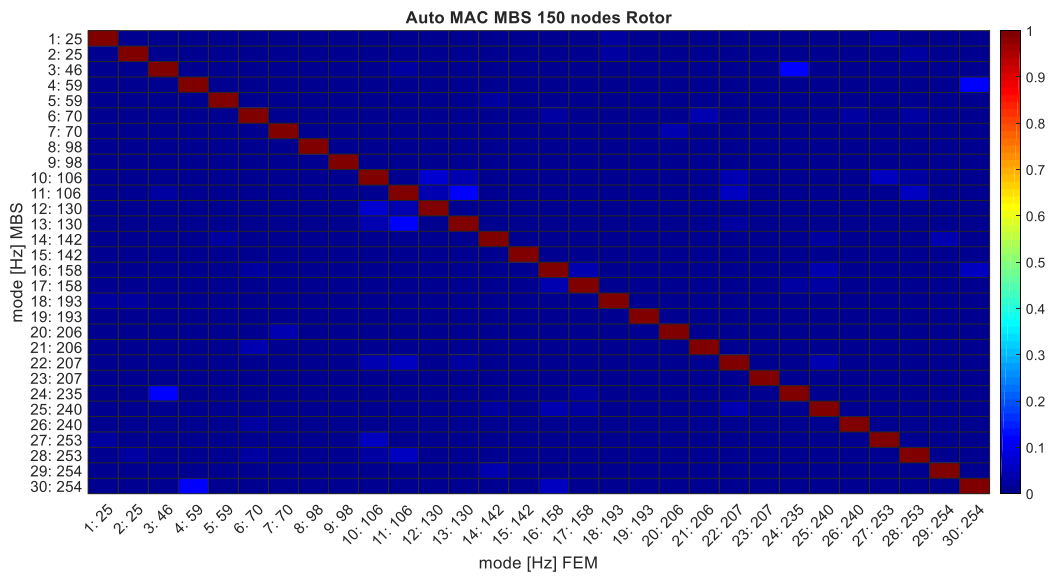
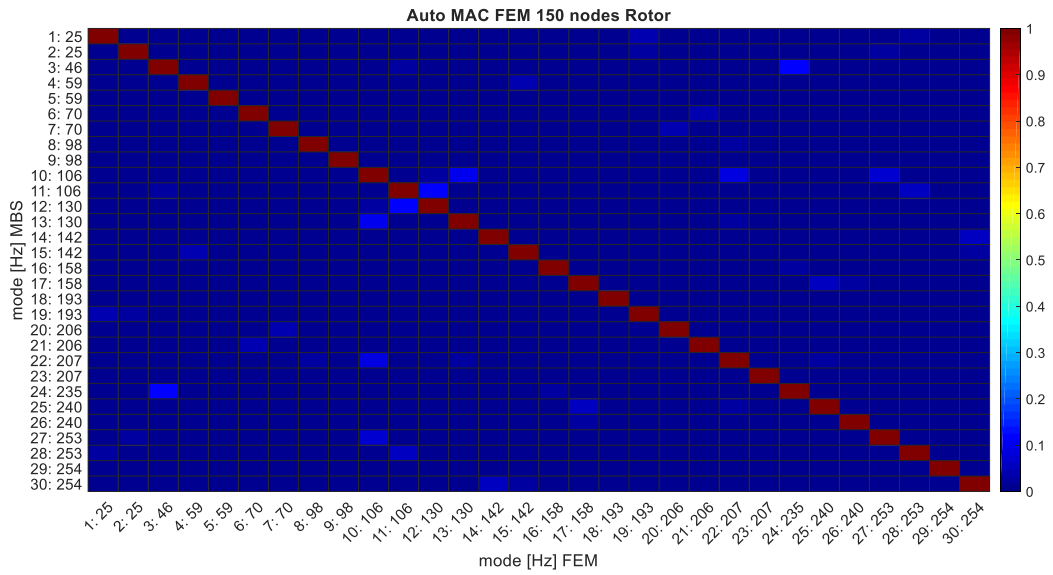
size and for most of the time between 6% to 14%. With the model deep of one slice the impact of the magnetic pull has estimated and, as in FEM, its impact is during the whole simulation around 1 – 2%.

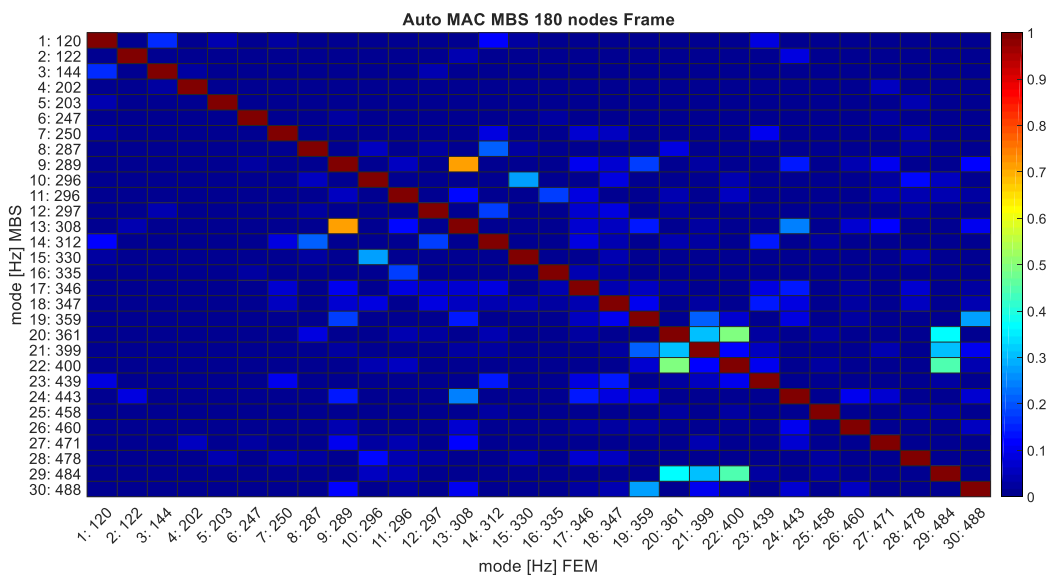
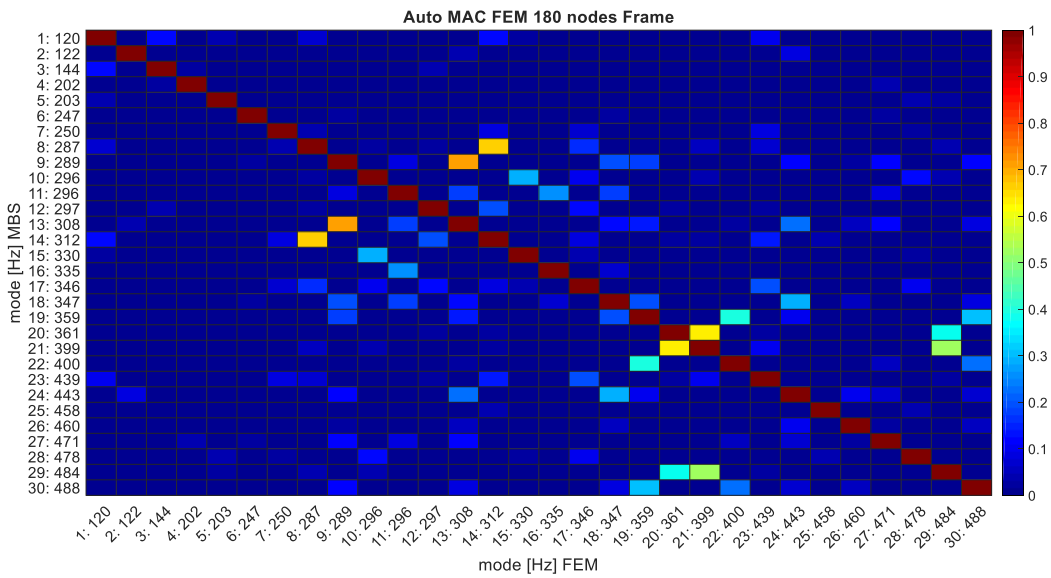
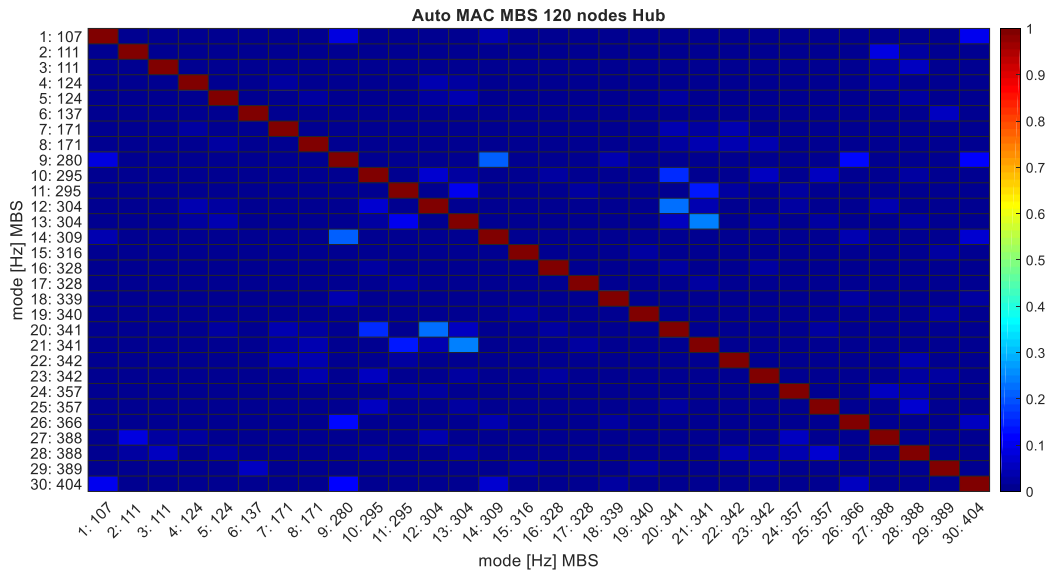
To conclude the thesis one optimization model has been made and the simulation with all loads has been performed. The changes made to improve the generator are: the thickness of each component is increased from 100 *mm* to 120 *mm*, the rotor's arms are moved in the middle of the air gap, the two sets of stator's arms have been shift and one more components in the machine frame has been added where there should be the bearing in touch with the tower. All these changes bring an increase of mass equal to 30 *ton*, the new total mass is 190 *ton*. The air gap displacement is still almost the same as in the first model but the now is 415*mm*, 666*mm* lower than in the first model. So, with an increase of 18,7% of the original mass there is and improve regarding the air gap behaviour equal to the 13.3%.

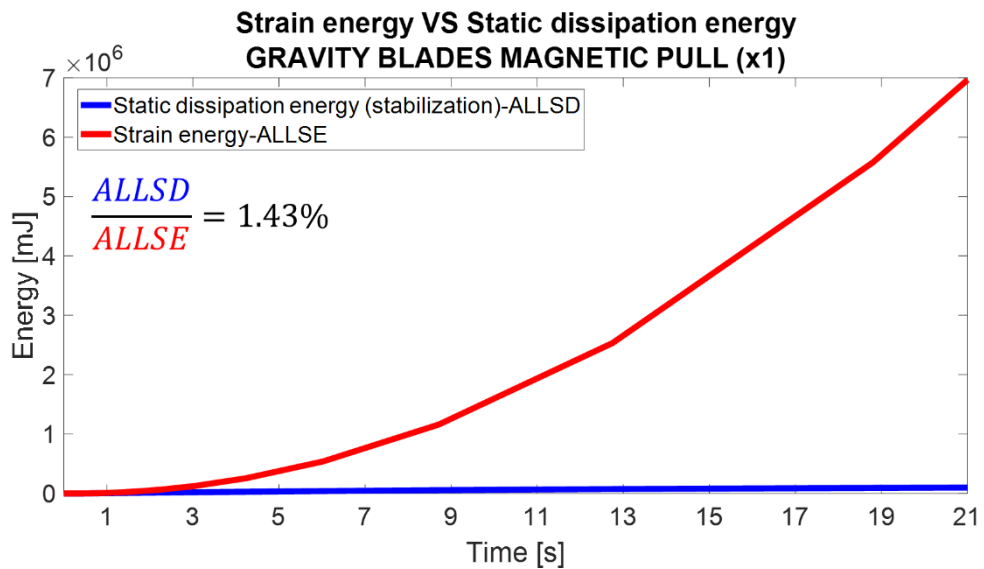
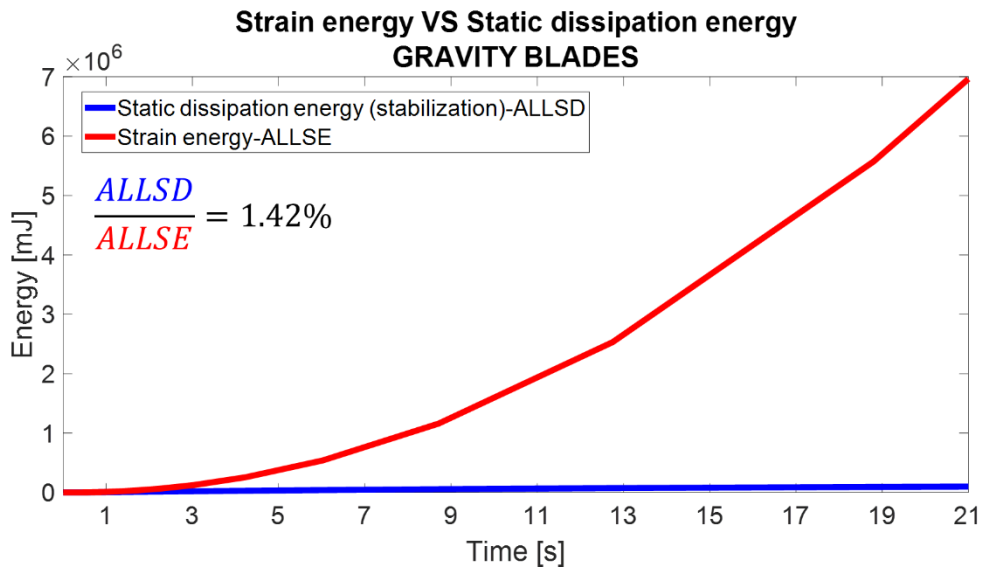
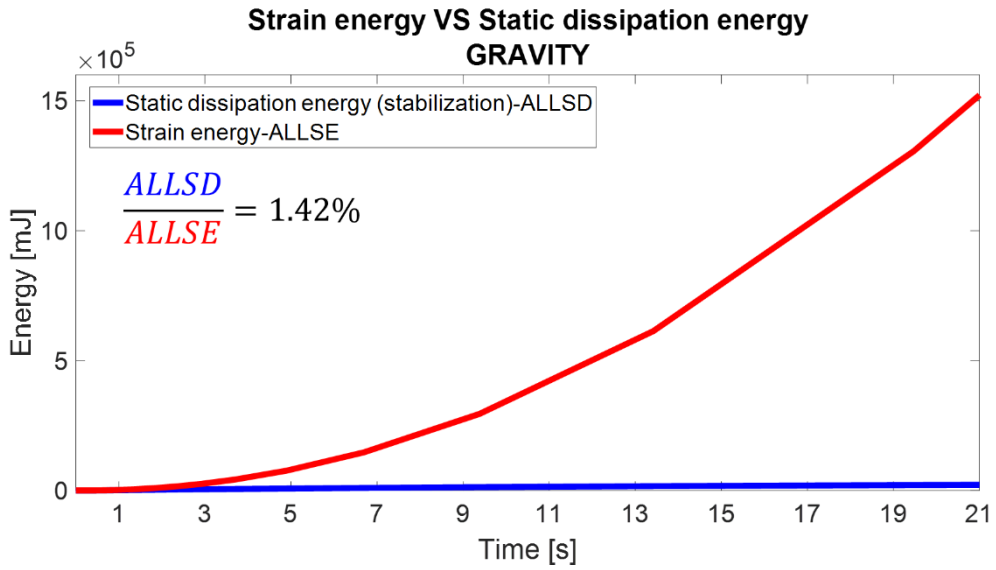
Appendix

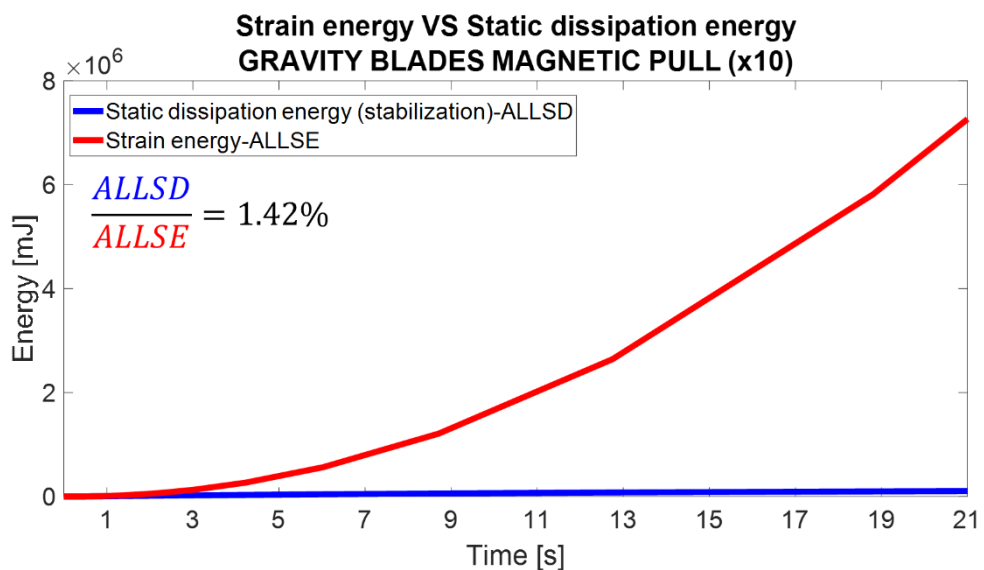
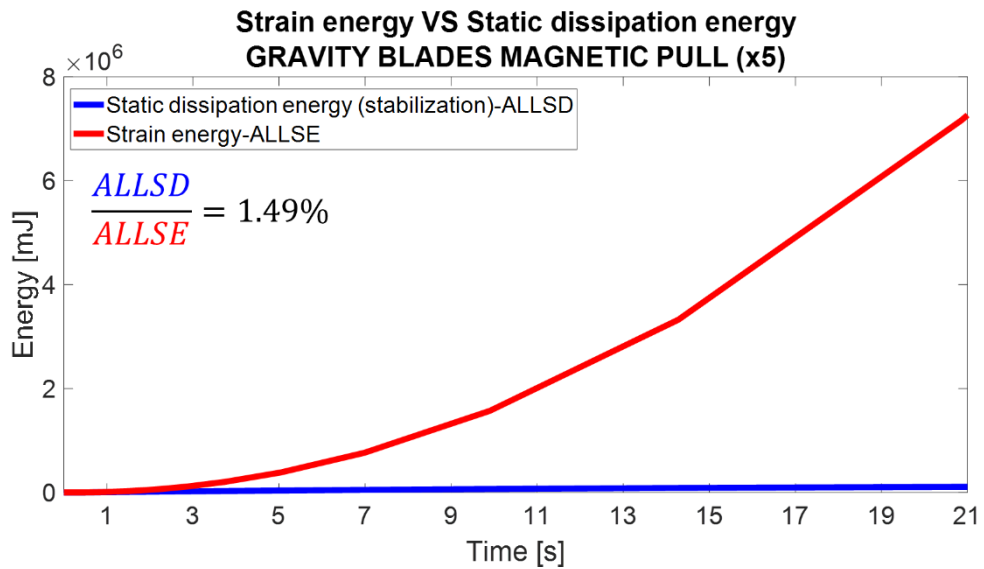
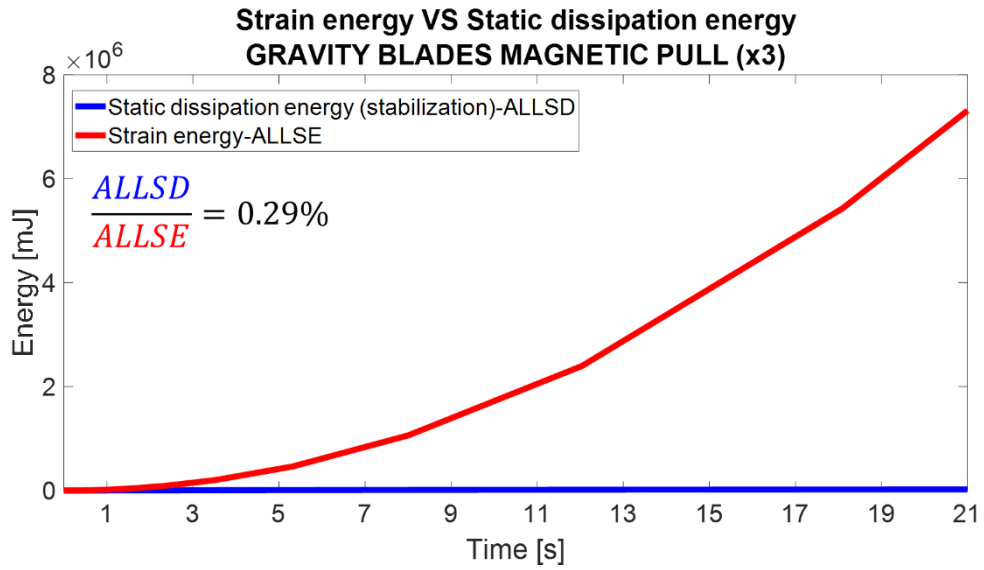


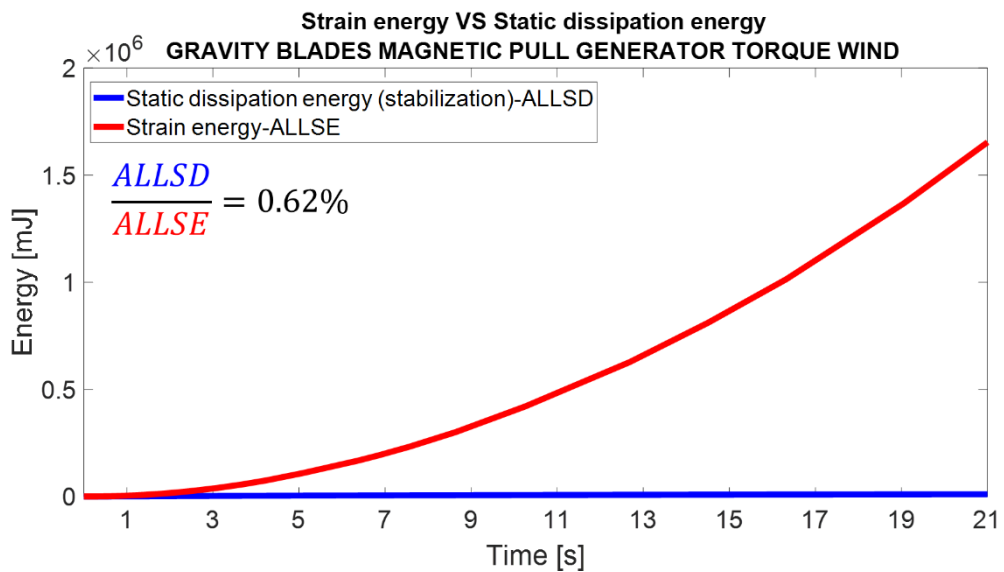
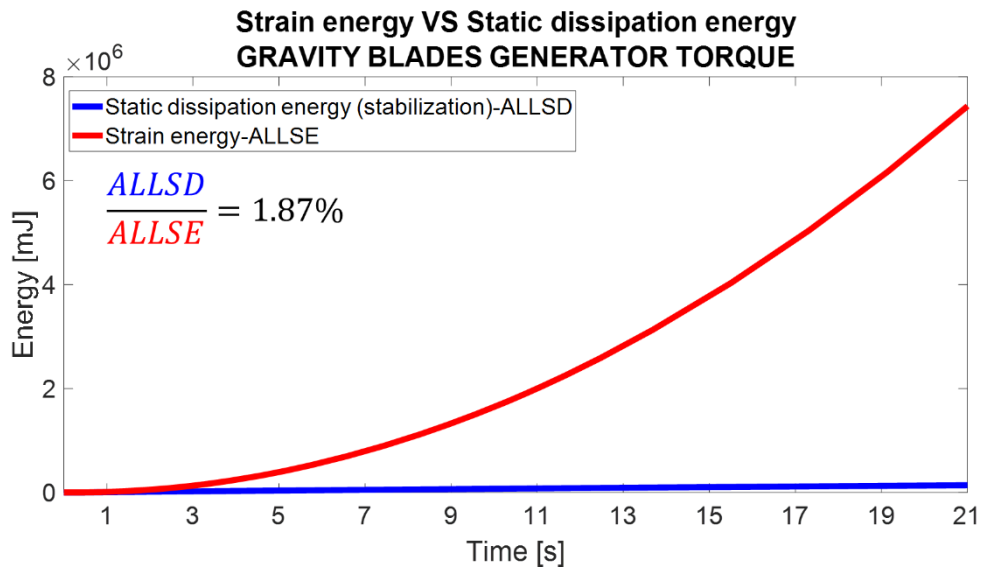
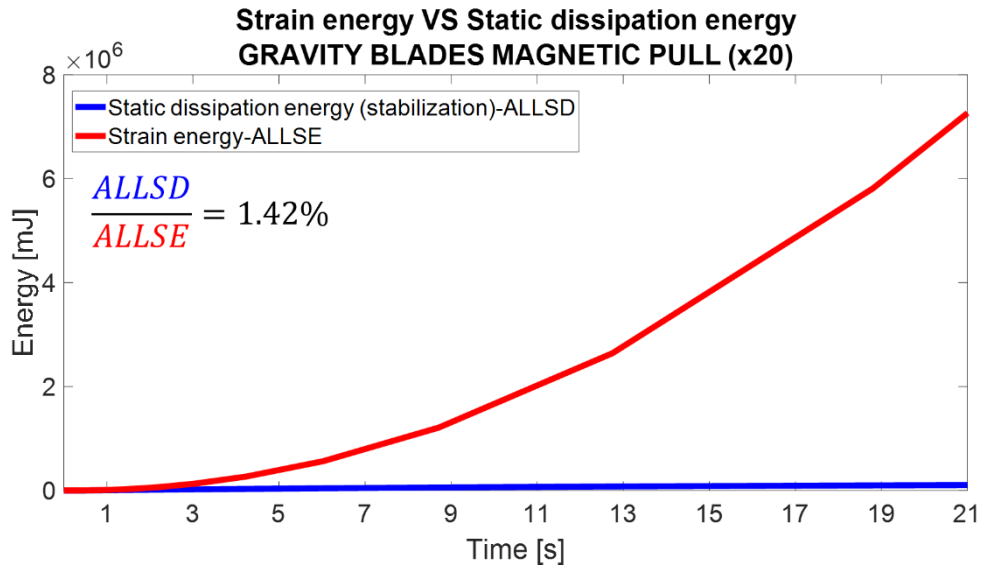


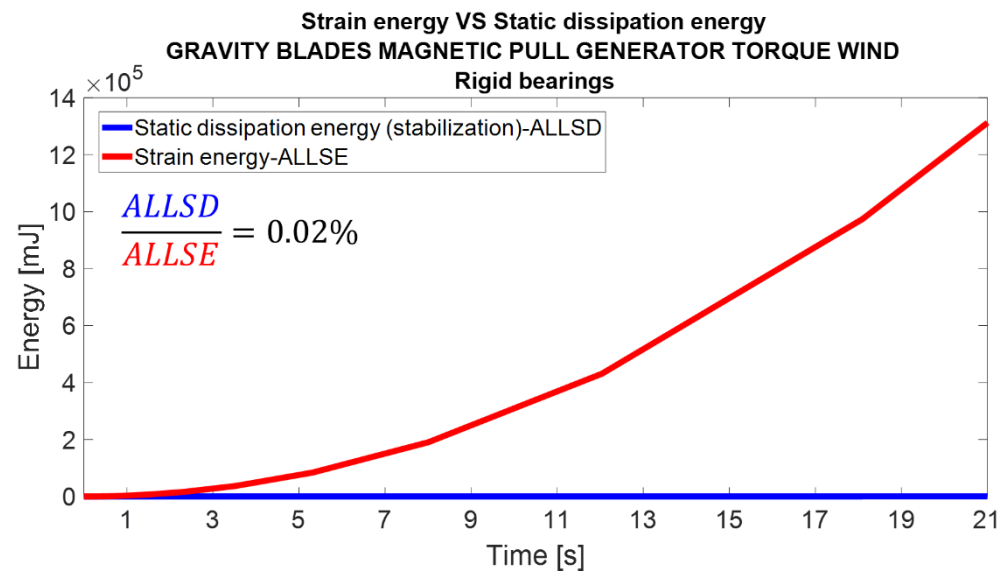
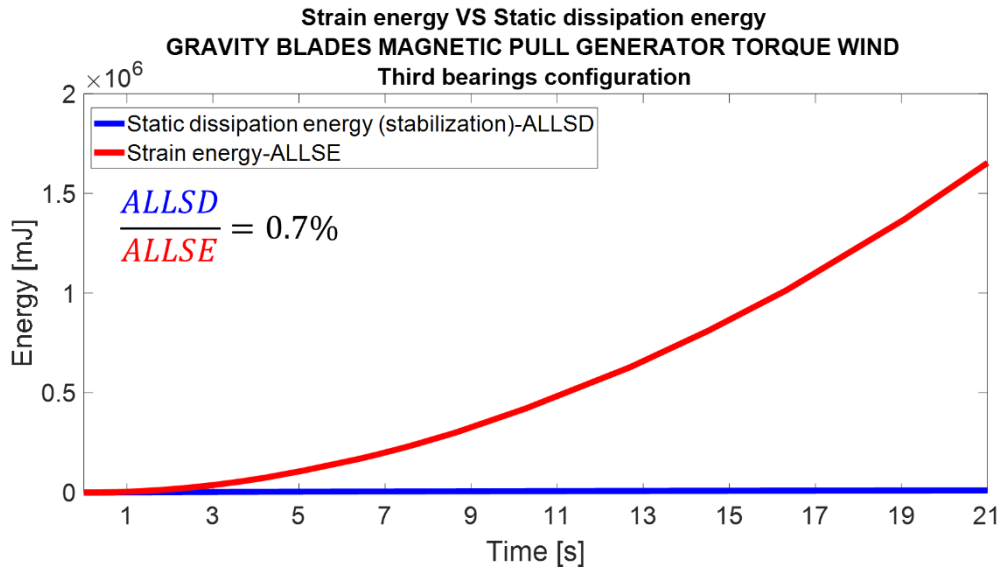
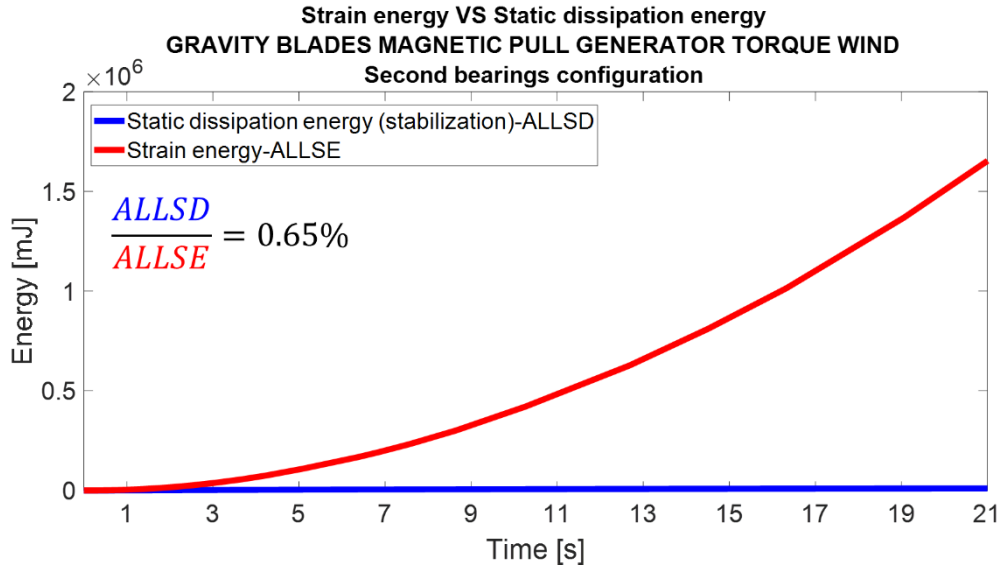


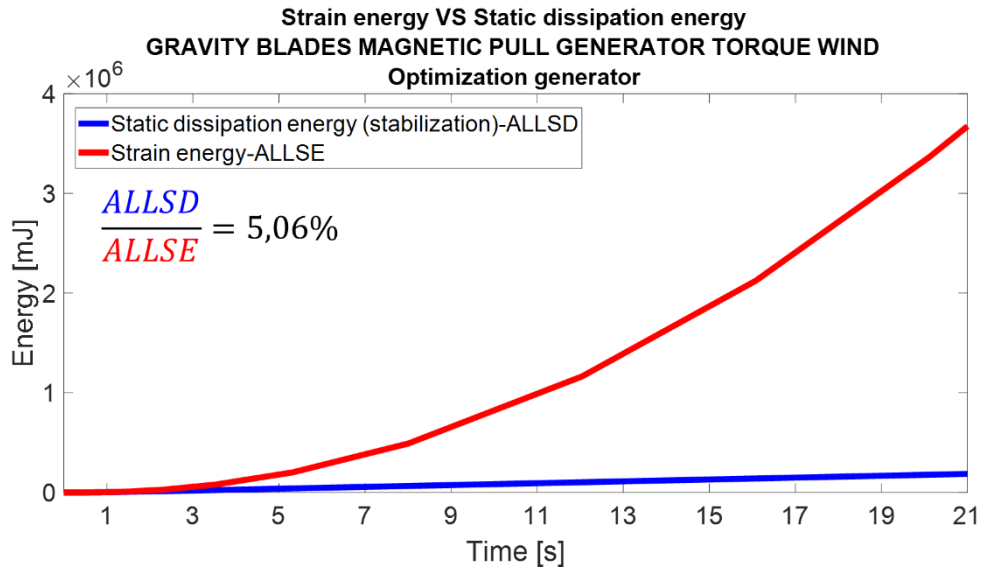












References

- [1] IEA International Energy Agency, "CO2 Emissions from Fuel Combustion 2018".
- [2] "IPCC, 2014: Summary for Policymakers. In: Climate Change 2014: Mitigation of Climate Change. Contribution of Working".
- [3] NOAA National Oceanic and Atmospheric Administration, "<https://www.ncdc.noaa.gov/sotc/global/201902>," [Online].
- [4] Canadian Institute of Actuaries, "Climate Change and Resource Sustainability," 2015.
- [5] United Nations, "Kyoto protocol to the united nations framework convention on climate change".
- [6] United Nations, "Paris agreement".
- [7] IEA Wind Technology Collaboration Programme, "Annual Report," 2017.
- [8] GWEC, "Global wind report 2018," april 2019.
- [9] General Electric, "<https://www.ge.com/renewableenergy/wind-energy/offshore-wind/haliade-x-offshore-turbine>," [Online].
- [10] BloombergNEF, "Clean Energy Investment Trends, 2Q 2018," July 9, 2018.
- [11] IRENA International Renewable Energy Agency , "Renewable Energy and Jobs," 2017.
- [12] A. Schaffarczyk, "Introduction to Wind Turbine Aerodynamics," Springer-Verlag, Berlin, 2014.
- [13] Wei Tong, Kollmorgen Corporation, Virginia, USA., "Fundamentals of wind energy, CHAPTER 1".
- [14] A. M. R. Magdi Ragheb, "Wind Turbines Theory - The Betz Equation and Optimal Rotor Tip Speed Ratio".
- [15] J. Dean, E. Hotchkiss, A. Kandt and R. Robichaud, "Broad Overview of Energy Efficiency and Renewable Energy Opportunities for department of Defense Installations," Jesse Dean, Alicen Kandt, Eliza Hotchkiss, Robi Robichaud.
- [16] A. Zavvos, "Structural Optimisation of Permanent Magnet Direct Drive Generators for 5MW Wind Turbines," The University of Edinburgh, 2013.
- [17] C. L. Archer and M. Z. Jacobson, "Evaluation of global wind power," Departement of Civil and Environmental Engineering, Standord University, Stanford, CA, 2005.
- [18] R. Whitlock, "Interesting engineering," [Online]. Available: <https://interestingengineering.com/factors-in-wind-turbine-gearbox-failure>.
- [19] A. M C DONALD, M. MUELLER and A. ZAVVOS, "Electrical, thermal and structural generator design and systems integration for direct drive renewable energy systems".
- [20] J. Tan, W. Hu, X. Wang and . Z. Chen, "Effect of Tower Shadow and Wind Shear in a Wind Farm on AC Tie-Line Power Oscillations of Interconnected Power Systems," 2013.
- [21] H. Sintra, V. Mendes and R. Melício, "Modeling and Simulation of Wind Shear and Tower Shadow and on Wind Turbines," 2013.
- [22] B. A. T. Iamamura, Y. Le Menach, A. Tounzi, N. Sadowski and E. Guillot, "Study of Static and Dynamic," 2010.

- [23] M. Polikarpova, P. Roytta, J. Nerg and J. Pyrhönen, “Direct-drive permanent magnet generators for high-power wind turbines: Benefits and limiting factors,” *IET Renewable Power Generation*, 2012.
- [24] A. McDonald, M. Mueller and H. Polinder, “Structural mass in direct-drive permanent magnet electrical generators,” 2008.
- [25] A. Salah, “A Review of the Monitoring and Damping Unbalanced Magnetic Pull in Induction Machines Due to Rotor Eccentricity,” 2019.
- [26] D. V. Hutton, *Fundamentals of finite element analysis*, Mc Graw Hill, 2004.
- [27] Abaqus 6.10, “Abaqus documentation,” [Online].
- [28] B. Corves, *Multibody Dynamics Lecture*, Institute of Mechanism Theory, Machine Dynamics and Robotics, RWTH Aachen University, 2017.
- [29] Simpack assistance 2018x, [Online].
- [30] R. J. Allemang, “The Modal Assurance Criterion –Twenty Years of Use and Abuse”.
- [31] M. Pastora, M. Binda and T. Harcarika, “Modal Assurance Criterion”.
- [32] Siemens Phenom , 10 06 2016. [Online]. Available: <https://community.plm.automation.siemens.com/t5/Testing-Knowledge-Base/Modal-Assurance-Criterion-MAC/ta-p/368008>.
- [33] SKF , [Online]. Available: <https://www.skf.com/de/products/bearings-units-housings/roller-bearings/tapered-roller-bearings/double-row-tapered-roller-bearings/double-row-tdi-design/index.html?designation=331590&unit=metricUnit>.
- [34] Simpack documentation , “<https://www.3ds.com/products-services/simulia/products/simpack/>,” Dassault. [Online].
- [35] Y. Yasa and E. Mese, “Thermal Assessment of Outer Rotor Direct Drive Gearless Small-Scale Wind Turbines,” *Academy of Science, Engineering and Technology International Journal of Environmental and Ecological Engineering*, vol. 9, no. 8, 2015.
- [36] Vestas, “Annual report,” 2017.
- [37] GE Renewable Energy, “Onshore wind,” 2017.
- [38] H. Polinder, G. Shrestha Shrestha and D.-j. Bang, “Review of generator systems for direct-drive wind turbines”.
- [39] U.S. department of energy , “Advange wind turbine drivetrain concepts: workshop report,” June 29-30, 2010.
- [40] J. A. Ferreira, H. Polinder and B. B. Jensen, “Trends in Wind Turbine Generator Systems,” *IEEE JOURNAL OF EMERGING AND SELECTED TOPICS IN POWER ELECTRONICS*,, 2013.
- [41] A. Salah, “A Review of the Monitoring and Damping Unbalanced,” University of Technology Sydney , 2019.
- [42] P. Bangert, “algorithmica technologies GmbH,” [Online]. Available: http://www.algorithmica-technologies.com/en/case_studies/failures-of-wind-power-plants.

[43] SKF, [Online]. Available: <https://www.skf.com/de/products/bearings-units-housings/roller-bearings/cylindrical-roller-bearings/single-row-cylindrical-roller-bearings/single-row/index.html?designation=NU%2029/1180%20ECMA/HA1&unit=metricUnit>.